ABSTRACT

Title of Document: COMBINATORIAL INVESTIGATION OF
                                      RARE-EARTH FREE PERMANENT
                                      MAGNETS

                                      Sean Wu Fackler, Doctor of Philosophy 2015

Directed By: Professor Ichiro Takeuchi, Department of
                                      Materials Science and Engineering

The combinatorial high throughput method allows one to rapidly study a large number of samples with systematically changing parameters. We apply this method to study Fe-Co-V alloys as alternatives to rare-earth permanent magnets. Rare-earth permanent magnets derive their unmatched magnetic properties from the hybridization of Fe and Co with the f-orbitals of rare-earth elements, which have strong spin-orbit coupling. It is predicted that Fe and Co may also have strong hybridization with 4d and 5d refractory transition metals with strong spin-orbit coupling. Refractory transition metals like V also have the desirable property of high temperature stability, which is important for permanent magnet applications in traction motors.

In this work, we focus on the role of crystal structure, composition, and secondary phases in the origin of competitive permanent magnetic properties of a particular Fe-Co-V alloy. $Fe_{38}Co_{52}V_{10}$, compositions are known as Vicalloys. Fe-Co-

V composition spreads were sputtered onto three-inch silicon wafers and patterned into discrete sample pads forming a combinatorial library. We employed high-throughput screening methods using synchrotron X-rays, wavelength dispersive spectroscopy, and magneto-optical Kerr effect (MOKE) to rapidly screen crystal structure, composition, and magnetic properties, respectively. We found that in-plane magnetic coercive fields of our Vicalloy thin films agree with known bulk values (300 G), but found a remarkable eight times increase of the out-of-plane coercive fields (~2,500 G). To explain this, we measured the switching fields between in-plane and out-of-plane thin film directions which revealed that the Kondorsky model of 180° domain wall reversal was responsible for Vicalloy's enhanced out-of-plane coercive field and possibly its permanent magnetic properties. The Kondorsky model suggests that domain-wall pinning is the origin of Vicalloy's permanent magnetic properties, in contrast to strain, shape, or crystalline anisotropy mechanisms suggested in the literature. We also studied the thickness dependence of an $Fe_{70}Co_{30}$-V thin film library to consider the unique effects of our thin film libraries which are not found in bulk samples. We present results of data mining of synchrotron X-ray diffraction data using non-negative matrix factorization (NMF). NMF can automatically identify pure crystal phases that make up an unknown phase mixture. We found a strong correlation between magnetic properties and crystal phase quantity using this valuable visualization.

In addition to the combinatorial study, this dissertation includes a study of strain controlled properties of magnetic thin films for future applications in random access memories. We investigated the local coupling between dense magnetic stripe

domains in transcritical Permalloy (tPy) thin films and ferroelectric domains of BaTiO$_3$ single crystals in a tPy/BaTiO$_3$ heterostructure. Two distinct changes in the magnetic stripe domains of tPy were observed from the magnetic force microscopy images after cooling the heterostructure from above the ferroelectric Curie temperature of BaTiO$_3$ (120°C) to room temperature. First, an abrupt break in the magnetic stripe domain direction was found at the ferroelectric a-c-domain boundaries due to an induced change in in-plane magnetic anisotropy. Second, the magnetic stripe domain period increased when coupled to a ferroelectric a-domain due to a change in out-of-plane magnetic anisotropy. Micromagnetic simulations reveal that local magnetic anisotropy energy from inverse magnetostriction is conserved between in-plane and out-of-plane components.

COMBINATORIAL INVESTIGATION OF RARE-EARTH FREE PERMANENT
MAGNETS

By

Sean Wu Fackler

Dissertation submitted to the Faculty of the Graduate School of the
University of Maryland, College Park, in partial fulfillment
of the requirements for the degree of
Doctor of Philosophy
2015

Advisory Committee:
Professor Ichiro Takeuchi, Chair
Assistant Professor John Cumings
Professor Lourdes G. Salamanca-Riba
Professor Robert M. Briber
Professor Johnpierre Paglione

Dedication

To my fiancé Kathryn, my parents Gregg and Eleanor, my brother Aaron,
and my most cherished grandparent Galia.

Acknowledgements

Here, I give thanks to my adviser, Prof. Ichiro Takeuchi, who never failed to provide me with a safe work environment to explore the wonders and labor of materials science. I am deeply honored to have worked and learned under your guidance these past five years. Thank you for your prompt responses, endless scientific and professional opportunities, consistent character, and attention to detail in preparing manuscripts and presentations. These are things I strive towards as I grow to be a scientist and continue to be an active member of society. In the future I hope to take better advantage of the opportunities you have to offer.

This acknowledgement also goes to my undergraduate adviser Prof. Sang-Wook Cheong, who will always be my first scientific mentor. You saw in me the potential to make it as a PhD and always made sure that I knew it wouldn't be easy.

I also want to thank my advising committee members Prof. Robert Briber, Prof. John Cumings, Prof. Lourdes Salamanca-Riba, and Prof. Johnpierre Pagione. You have all been generous with your time and efforts whether it was helping to vet a concept, offer research opportunities in polymers, something outside my specialty of functional materials, teaching me defects, or being the soundboard for my ideas. I will always be indebted to you for your help in this final stage of my Ph.D. Thanks also to Prof. Wuttig for being a guiding figure for my time at Maryland.

Thank you to all my lab mates who made my time at Maryland a pure joy to make mistakes, learn, and keep trying. The process of learning is such a messy business and it was a real pleasure to have Dwight Hunter, Yi Wang, Iain Kerzewski, Tieren Gao, Arun Luykx, Luz Sanchez, Christian Long, Peng Zhao, Anbu

Table of Contents

List of Tables

List of Figures

xii

Chapter 1. Introduction

1.1 Magnetic Thin Film Research in Energy and Information Technology

We discuss two main topics in this dissertation related to developing novel functional magnetic materials. My first topic focuses on using the combinatorial thin film approach in a search for permanent magnets without rare-earth elements. Rare-earth permanent magnets are currently the strongest permanent magnets available, and "green" energy technologies like wind turbines and electric vehicles rely on them for efficient operation of their generators and motors. 90% of world production of rare-earth elements like Nd, Dy, and Sm occur in China, and their prices have been unstable since the "rare-earth crisis" in 2011 [1]. Rare-earth prices increased over ten-fold in 2011 when China unexpectedly restricted exports, and prices have still only dropped to 2-3 times the pre-crisis values. Development of effective and inexpensive alternatives to the current dominance of rare-earth containing permanent magnets will help keep the growing demand for "green" energy affordable. Promising candidates for alternatives include Fe-Co-X alloys where X is a refractory metal including V, W, Mo, Nb, Zr, Hf, and Ta. Fe-Co on its own has one of the largest known magnetizations (2.35 Telsa) and theory suggests that mixtures with refractory metals may increase magnetocrystalline anisotropy thereby increasing the coercive field necessary for a good permanent magnet [2]–[4].

In this dissertation we apply the combinatorial thin film approach to study the Fe-Co-V ternary system where the compositions near $Fe_{40}Co_{52}V_8$ are well-known alloys called Vicalloys. A Vicalloy is a competitive permanent magnetic material still

1

used in low-torque hysteresis motors [5], [6], but the origin of its magnetic hardness is not well understood [5], [7]. Understanding the mechanism for known permanent magnets without rare-earth elements will guide the engineering of future alternatives to rare-earth elements.

The combinatorial method allows the systematic study of materials structure and properties versus composition with the goal to reveal the underlying origin of the desired properties. The combinatorial method has previously been used to successfully find new magnetic materials in ferromagnetic shape memory alloy systems and magnetostrictive ternary systems [8]–[10]. It has also been effectively used to investigate composition-structure-property relationships across composition spread wafers. The combinatorial method then offers the ability to (1) uncover unexplored composition regions in the Fe-Co-V system, and (2) have the same fabrication environment for hundreds of unique composition samples compared to the individual preparation used previously in the literature [7]. Individual sample preparation can lead to irreproducible results because of small variations between samples compared to the parallel fabrication of hundreds of different compositions possible in the combinatorial method.

The second part of this dissertation focuses on magnetic materials in information technology (IT) where there is a need for more energy efficient memory and logic devices for next generation communication devices and computers. Memory and logic devices have metal-oxide-semiconductor field-effect-transistors (MOSFET) that use electric charge to perform switching of bits. A MOSFET's energy dissipation is then decided by the injection or extraction of charge, which

produces unwanted Joule heating. The density of transistors in an integrated circuit has doubled every two years since the 1970's and the observation is now called Moore's law. The major obstacle in continuing Moore's law is excessive heat dissipation leading to malfunction or catastrophic burn-out [11].

Composite multiferroics, where a magnetic (magnetostrictive) thin film is in intimate contact with a ferroelectric material, offer an energy efficient solution for digital memory and logic. Multiferroic means having the ability to control magnetism with an electric field (or vice-versa) and uses dramatically less energy to switch magnetic bits than the motion of electric charge in a transistor [12]. Magnetic bits for random access memory (RAM) has been proposed for other memories like spin-torque transfer and magnetic-RAM, however similar energy dissipation problems remain because of their reliance on flowing charge to provide magnetic fields. Hence, composite multiferroics offer a new paradigm in low-power digital memory.

To date, many groups have studied macroscopic properties of composite multiferroics but microscopic local interactions of ferroelectric and ferromagnetic domains are lacking in the literature. The strong desire for device miniaturization requires in depth understanding of the local nature of these composite multiferroic materials. Therefore quantitative studies of the microscopic interactions are needed to advance the field for future applications in high-density, high efficiency multiferroic memories. In the second part of this dissertation we present experimental results and simulations of a transcritical Permalloy film with magnetic stripe domains sputtered on top of a $BaTiO_3$ single crystal in order to study the local control of strain induced of magnetic anisotropy. This work combined with our group's previous results on the

control of all-thin-film ferroelectric domains brings us one step closer to making compact and efficient multiferroic memory devices. The results of this second topic are published in *Applied Physics Letters* under the title "Local control of magnetic anisotropy in transcritical Permalloy thin films using ferroelectric $BaTiO_3$ domains."

These two topics on novel functional magnetic materials are connected by the similarities in which magnetic materials are studied; requiring knowledge of thin film deposition, magnetometry (measurements of magnetic hysteresis loops), microstructure, crystallography, and micromagnetic modeling. Unique to the first topic of the dissertation is the combinatorial thin film high-throughput method introduced in the next sections. Throughout the following introductory chapter a combination of borrowed literature results and figures are mixed explanatory figures that may contain representative data. Please note that if there is no reference in the title caption, then the work is the original work of this dissertation's author.

1.2 Introduction to the Combinatorial High-Throughput Method

Materials science has the goal of discovering and designing new materials using the paradigm of relating synthesis, structure, properties and performance of said materials. The traditional approach to finding these relations is the trial and error method where individual materials are synthesized and tested for their performance in a given application, similar to the discovery of the light bulb filament. A more systematic experiment, for example, the study of properties across a binary system of two metals previously required the laborious process of separately synthesizing a large number of samples across the binary. Not only is this traditional method slow and results in large missing areas of the composition space, but also introduces

undesired variation in sample preparation conditions. The combinatorial method was created to address these inherent materials science issues.

Combinatorial science allows the more rapid and systematic search and discovery of new materials through the synthesis and analysis of large numbers of possible candidates. This general approach was used in 1960's in the search for new superconducting and electronic materials [13], [14], although it was not described as combinatorial science. It wasn't until the 1990's that combinatorial chemistry was developed in the pharmaceutical industry to accelerate the discovery of new drugs [15].

Increasing economic pressure for innovation combined with increasing scarcity and prices of resources have prompted the desire to accelerate the process of discovery of new materials and their introduction into commercial products. This process traditionally takes more than twenty years, for example the development of lithium ion batteries [16]–[18] or semiconductor technologies. In 2011, President Obama launched the Materials Genome Initiative (MGI) as part of a multi-agency effort to revitalize the American manufacturing sector with the ambitious goal of doubling the pace of advanced materials discovery, development, and commercialization [19]. The search for alternatives to rare-earth permanent magnets using the combinatorial method is then part of this effort to accelerate the discovery of new materials.

In the pursuit of any new material discovery there are a staggering number of composition choices. Take the number of elements on the periodic table that are stable and usable as 86. Man-kind has largely studied the unary and binary systems

while a fraction of ternary systems have been studied and an even smaller fraction of more complex systems. By simply calculating the possible combinations of 3 elements from the 86 elements, not considering order, there are over 100,000 ternary combinations. For quaternary combinations, there are over 2 million. The total number of combinations between 86 such elements can be presented as in Figure 1-1, showing the known and unknown elemental combinations man has studied. The figure helps us understand the need for experimental methods that rapidly accelerate man's ability to explore this vast space of material possibilities. Certainly the traditional one-by-one method does not provide the speed or systematic exploration necessary for such an expedition.
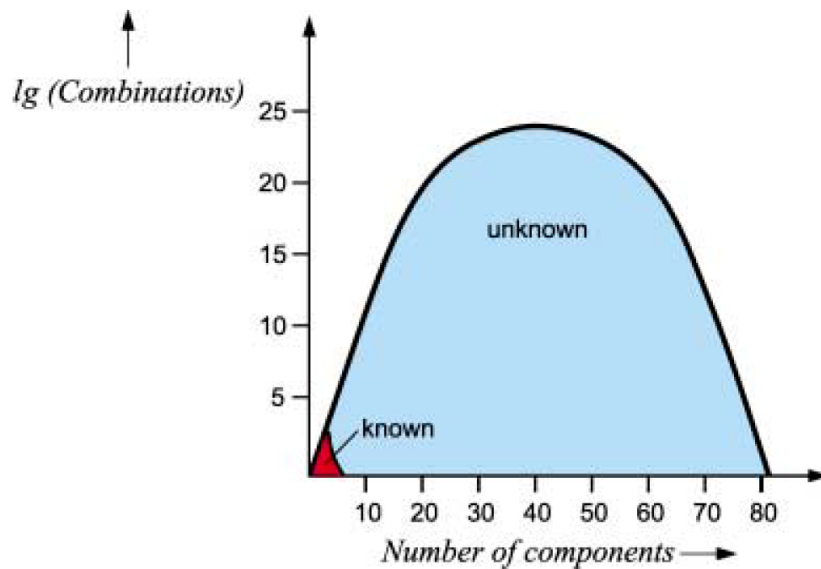
Figure 1-1 Plot giving perspective on the scale of unexplored materials systems by showing the possible combinations of reactive elements and the number of combinations mankind has investigated [20].

Advanced combinatorial methods alone are not sufficient to explore all known combinations with the addition of possible parameters for preparation including temperature, gas partial pressure, thermal history, and sample size. Strategic planning using experience, intuition, or theoretical methods must be used to limit this parameter space to within realistic experimental capabilities. Theoretical methods such as CALPHAD (Calculation of phase diagrams) [21] or first principles calculations [22], [23] can inform combinatorial experiments about the most promising areas for research. Efficient experimental exploration of regions of interest with methods like on-the-fly machine learning [24] can further facilitate experimental measurements.

Figure 1-2 shows an example of a schema to integrate combinatorial synthesis into the discovery, development, and commercialization of a new material. A major attribute of this system is the iterative process of theory, experimental design, fabrication, and properties screening in the effort to identify lead materials for scale up and contribute to the knowledge base of known materials.

Companies such as Intermolecular (www.intermolecular.com founded in 2004) are profiting from the combinatorial method and its ability to accelerate research and development speed by orders of magnitude. This is particularly useful in the semiconductor industry where devices are largely made by thin film deposition techniques. Intermolecular uses a proprietary "High Productivity Combinatorial" platform to aid large semiconductor companies in the development of new intellectual property related to digital memory, processing and device structure [25]. The success

of Intermolecular highlights the combinatorial method's success with inorganic materials development in the semiconductors sector.
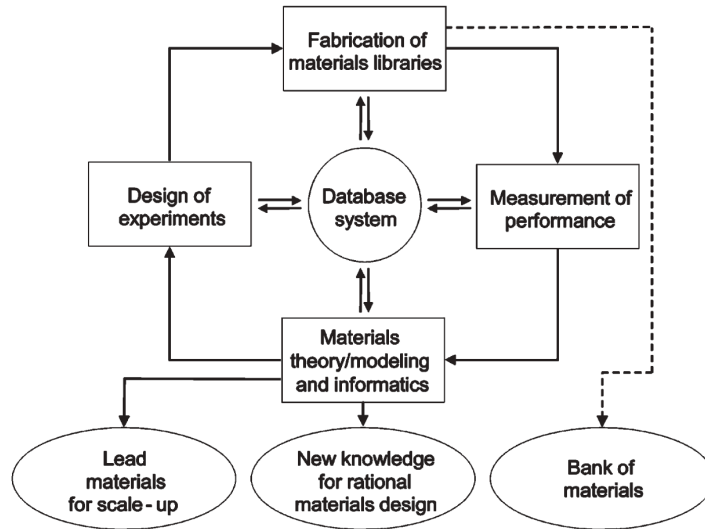
Figure 1-2 Schematic showing basic steps of combinatorial synthesis method leading from materials the iterative process of consulting theory, designing experiments, fabrication, and analysis, to scaling up adding to the database of known materials [26].

The combinatorial method lends itself to a number of bulk and thin film methods. Bulk methods, like the diffusion multiple approach use three or more metal blocks that are in intimate contact and then undergo high thermal treatments to allow thermal diffusion. This method is used for the rapid creation of bulk phase diagrams [27]. Thin film methods employ a variety of deposition techniques to achieve large composition gradients across a substrate where a high density of points can be mapped in composition space. The bulk fabrication of a number of samples with small variations in composition between them is a particularly challenging endeavor, but is achieved consistently and quickly using combinatorial thin film methods. This

is certainly an advantage if one is trying to understand a system where subtle composition variation yields interesting properties and structures [8].

The combinatorial thin film method becomes particularly useful when the desired application will ultimately be used as a thin film. The advantages are in the scale-up ability of certain deposition techniques allowing fewer steps from research and development to mass-production. This thin film method is applicable in solid-state batteries [28], superconductor devices [13], [14], [29], micro-electromechanical systems (MEMS) [30], coatings [26], and a host of other applications.

1.3 Combinatorial thin film synthesis methods

In this section we introduce four common techniques used in the synthesis of combinatorial thin film composition spreads, namely electron beam (e-beam) and thermal evaporation, magnetron sputtering, and pulsed laser deposition (PLD). A host of other techniques including molecular beam epitaxy (MBE), chemical vapor deposition (CVD), and atomic layer deposition (ALD) each offer advantages and disadvantages depending on the application. Physical vapor deposition techniques (like PLD, e-beam, MBE, and sputtering) offer the ability to create composition gradients either through shadow masks, moving shutters, or natural means where the gradient itself is from the natural geometry of the deposition source relative to the substrate surface. Chemical vapor deposition techniques such as CVD and ALD do not have the ability to use simple masks for composition gradients because of the nature of the deposition through chemical reaction with the surface of the substrate. Advantages of CVD and ALD are their ability to deposit uniform films over large surface areas.

1.3.1 Electron Beam and Thermal Evaporation

Evaporative deposition techniques heat the atoms to be deposited (called the source) into their gaseous state, which then travel to the substrate and condense back into a solid. Different heating sources have been developed including thermal evaporation, which uses resistive heating of sources, and electron beam (e-beam) evaporation, which uses a high-energy electron beam for heating the source. Thermal evaporation suffers from the limitation of its relatively low input power levels, while e-beam is the preferred method capable of depositing high melting point materials. Evaporative deposition techniques only deposit within line-of-sight of the source, making them amenable to layer-by-layer deposition using movable masks. Co-deposition is also possible with evaporative techniques. A number of combinatorial investigations have used e-beam evaporation, such as the study of dipolar fields in soft/hard magnetic layers [31], hydrogenation in the Mg-Al system [32] and hydrogenation in the Mg-Ni system with a new high-throughput infrared imaging technique [33], among others [34].

1.3.2 Pulsed Laser Deposition (PLD)

PLD uses a laser beam focused on the target material to ablate the material for deposition onto the sample surface. PLD ablation is distinct from evaporation because the laser beam pulse on the target surface is more akin to an explosion of vaporized material. This non-equilibrium process retains the stoichiometry between the target and the sample surface. Target to sample stoichiometry in evaporative techniques are not retained because of different vapor pressures of each material thereby affecting the deposition rate. A KrF laser is pulsed between frequencies of 1 to 50 Hz while the

target is rotated. With a pulse energy on the order of 1 J, a vacuum of 10^{-6} Torr, and

partial pressures of oxygen or other gasses in the mTorr range, a plume, or cloud of

ablated material forms for each laser pulse as depicted in Figure 1-3(a). The sample is

positioned near this plume, which ensures a high deposition rate, but large material

chunks will land on the sample if positioned closer than about 1 cm. Because of the

plume size of about 1 cm, PLD is limited to small samples sizes and has been used

chiefly in research laboratories.
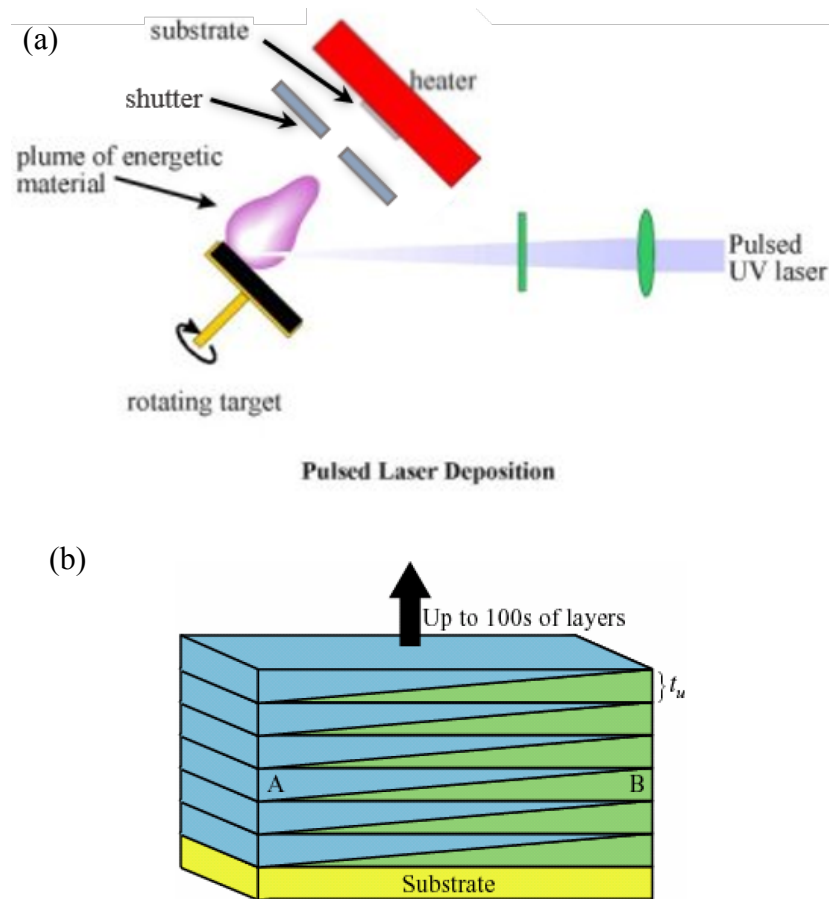
Figure 1-3 (a) Diagram of experimental setup for PLD adapted from [35]. (b) Schematic of layer-by-layer PLD synthesis method. The thickness of each layer is t_u [36].

This relatively new physical vapor deposition technique was discovered in the 1980's and since its successful growth of superconducting $YBa_2Cu_3O_7$ films [37], it has gained in popularity for growing high quality complex oxide thin films of ferroelectric [38] and colossal magnetoresistance materials [39]. Moving shutters and multiple target carriages have been developed in order to allow composition gradient films using PLD. Composition spread films are fabricated by using a layer-by-layer method as depicted in Figure 1.3(b). Each layer, or wedge, has a thickness t_u which is typically less than 0.5 nm to guarantee intimate atomic mixing of the two constituent materials, A and B. In this way, PLD is also amenable to combinatorial investigations [40], [41].

1.3.3 Magnetron Sputtering

Magnetron sputtering gets its name from the fact that magnets are used to enhance the efficiency of the sputtering process. Sputtering is where a large voltage is applied between the target material to be deposited and the sample. In the presence of a gas medium such as Argon (Ar) and a strong voltage, the Ar is ionized and a plasma of electrons, Ar^+ ions, and target atoms give the characteristic glow associated with sputtering. The Ar^+ ions are then accelerated towards the target by the voltage and bombard the target surface ejecting target atoms at an atomic scale. This process is called sputtering and can deposit metals or insulators. A low enough pressure, or high enough vacuum in the mTorr range must be achieved for practical depositions rates. The pressure decides the mean free path of the target atoms being sputtered and thereby affects the deposition rate. Figure 1-4 shows the basic components of the sputtering system.

The plasma itself has a very high temperature and a slight heating of the sample (<10°C) is expected, but the temperature difference between the plasma and the sample is such that the film deposits in a quenched state. Additional post annealing crystallizes the film to achieve thermodynamically stable states.
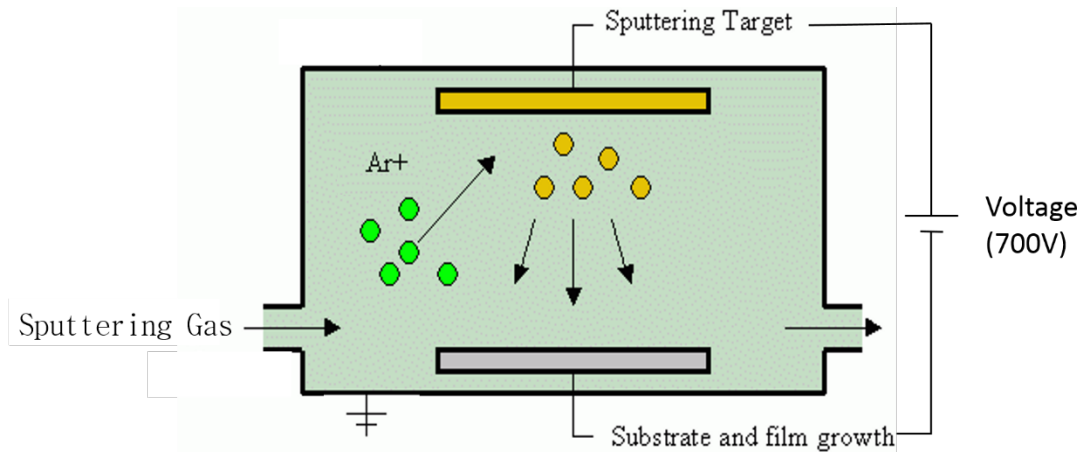
Figure 1-4 Sputtering schematic showing basic components of the sputtering chamber.

Sputtering has been applied in combinatorial investigations of metallic alloy systems [10], [29], [42], [43] where the sputtering guns have a natural deposition profile used to obtain composition gradients as depicted in the left of Figure 1-5. Natural just means that the deposition profile is not artificially changed with shutters or masks and is instead a consequence of the geometry of the sputter gun and the target/sample distance. Co-sputtering is implemented in this dissertation where three spatially separated guns (X, Y, Z) are simultaneously depositing and achieve intimate atomic mixing in the as-deposited film. The masking scheme for the 3-inch silicon

wafers and the corresponding ternary composition diagram is also shown in Figure 1-5.
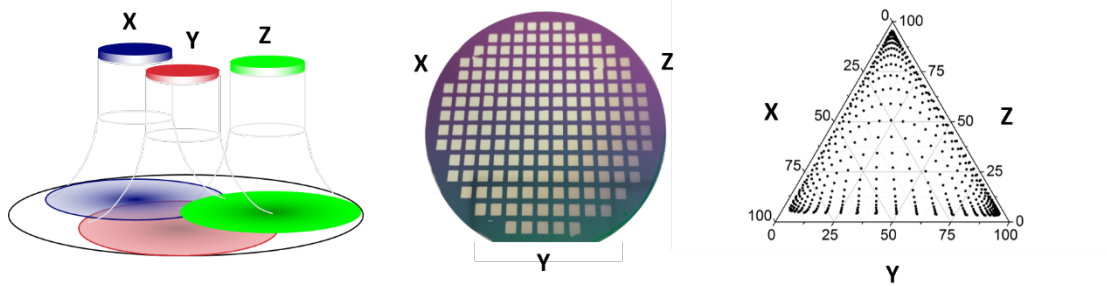
Figure 1-5 Ternary sputtering scheme showing arrangement of targets of possible materials X, Y, Z on the left. Middle shows the arrangement of the target centers around the 3-inch silicon wafer and the mask pattern used to designate individual samples. Right shows the ternary composition diagram where the ternary is largely covered in this representative data.
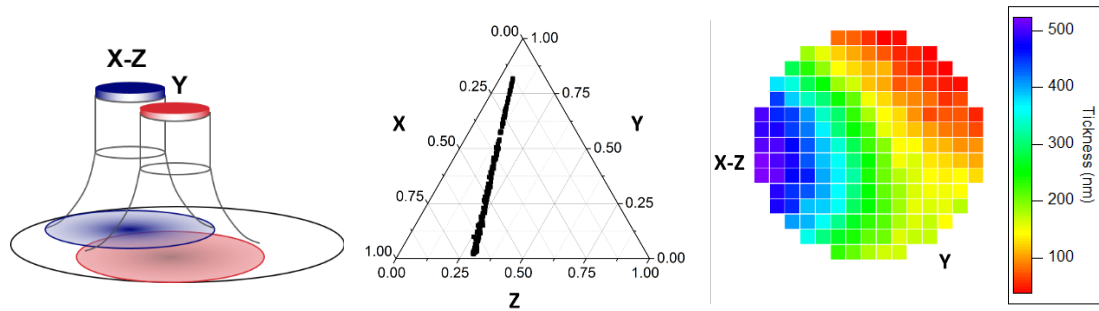
Figure 1-6 Natural thickness gradient sputtering scheme showing a binary gun arrangement (left), binary compositions mapped on the ternary (middle), and the color mapped thickness gradient across the wafer position (right).

1.3.3.1 Natural Thickness Gradients

Natural thickness gradients are also possible due to the non-uniform deposition gradient of a sputtering gun. Using only two of the guns in the three-gun

14

chamber, depicted in the left of Figure 1-6, a natural thickness gradient can be achieved while still having a quasi-ternary composition spread. This is possible with the use of a two element alloy target (X-Z) and a single element target (Y). The composition gradient is then limited to a line in the ternary diagram as shown in the middle of Figure 1-6. The thickness map is also shown where there is a strong thickness gradient perpendicular to the line between the two target positions providing a thickness ratio of 10:1 between the two sides of the wafer.

1.4 High-Throughput Measurement

The crux of the combinatorial method is developing quick and accurate measurement techniques for the large number of samples created in a single library. If even a single step of characterization is required in the traditional serial and manual method, this becomes a laborious, time-consuming, and unfeasible task. The ideal high-throughput measurement is parallel or rapid serial measurement in an automated way that is reliable. In this dissertation, corresponding measurement techniques to understand the composition, structure, and function relationship are implemented using wavelength dispersive X-Ray spectroscopy (WDS), synchrotron X-Ray diffraction, and magneto-optical Kerr effect (MOKE), respectively. In addition, combinatorial application of X-Ray magnetic circular dichroism (XMCD) was developed with our partners, Elke Arenholz in Berkeley, California at the Advanced Light Source, Lawrence Berkeley National Laboratory. XMCD offers a unique magnetic characterization tool that is both quantitative and element sensitive. We will review the basics of XMCD but no results will be presented.

1.4.1 Wavelength-Dispersive X-Ray Spectroscopy (WDS)

WDS operates as part of a scanning electron microscope with an automated x-y-z stage offering the programmable automation necessary to easily measure the 177 samples on a single 3-inch wafer. WDS is able to measure the composition by measuring the wavelength and number of characteristic X-Rays that are ejected from the sample when a high-energy electron beam (15kV) impinges on the sample. When a high-energy electron beam impinges on a sample, electron scattering and photon (X-ray) production occur under the surface in the electron interaction volume. Characteristic X-rays are produced when a high-energy electron strikes a bound electron of the atom and ejects it leaving a vacant energy level. Quantized photons are then emitted when outer-shell electrons fall to fill the empty inner electron shell. Since the energy differences between the higher and lower states are unique for each element, there is a characteristic set of frequencies that each element emits, hence characteristic X-rays.

With a good calibration standard, WDS can offer composition accuracy to within a fraction of a percent. With a beam size of about 30 μm the composition is averaged over within this range. Depending on the elements in the spread, a single position takes about 1 minute to measure. A JOEL JXA-8900 electron microprobe was used in the course of this research pictured below in Figure 1-7.

Figure 1-7 Image of a JOEL 8900 WDS/EDS microprobe used in the composition measurement of the alloy thin film samples for this study. Image from [44].

1.4.2 Synchrotron X-Ray diffraction

Synchrotron X-ray diffraction was used to streamline the process of determining the crystal phase distribution and evolution across the composition and thickness spreads of Fe-Co-V. Synchrotron X-rays refer to the high intensity beams of X-rays that come from nearly light-speed electrons in a synchrotron particle accelerator. The synchrotron beam has about 10,000,000 times the intensity or brilliance of the typical laboratory X-ray source [45] thereby offering faster sample measurement and higher quality data. Synchrotron radiation is the electromagnetic radiation emitted when charged particles (electrons) are accelerated radially like in a synchrotron particle accelerator. Insertion devices like wigglers can further intensify the radiation using a series of magnets designed to periodically deflect the beam from the many magnetic dipoles and thereby increasing the energy of radiation.

17

The synchrotron beam line 1-5 at Stanford Linear Accelerator Center (SLAC) National Accelerator Laboratory was used for data collection in this work. Beam line 1-5 is a wiggler beam line with a custom end-station equipped with an automated scanning stage for fast stepping between sample positions and can be set up in reflection or transmission modes. As a comparison of data acquisition speed we also used a standard laboratory Bruker D8 X-ray diffractometer with an area detector and automated stage to carry out combinatorial measurements. The laboratory diffractometer typically takes 72 hours of measurement to acquire spectra on a 177 sample combinatorial library. The same library can be measured in less than 2 hours at SLAC. Therefore, bringing a dozen libraries to SLAC is a good use of time and provides high quality data.
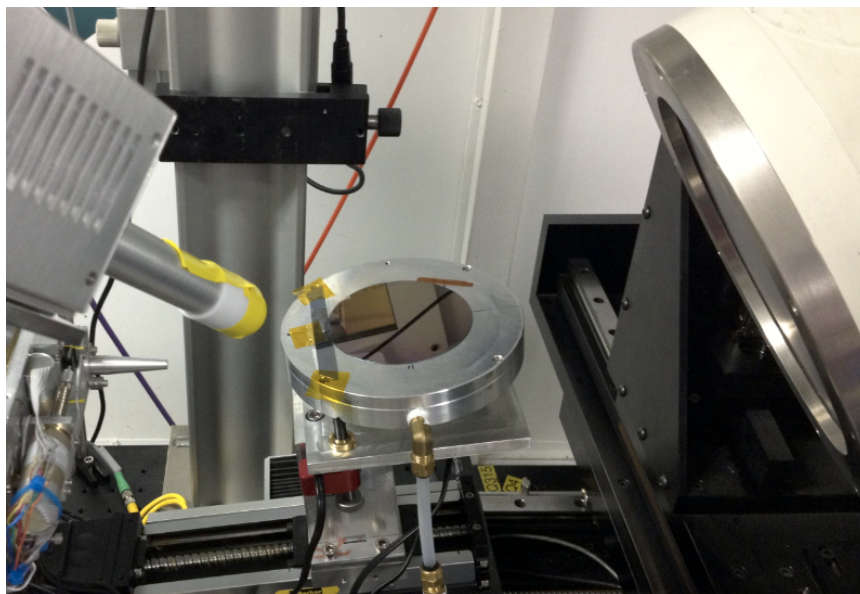
Figure 1-8 Reflection setup for rapid structural mapping of combinatorial wafers using synchrotron radiation at SLAC. The beam can be seen entering from the left where it diffracts off the wafer in the center and diffracted beams hit the detector at the right.

Figure 1-8 shows an image of the actual synchrotron sample holder with a wafer mounted in reflection mode. The beam enters from the left side while the Pilatus area detector is on the right side. The large amount of data collected in synchrotron were analyzed automatically using either WxWindows Diffraction Integration Tool or Fit2D for integration of diffraction images into diffraction patterns, and CombiView for clustering analysis.

The principles of X-ray diffraction are the same for the synchrotron radiation where diffraction of periodic atomic planes occurs when Bragg's law is satisfied:

$$2d \sin\theta = n\lambda. \tag{1}$$

d is the lattice spacing between periodic planes, θ is the angle between the incident X-ray beam and the atomic plane, n is an integer, and λ is the wavelength of incident X-rays. The wavelength used in the present study was $\lambda = 0.7514$ Å.

1.4.3 X-Ray Magnetic Circular Dichroism (XMCD)

XMCD signal is measured by finding the difference in absorption of left and right circularly polarized X-rays by a magnetic sample. Magnetic ions absorb different amounts of radiation depending on the direction of the polarization and so the technique gives information about the element specific magnetic properties [46]. The background is provided, however results on our novel combinatorial XMCD technique will not be presented. XMCD gained traction in the 1980's by observing XMCD signal in the rare-earth elements, iron, and nickel, after a number of failed attempts. The technique has been growing rapidly ever since, now including the study of organics [46].

The technique requires circularly polarized X-rays, a synchrotron beam line ensuring the X-rays are monochromatic, ability to magnetize the sample, and an X-ray absorption detection system. The basic components are shown in Figure 1-9 where three modes of operation are possible: transmission, fluorescence, and electron yield. Transmission mode is made possible by detecting the incoming (I_0) and outgoing X-rays (I), but is limited by the sample type. For example, with thin films, a large signal will come from the substrate and hamper detecting of the thin film signal. Fluorescent X-rays (I_f) are emitted from the sample and also have information about the polarization making fluorescence mode useful for when samples are not conductive (for electron yield mode) and are not suitable for transmission mode, like magnetic oxides. Finally is electron yield mode which detects spin-polarized photoelectrons (I_c) which are stimulated by the incident X-rays.
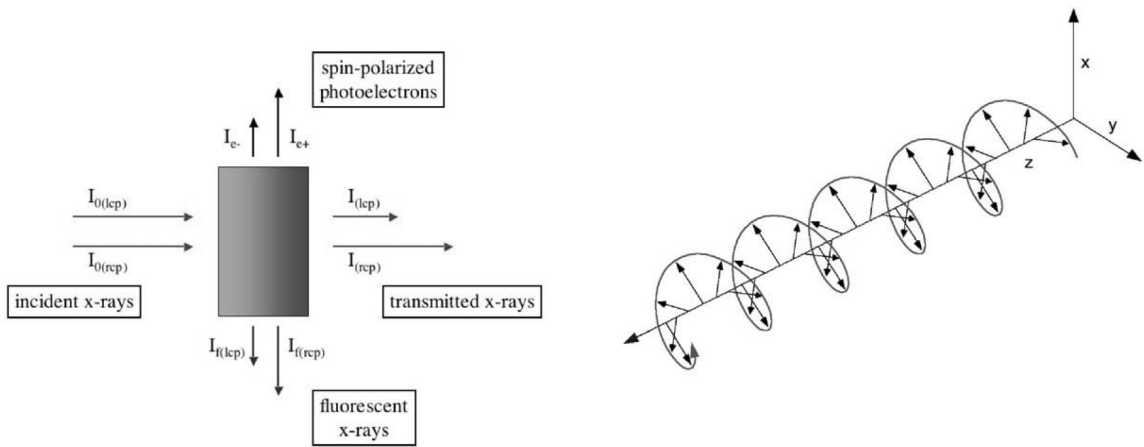
Figure 1-9 (Left) Schematic of XMCD experiment. I_0 is incident beam intensity; I is the transmitted intensity while I_f and I_e are the intensities of the emitted fluorescence and photoelectrons respectively. (lcp) is left circularly polarized and (rcp) is right circularly polarized. (Right) Illustration of the electric field direction along the propagation axis for right circularly polarized light. Figure from [46].

Electron yield mode is compatible with conductive magnetic thin films. One difficulty with electron yield mode is that the photoelectrons are only emitted from the top 2.5-5 nm and so it's very sensitive to oxidation and surface states. To reduce the effects of oxidation, a thin capping film is often necessary for oxidizing films like iron and cobalt. Figure 1-10 shows an example of X-ray absorption spectra (XAS) on the top and an XMCD spectra on the bottom. The two XAS spectra for opposite magnetic field are plotted as μ^+, and μ. They are then subtracted to get the XMCD spectra. The end-station at the Advanced Light Source in Berkeley can measure samples of about 1 x 2 inches using magnetic fields up to 2 Tesla.
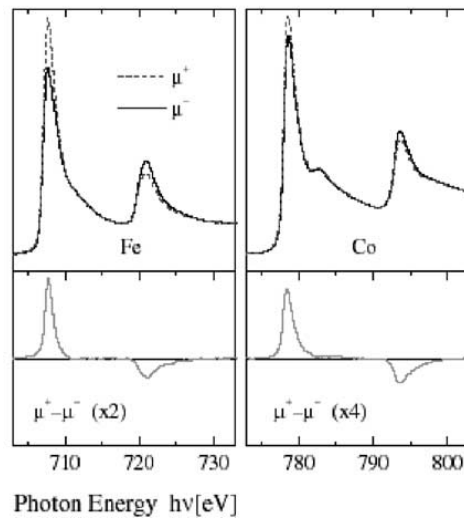
Figure 1-10 Example XAS (top) and XMCD (bottom) spectra. The spectra at opposite magnetic fields is written as μ^+, and μ. Figure from [46].

1.4.4 Magneto-Optical Kerr Effect (MOKE)

MOKE meets the requirement for rapid screening of magnetic properties because of its ability to non-destructively measure magnetic thin films in an

21

automated way. MOKE operates by the Kerr effect where light that is reflected from a magnetized surface can change in both polarization and reflected intensity. The effect is from an anisotropic permittivity where the permittivity affects the speed of light in a material thereby changing its polarization direction. MOKE uses polarized laser light and a sweeping magnetic field to non-destructively measure magnetic hysteresis loops across composition and thickness variations. MOKE has been previously used in combinatorial studies of exchange coupled soft and hard magnetic thin films [31], half-metallic ferromagnetism in Co-Mn-Ge system [47], among other magnetic systems [48], [49].

Combined with a programmable x-y stage, MOKE becomes a practical high-throughput serial screening method for combinatorial libraries in this study of Fe-Co-V alloys. The maximum applied field is over 5 kOe, which was enough to saturate the Fe-Co-V thin films in-plane. Each hysteresis loop takes about 10-15 minutes for good quality data like as in Figure 1-11, and is completely automated using LabVIEW software after calibration and setup. MATLAB programs have been written to also automate the visualization of hysteresis maps, the analysis of coercive fields, switching fields, and clustering of hysteresis loop data to gain additional insights into subtle trends in the hysteresis data across composition or thickness variation. These points are discussed in Chapter 3.

Our MOKE setup used a 635-nm laser beam (Blue Sky Research, CLAS-635-025-WL00) that was then shone through a polarizer and focused onto the magnetic sample. The reflected beam then goes to a cross-polarizer and then the intensity detector. We used the polarizers to minimize the signal read by the detector so that

any change in polarization due to the sample would read as a change in intensity. The amount of polarization change is proportional to the magnetization so that as the field sweeps, magnetic hysteresis loops can be measured to learn about relative magnetization and coercive fields. Because of the small polarization changes involved, a light chopper operating at 1,000 Hz, and a lock-in amplifier synchronized with the chopper frequency is used to detect the small signal. LabVIEW was used to automate the system for averaging over seconds for each data point and operating the scanning stage for automated measurement. An example of the magnetic hysteresis loop data from MOKE is shown in Figure 1-11. The maximum fields that the electromagnet on this particular setup can reach are 5 kOe.
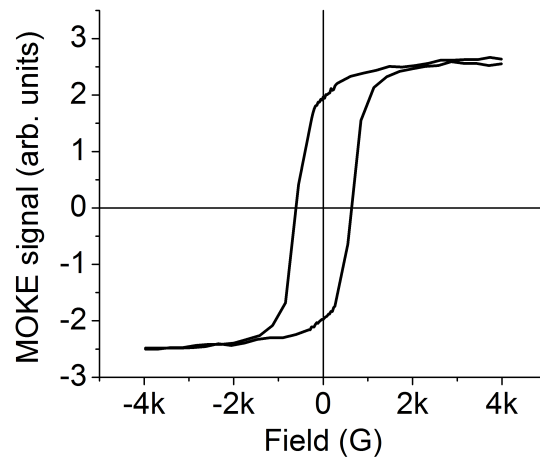
Figure 1-11 Example MOKE hysteresis loop of Fe-Co-V showing the magnetic field range and quality of the data.

The basic components of the MOKE setup used in this study are displayed below in Figure 1-12. An image of the actual scanning MOKE setup in polar mode is given in Figure 1-13. Using either the longitudinal or polar MOKE setup, the

23

hysteresis loops with applied magnetic field can be measured in-plane (IP) or out-of-plane (OOP) of the thin films, respectively. The gap between the magnets is just over 3 inches so in order for the scanning of the full wafer in the longitudinal (IP) mode, the wafer needed to be cut into three pieces. For the polar mode, the whole wafer could be measured at once. Because the wafer needed to be separated into pieces for IP measurements, it's imperative that all other measurements requiring the wafer to be in one piece have been carried out.
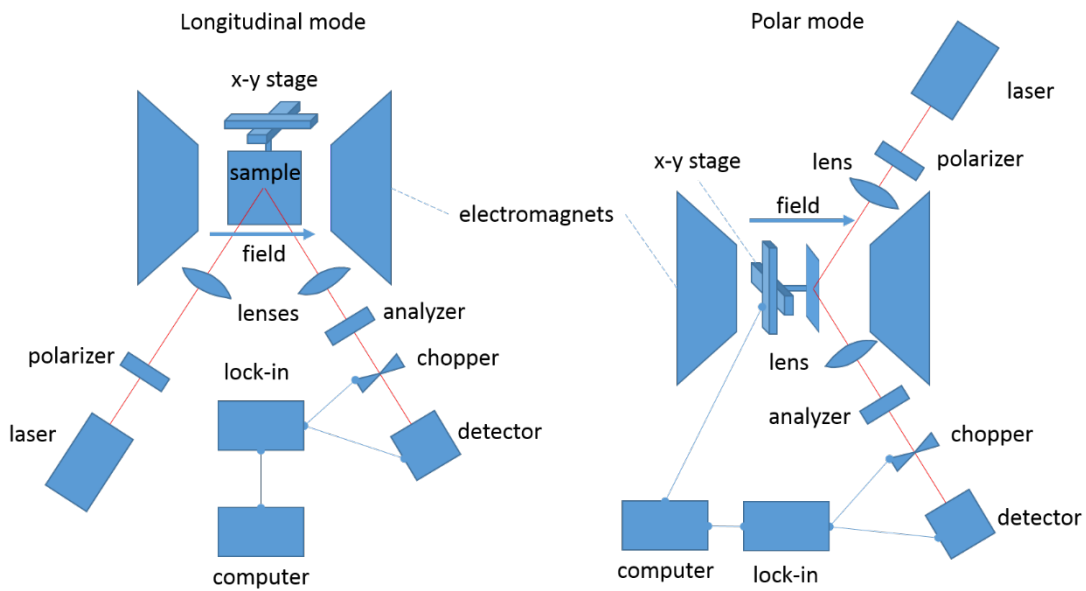
Figure 1-12 MOKE setup on left for measuring in-plane (longitudinal) and on right, measures out-of-plane (polar) magnetic hysteresis loops. "lock-in" refers to the lock-in amplifier. Solid lines with circle arrows indicate hard wire connections while dashed lines point to labeled item. Red lines indicate the laser path. Items are not drawn to scale.

(a)

(b)
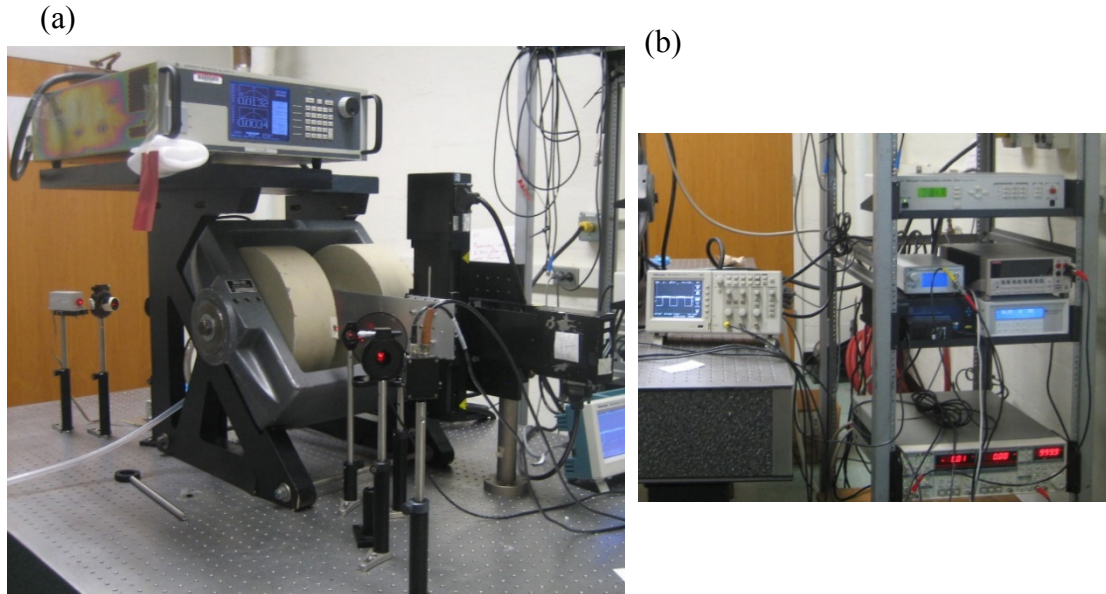
Figure 1-13 Images of the scanning MOKE setup where (a) shows the MOKE in polar mode with the power supply at the top, laser at the far left, and the electromagnet at center. (b) MOKE electronics including the oscilloscope (left), stage controller (top right), chopper controller (beneath), gauss probe to measure magnetic field, and the lock-in amplifier (bottom).

1.4.5 One-by-one Vibrating Sample Magnetometry (VSM)

Unfortunately not every measurement has yet found its combinatorial high-throughput form. In some cases we still need to resort to traditional one-by-one measurement to attain accurate and trusted data. The vibrating sample magnetometer is one of those techniques we needed for confirmation of magnetization in our combinatorial study. The operation of VSM uses pick-up coils to measure the induced voltage from the magnetic field of the vibrating sample as depicted in Figure 1-14. The pick-up coils are frequency matched with the vibrating frequency of the sample holder to increase signal to noise ratio. As different magnetic fields are applied by the electromagnet the signal from the pick-up coils is averaged over about one second for

25

each field and recorded thereby forming a hysteresis loop for ferromagnetic materials. The system must be calibrated with a known standard, in this case a nickel sphere provided by NIST. The fields from the electromagnet are measured with a gauss probe that is situated directly in front of the electromagnet face. We used a Lakeshore VSM 7407 for the measurement in this work. The accuracy of this system is less than one percent with a sensitivity of 1 μemu (micro e-m-u, electromagnetic unit). The maximum applied magnetic field for the system is 2 Tesla.
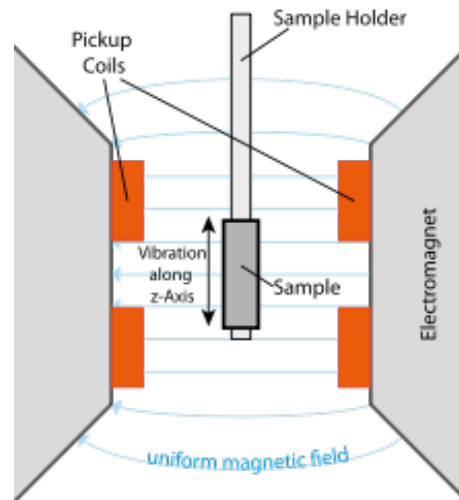
Figure 1-14 Components of the vibrating sample magnetometer (VSM).

1.5 Informatics for Data Mining and Visualization

The necessity of analyzing and processing data sets of 10's of gigabytes created in this combinatorial study prompted the use of digital approaches to visualize and perform data mining techniques. For example, the analysis of X-ray spectra is a time consuming endeavor even for a single spectra. When dealing with hundreds, or

thousands of spectra, it is impossible to individually inspect each one, so data mining techniques are highly desirable. The goal of using informatics in materials science is to discern structure, function, and composition relationships rapidly and reliably. As a first step approach to discerning composition/structure trends we used an in-house software suite developed in MATLAB by Christian Long to handle daily visualization of ternary compositions, X-ray diffraction spectra, and hierarchical clustering [41]. The use of machine learning techniques like hierarchical clustering and non-negative matrix factorization (NMF) in this research is part of a trend in the academic, commercial, and government sectors as huge amounts of data are now gathered on a routine basis. The analysis of these data is part of a growing demand to predict phenomenon, understand highly complex systems, and discover and improve existing material systems.

In this section we will review some basics of hierarchical clustering and NMF to give insight into the later sections that utilize these techniques to discern composition, structure, and function relationships in the Fe-Co-V system. In particular we apply NMF to understand the relationship between thin film thickness, composition, crystal phases, and magnetic properties.

1.5.1 Hierarchical Cluster Analysis

After hundreds of X-Ray spectra are gathered, hierarchical cluster analysis (HCA) sorts the spectra into groups to allow the rapid discovery of the distribution of crystal phases on the ternary composition diagram. Each group then represents a similar crystal structure hence giving information about phase boundaries when plotted on the ternary. Using HCA turns the arduous analysis of hundreds of spectra

and identification of crystal phases into a much shorter analysis of just a few spectra. HCA is usually presented in a dendogram that represents groupings in a branching tree-like diagram. An example of a dendogram is shown in Figure 1-15 where each vertical line represents an X-ray spectrum, and the height of horizontal lines connecting them represent how similar the spectra are. This type of clustering analysis is used in this dissertation to rapidly identify regions of composition space and/or thin film thickness that have similar crystal structures, particularly having similar X-ray spectra. HCA has been previously used in combinatorial experiments to analyze X-ray spectra [50], Raman spectra [41], [51], ferroelectric hysteresis loops [41], and gas sensors [52].
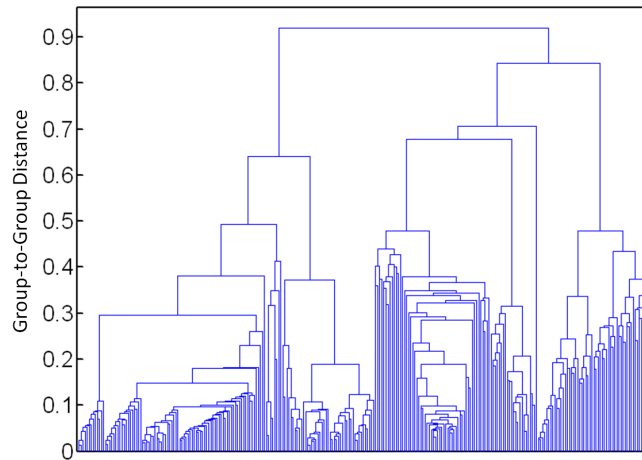
Figure 1-15 Example of a dendogram from HCA where each vertical line represents a spectrum and the distance between groups is on the left axe. Figure from [53].

The particular method of HCA used here is the agglomerative type which means each object, or X-ray spectrum, is initially taken as its own group and based on its similarity to others, they are grouped together until only one group remains. A

distance metric is used to determine the similarity between groups defined as $D = \frac{1}{2}(1 - C_{xy})$, where C_{xy} is the Pearson correlation coefficient between the two spectra. The Pearson's correlation coefficient is defined as follows:

$$C_{xy} = \frac{\sum_{i=1}^{n}(x_i - \bar{x})(y_i - \bar{y})}{(\sum_{i=1}^{n}(x_i - \bar{x})^2 \sum_{i=1}^{n}(y_i - \bar{y})^2)^{1/2}}, \tag{2}$$

where x_i and y_i are the diffraction intensities of two spectra at a given diffraction angle, and n is the number of angles at which the diffraction intensity is measured. A number of other distance metrics can be used including Euclidian, Spearman, and others depending on your application.

Comparing XRD spectra

C_{xy} = 1
D=0

C_{xy} = 0
D=.5

C_{xy} = -1
D=1
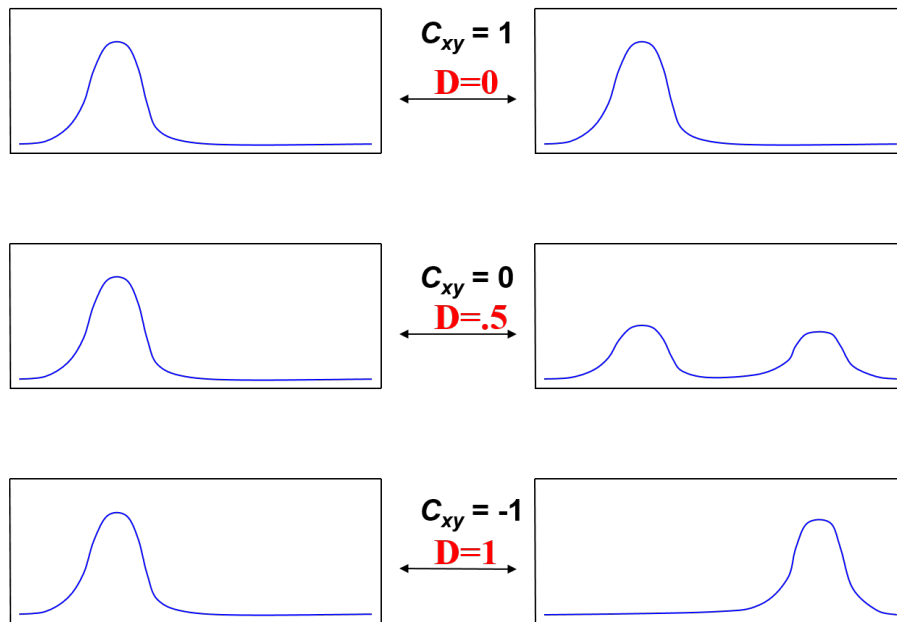
D = distance metric

Figure 1-16 Schematic of Pearson correlation coefficient and distance metric values with their corresponding X-ray diffraction spectra.

All the spectra are compared in this fashion and the correlation coefficients are collected in a matrix C, which can then be converted to a distance matrix D, as per our previous distance metric definition. Hence, a distance D of zero (0) between two spectra is considered as identical spectra (with a Pearson coefficient of one (1)) and would suggest that the X-ray spectra peaks match up perfectly, indicating it's very likely the crystal structures are the same. A distance D of one (correlation coefficient of -1) indicates they are very unlikely to share the same crystal structure because of their dissimilarity in X-ray spectra peak position and intensity. Different cases are depicted schematically in Figure 1-16.

Now that the distance matrix D holds all the information necessary to group our data together, how do we understand those relationships? Let's go back to the dendogram to get a more intuitive understanding. First, we take the two most similar spectra and put them in a group together. This is accomplished by connecting them in the dendogram with a horizontal line at the height corresponding to the distance, D, between them. Next, we need to determine the distance of this group of spectra to all of the other spectra. This group-to-group distance is calculated by the group average linkage method that takes the average of the distances from all of the members of the first group to all the members of the second group. This is the method for making the dendogram in Figure 1-15. Agglomeration of the groups is repeated as more dissimilar groups are merged until eventually, there is only one group at the top of the dendogram.

If we were to stop merging groups at a threshold group-to-group distance, then a number of groups would remain. The threshold group-to-group distance is

called the cut level. One can adjust the number of groups by adjusting the cut level as the colors show in Figure 1-17. But how do we decide where the cut level should be? Going back to the distance matrix D, we want to be able to visualize this correlation matrix in three-dimensional space, but the dimensionality of D is too high. This is the classic problem of reducing the dimensionality of a data set, which will not be covered here, but for this work, we use multi-dimensional data scaling (MMDS). MMDS allows us to visualize the best possible three-dimensional approximation of the distribution of points in the distance matrix, D. For an example set of data, the three dimensional representation of the distance matrix as approximated by MMDS appears in the middle of Figure 1-17. An animation of the plot can also be viewed at www.combi.umd.edu.

The MMDS analysis allows us to qualitatively create groups by eye to verify the work done by the average linkage method. If well separated clusters are formed in the MMDS plot, then there should be a cut level where there is a large step in the linkage height. Figure 1-17 shows different cut levels of 0.87, 0.83, and 0.55. At 0.55, the clusters form more or less spherical clusters of green, purple, and yellow, and two "boomerang" shaped clusters of red and blue.

MMDS analysis in Figure 1-17 not only shows spherical clusters indicating groups of spectra with the same crystal structure, but there are points that form arc-like distributions, meaning the spectra are related to each other but undergo some systematic change. This change could be a shift of an X-ray peak in a subset of samples indicating a change in lattice parameter, or some slowly varying crystal phases giving different mixtures of crystal structures. These gradual changes in

31

spectra are the types of problems not handled well by HCA giving false phase boundaries. NMF is another method explored next, to address these shortcomings in HCA.

Using Clusters to Identify Boundaries in Composition Space
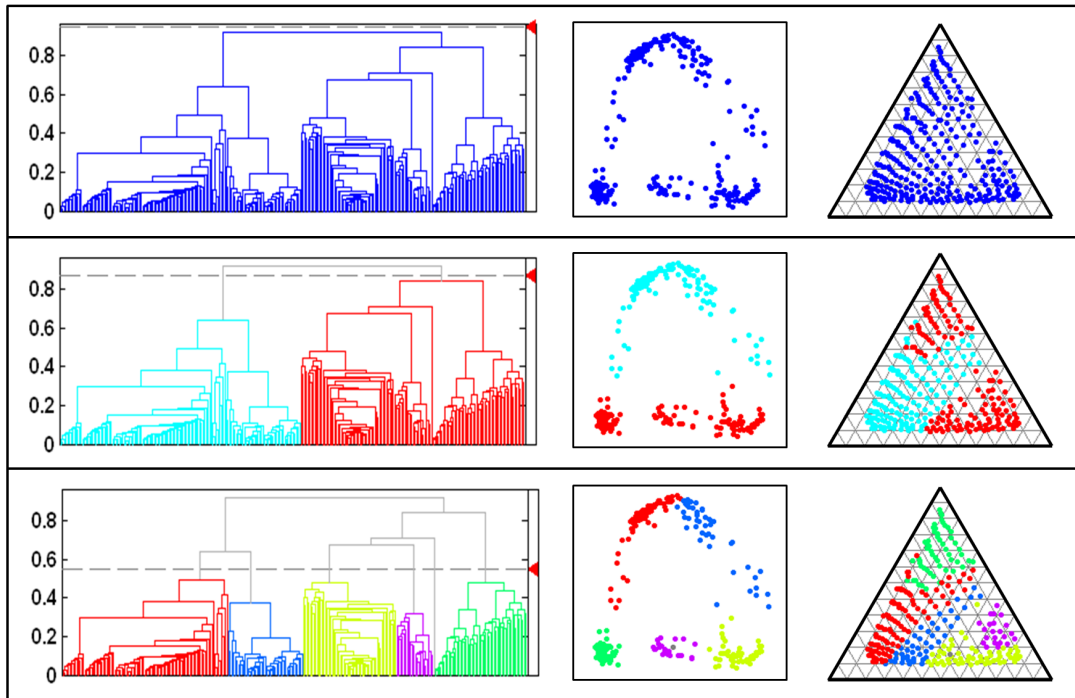
Figure 1-17 Example of different cut levels showing the dendograms (left), MMDS analysis (middle) and the corresponding groups on the ternary diagram (right). Each color represents a group, and each point represents a diffraction spectrum in the MMDS analysis and ternary diagram. The distance is related to the similarity metric defined for MMDS analysis. Figure from [53].

1.5.2 Non-Negative Matrix Factorization

Another method to address the problem of analyzing hundreds of X-ray diffraction (XRD) spectra from a combinatorial thin film library is non-negative

32

matrix factorization (NMF). NMF can identify the unique XRD spectra present in a materials system and quantify how much are contained in each experimental spectra. The advantage is that the user need only analyze a small number of the unique XRD spectra to identify the component phases of numerous mixtures present in the combinatorial library. NMF has only recently been applied to XRD spectra [50] and was previously used for image [54] and document [55] processing as well as analyzing spectral data for satellite material identification [56].

XRD spectra are considered non-negative because they contain only positive values in the series of diffraction peaks versus angle or d-space. Borrowing from signal and image processing, NMF uses deconvolution of a large number of spectral patterns into a small number of basis patterns. Deconvolution is the reverse of convolution where in convolution the two functions are overlapped at different translations between each other and a third function describes the area of overlap between them. After deconvolution, the experimental patterns are then described as a weighted superposition of the deconvolved basis patterns.

NMF applies particularly well to XRD spectra because the basis patterns can be interpreted directly as diffraction patterns unlike when trying to apply principle component analysis (PCA) which gives negative values in the basis patterns [53]. The method involves a matrix problem where the XRD data are arranged in an m-by-n matrix, Y, with $m = 177$ as the number of compositions and n is the number of angles that the diffraction data was recorded at. Typically a spectra will range about 35 degrees in 2θ and are measured at $0.005°$ giving $n = 7,000$. NMF is then used to

obtain a factorization of Y into the product of the smaller matrices A and X such that they are constrained to be non-negative as below:

$$Y = AX + E, \text{ Where } A_{ij} \geq 0, \text{ and } X_{ij} \geq 0. \tag{3}$$

Noise or error in the experimental data can be accounted for by the error matrix E, which can contain negative values. Figure 1-18 shows a schematic of the equation where the size of matrix A is m-by-r, X is r-by-n, and matrix E is m-by-n. The rank of the factorization, r is chosen by the user as the number of basis patterns to be extracted from the experimental data. This decision should be based on the number of expected pure phases present in the analysis and requires an experienced user's intuition.
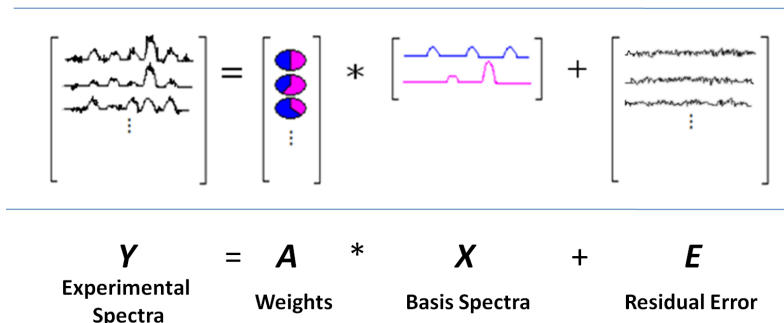
Figure 1-18 NMF is able to deconvolve the experimental spectra into a smaller number of basis spectra. These basis spectra can be superposed by the weights to give the experimental data as depicted in the schematic. Figure from [53].

Crystallographic databases of known crystal phases like the Inorganic Crystal Structure Database (ICSD) [57] can help identify the basis spectra as known pure crystal phases. The method will be applied particularly to the natural thickness

dependent library of Fe-Co-V where X-ray spectra have a combination of shifting peaks and mixed phases that give poor results with HCA. This work will be discussed at the end of Chapter 3.

1.6 Examples of Rapid Mapping of Magnetic Materials

Before we go into the details of our investigation, we would like to provide two examples of the power of studying magnetic materials with the combinatorial method. We present two examples below, however, a number of successful examples exist including the discovery of giant magnetostriction in annealed Co-Fe films [10], the investigation of the magnetostrictive Fe-Ga-Al system [9], among others [24], [31], [58].

The first example presented is part of our group's larger search for rare-earth free permanent magnets in the Fe-Co-X compounds where X are refractory transition metals. In this case, X is W (tungsten), which shows promise as a rare-earth free permanent magnet candidate [59]. The importance of reviewing this Fe-Co-W study is because a similar approach is taken for the Fe-Co-V system where we use switching field dependence to understand the magnetization reversal mechanism. The second example is the combinatorial investigation of ferromagnetic shape-memory alloys in the Ni-Mn-Ga system [8].

1.6.1 Fe-Co-W Candidates for Rare-Earth Free Permanent Magnets

The first example that exhibits the effectiveness of the combinatorial method to rapidly map magnetic and other structural properties is the systematic investigation of the Fe-Co-W system [59]. Detailed theoretical motivation for this study will be discussed later (Section 2.6), but for now we focus on the successful application of

the combinatorial thin film method to understand structure/function relationships and the angular switching field strategy used to understand the magnetization reversal mechanism. 400 nm composition spread films of Fe-Co-W were co-sputtered on 3-inch Si wafers using the above described sputtering scheme (Section 1.3.3). In addition to studying the composition dependence of magnetic properties, the temperature dependence of the crystal structure was studied by fabricating libraries with different annealing procedures as follows: (1) as-deposited at room temperature, (2) deposited at room temperature and then annealed at 600°C, and (3) deposited at room temperature and then annealed at 700°C. It is extremely difficult to produce hundreds of unique composition samples with a series of different preparation conditions using the traditional one-by-one method. The combinatorial method has the advantage that parallel sample fabrication guarantees identical conditions for each of the libraries.

The wafers were measured with synchrotron X-Ray diffraction to study the composition dependence of the crystal structure. The X-ray diffraction spectra are presented for 4 different W compositions in the top of Figure 1-19. The individual spectra show the evolution of crystal structure with W composition from crystalline body-centered cubic (BCC) for low-W spectra under 7 at% (black and red lines), to the broad peaks of the amorphous samples containing higher W compositions above 17 at% (blue and green). The full-width at half maximum (FWHM) of the (110) X-ray peak was then used as a measure of the crystallinity and mapped on the ternary diagrams in the bottom of Figure 1-19. The boundary between the crystalline and

amorphous regions is sharp and progresses from 10 at% W for the as deposited films, to 20 at% W for 700°C annealed films.
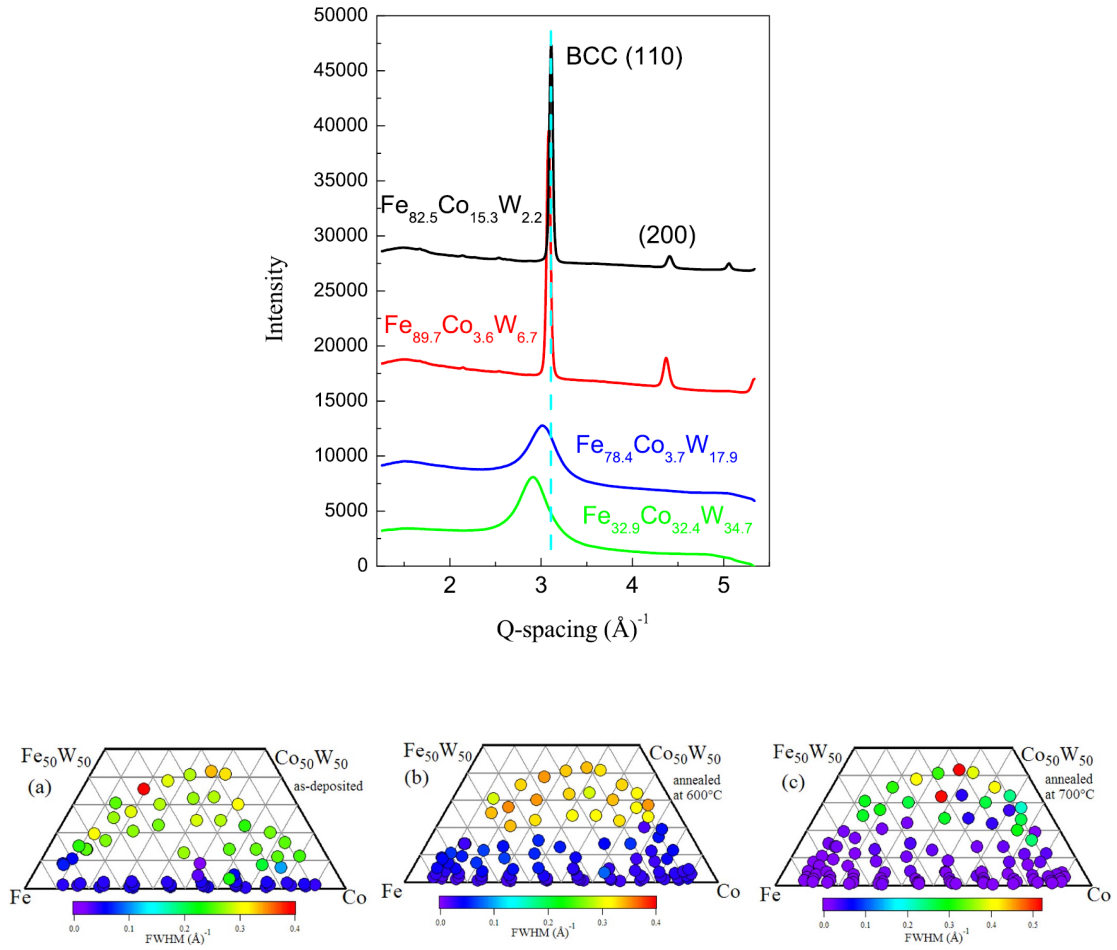
Figure 1-19 (Top) Typical synchrotron X-ray spectra of Fe-Co-W thin films annealed at 600°C with various W contents. (Bottom) FWHM values mapped on the composition ternary of the Fe-Co-W thin film spreads for (a) the as deposited at room temperature state, (b) annealed at 600°C, (c) and annealed at 700°C. Figures adapted from [59].

Now that the structural dependence of composition has been revealed we move on to review the functional property of magnetism in the Fe-Co-W system. Figure 1-20(a) shows typical in-plane (IP) and out-of-plane (OOP) magnetic hysteresis loops where a large enhancement in the coercive field of the OOP loop is noted. Microstructure investigations were carried out with TEM and selected area electron diffraction (SAED). Figure 1-20(b) shows a plane-view TEM image and the SAED pattern of a 2.2 at% W thin film. The film appears completely crystallized in the SAED pattern with a platelet-like microstructure visible in the TEM image. Although the crystallites appear aligned, it only appears that way since the image has such a small field of view. The overall crystals are not aligned over large areas. Figure 1-20(c) shows the plane-view TEM image and the SAED pattern where this 17.9 at% W sample is considered amorphous because of the halo-like rings observed in SAED. Finally, we review the angular dependent switching field study in order to understand the magnetization reversal mechanism and gain insight into the structure and function relationship.

Switching field experiments have been known since the 1940's to reveal important information about how magnets switch or reverse their magnetization [60], [61]. By understanding the nature of magnetic reversal it's possible to focus research efforts appropriately towards improving performance of permanent magnets. Details of the theory are described in Section 2.5 while details of the experimental measurements are in Section 3.2.3. Here, we note the angular dependence of the magnetic switching field and describe its relation to the microstructure in this example.

38
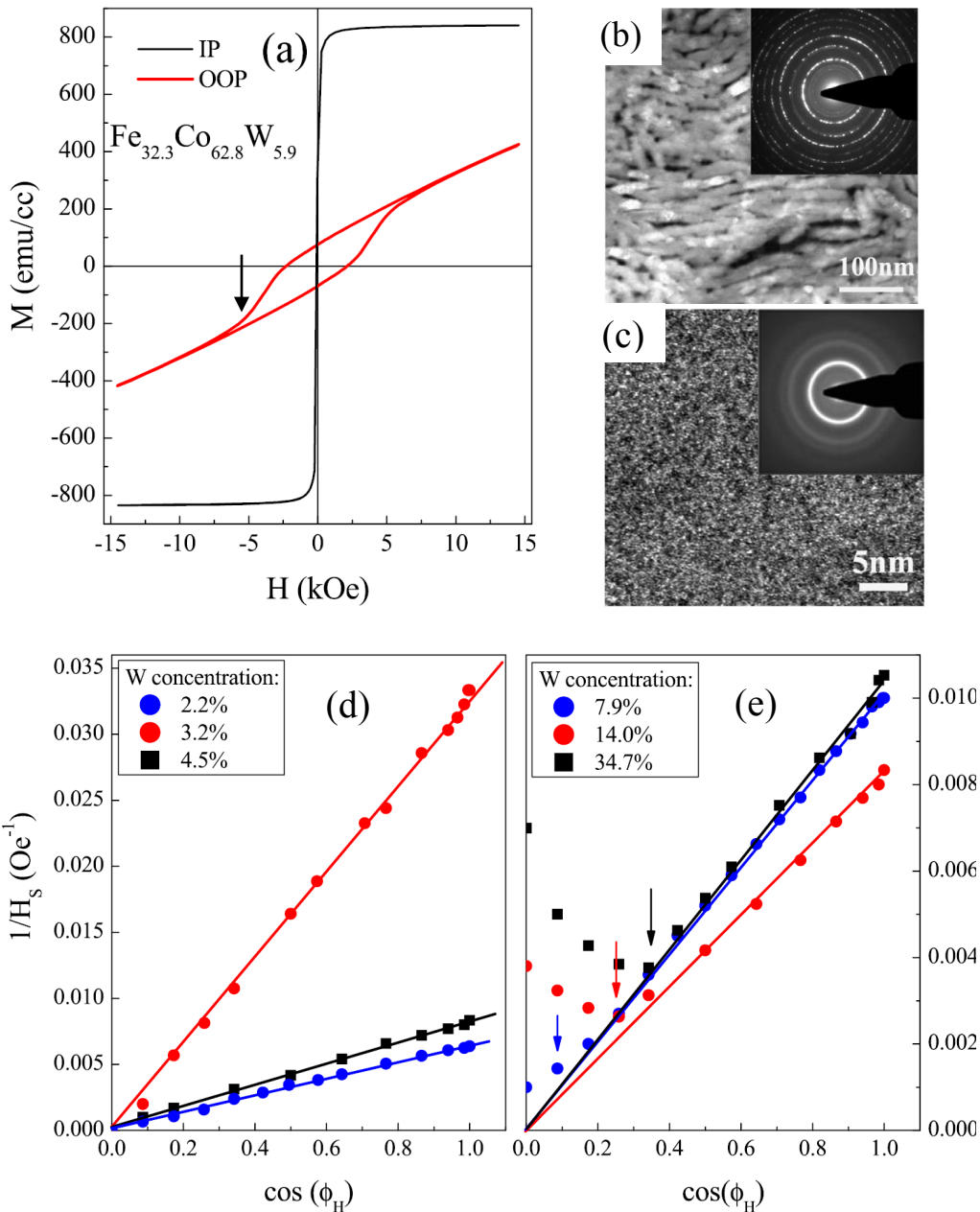
Figure 1-20 (a) Typical out-of-plane (OOP) and in-plane (IP) hysteresis loops of low W containing thin films. TEM images of (b) crystallized region with 2.2 at% W with inset selected area electron diffraction (SAED) demonstrating the crystalline state, (c) amorphous 17.9 at% W where inset SED demonstrates the amorphous state. Angular dependence of inverse H_S for low W concentrations (d) and high W concentration (e). In (d) and (e) inset numbers refer to W compositions. The solid lines are linear fit. The arrows indicate the onset of the H_S and $\cos(\varphi_H)$ to deviate from linear dependence. Figures adapted from [59].

The switching field for the out-of-plane magnetic hysteresis loop is indicated with a black arrow in Figure 1-20(a). Figure 1-20(d) & (e) show the angular dependence of this switching field for different W compositions. It is found that for low W compositions, under about 5 at%, that switching behavior agrees with the Kondorsky model for 180° domain wall motion as in Figure 1-20(d). For Figure 1-20(e), the switching field shows a deviation from the linear dependence, which indicates that both Kondorsky type and Stoner-Wohlfarth type switching are occurring. Stoner-Wohlfarth switching is thought of as coherent rotation of magnetic moments in single domain magnetic particles.

The microstructure associated with the Kondorsky type switching of Figure 1-20(d) was associated with the platelet grains of Figure 1-20(b). This was suggested to be a consequence of the large shape anisotropy from the platelet shaped grains that stand up in the film. The switching mechanism of Figure 1-20(e) with both domain wall motion and coherent rotation was associated with Figure 1-20(c) where the amorphous microstructure would have magnetic grains embedded in an amorphous matrix where magnetizations of particles switch independently and therefore magnetization reversal is achieved by both coherent rotation and domain wall motion.

This detailed study then guides future work on the Fe-Co-W system in order to verify if the platelet shaped grains are in fact contributing a shape anisotropy effect responsible for the increased out-of-plane coercive field. This example of the Fe-Co-W system was provided to give insight into successful application of the combinatorial method for studying magnetic materials and the use of switching field dependence to understand the origin of permanent magnetic properties.

1.6.2 Ferromagnetic Shape Memory Alloys in the Ni-Mn-Ga System

In this second example, we review the investigation of ferromagnetic shape-memory alloys (FSMA) in the Ni-Mn-Ga system [8] to show the effectiveness of the combinatorial method in studying magnetic materials. This work was also performed in the Takeuchi group but the author of this dissertation did not have direct involvement. FSMAs occur in materials that are simultaneously ferromagnetic and reversible martensites, meaning they are shape memory alloys. The strategy then is to use high throughput screening to search for compositions showing both properties. In this FSMA study, composition is varied across a 3-inch silicon wafer where targets of Ni, Mn, and Ni_2Ga_3 are used. Because of Ga's low melting temperature (29°C), a pure Ga content target could not be used. To map the magnetization versus composition, a scanning SQUID (superconducting quantum interference device) microscope was used, while X-ray diffraction was used to map the structure and confirm phase transitions. A novel screening technique used an array of micromachined mechanical cantilevers to detect structural transformation of thin film composition spreads depicted in the left of Figure 1-21.

It was possible to map the bifunctional phase diagram of the Ni-Mn-Ga system using the mechanical and magnetic property maps (right of Figure 1-21). The study found that the well-known Ni_2MnGa FSMA composition is actually part a much larger, unexplored composition region containing reversible martensites which are also ferromagnetic. They also find a trade-off between the magnetization and the martensite transition temperature. For applications, this means
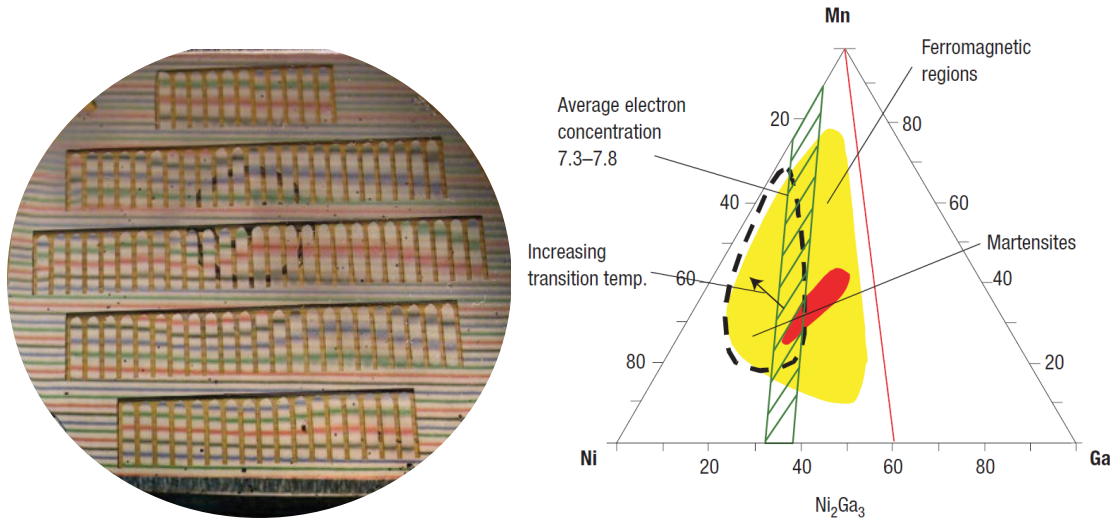
Figure 1-21 (left) Photograph of the Ni-Mn-Ni$_2$Ga$_3$ spread deposited on a cantilever library taken during the temperature dependent measurement. A typical cantilever has an area of 2mm by 1 cm and thickness of 60 μm. The lines are a reflection of an image with colored lines held over the wafer. The shifts in the positions of the lines as a function of temperature are used to detect small changes in local curvature of the cantilever. (right) Functional phase diagram deduced from the Figures adapted from [8].

1.7 Outline of this Dissertation

Part I focuses on the search for rare-earth free permanent magnets starting with Chapter 2 where we introduce the basics of permanent magnetic concepts necessary for the work here. This includes applications, properties, and theories for hard magnetic materials. We introduce the figure of merit used for permanent magnets called the maximum energy product (BH)$_{max}$ and we review some of the particular mechanisms of hard magnetism responsible for the properties in Fe-Co-V alloys. We also use our previous work on Fe-Co-W as a framework for the Fe-Co-V study.

Chapter 3 covers the experimental method and results of the combinatorial study of the Fe-Co-V system. The combinatorial high-throughput methods are

reviewed and results discussed for each. Then the switching field study and the thickness dependent study results are presented and discussed.

Part II focuses on the study of a strain-based composite multiferroic heterostructure of transcritical Permalloy and barium titanate. Chapter 4 begins with background on multiferroics and then we introduce each component of the composite material studied here and its important ferroic properties. We discuss ferromagnetic materials and their property relating strain and magnetism called magnetostriction. Then we describe the magnetic domain structure in Permalloy thin films and review the literature showing the magnetic domain structure is sensitive to strain and thin film thickness. Finally, we review the important properties of the ferroelectric substrate that has a strain modulation over its crystalline surface.

In Chapter 5 we present experimental methods for the preparation of the multiferroic heterostructure. These include preparation of the ferroelectric substrate, deposition of the magnetic thin film, and details of the magnetic force microscopy calibration and measurements. The experimental results are then presented and discussed. Finally, we review the numerical micromagnetic simulations carried out to understand the characteristics of the magnetic force microscopy data. A short introduction is given to the Object Oriented Micromagnetic Framework used in this work and developed by NIST. Results of the simulations and implications for future studies are discussed.

Part I

**Combinatorial Investigation of
Rare-Earth Free Permanent Magnets**

Chapter 2. Introduction to Permanent Magnets

Chapters 2 to 4 focus on exploring Fe-Co-X alloys as candidates to rare-earth free permanent magnets and understanding their composition and thickness dependent structure and properties since ultimately they are to be applied in bulk permanent magnets. In Chapter 2 we review the basic properties of hard magnets and their figure of merit called the maximum energy product $(BH)_{max}$. We introduce some the different kinds of magnetic anisotropies that can contribute to $(BH)_{max}$ including crystalline and shape anisotropy. Strain anisotropy is reserved for Chapter 4 where it applies directly to the strain-based multiferroic heterostructure. The reasoning behind the particular choice of Fe-Co-X compounds and theoretical work on the enhanced magnetic anisotropy of Fe-W and Co-W compounds is discussed. The Fe-Co-V system is introduced and experimental findings are discussed. In Chapter 3 we introduce some principles of thickness dependence in magnetic materials. Finally, experimental results on a natural thickness dependence study are presented and discussed in relation to the present study.

2.1 Hard Magnetic Materials

Magnetic materials for applications are divided into two main groups called soft and hard magnets. Soft magnets are easily magnetized and demagnetized due to their high relative permeability (the change in magnetic flux density per external magnetic field) and low coercive fields. Permeability for soft magnets like Permalloy, a Ni, Fe alloy, can be in the 1000's and coercive fields less than 1 Oe. Soft magnets are used in the cores of transformers, induction type generators, and motors where their ability to quickly and easily change their magnetization distinguishes them from

hard magnetic materials. Hard magnets have coercive fields above 100 Oe and are thus able to resist the action of opposing magnetic fields. Hard magnets are referred to as permanent magnets and are the focus of this dissertation. Permanent magnets find use in permanent magnetic motors, generators, actuators, magnetic latches, and controlling ion beams. Permanent magnetic motors and generators are capable of generating higher torque than induction motors and are more efficient.

2.1.1 Desirable Properties of Permanent Magnets for Traction Motors

The major desirable properties of a permanent magnet are the ability to maintain a high remanent magnetization while under external demagnetizing fields and changes in temperature. Other factors include corrosion resistance and machinability. Temperature stability is of considerable interest to the automobile industry as electric cars rely on high performance rare-earth permanent magnets to reduce weight while maintaining high torque for acceleration all at high operating temperatures around 150°C. The highest performance permanent magnet of today is the $Nd_2Fe_{14}B_2$ (neo) with $(BH)_{max}$ = 50 MGOe, which far outpaces any rare-earth free permanent magnets such as Alnico (5-10 MGOe) or magnet steels (1 MGOe). One undesirable property of neo magnets is the drop of coercive field and remanent magnetization as the temperature approaches the important operating requirement of 150°C (423°K) as shown in Figure 2-1.
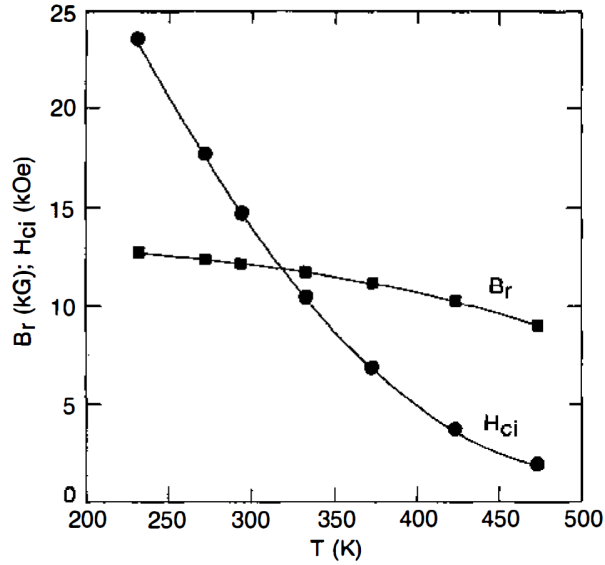
Figure 2-1 Temperature dependence of residual induction (Br) and intrinsic coercivity H_{ci} for a sintered Nd-Fe-B magnet showing the sharp drop in coercive field [62].

Considering temperature dependence for permanent magnets, a minimum T_C of about 300°C is desired for permanent magnets while higher T_C's are desirable. Nd-Fe-B's T_C of about 300°C explains its drastic decrease in magnetic properties above room temperature compared to more stable Alnico with a T_C closer to 550°C. One way that Nd-Fe-B manufacturers address the low T_C is with the addition of Cobalt (Co) and Dysprosium (Dy). Dy imparts a higher T_C while it lowers the magnetization. The addition of up to 5 wt% Dy can reduce irreversible and long term aging losses of magnetization from 70% to less than 10% for 5000 h at 150°C [63], [64].

One way to quantify this change in magnetization over temperature is the temperature coefficient. One can see that all the commercial permanent magnets listed in Table 1 have negative temperature coefficients meaning they lose a certain percentage of their magnetization per increase in temperature. Other permanent magnetic materials like MnBi have positive temperature coefficient for coercivity and

47

is under study in order to take advantage of its unusual properties [65]. One definition for the temperature coefficient of the magnetization, α, where B_r is the remanent flux, T_1 is room temperature, and T_2 is the elevated temperature is given below [64].

$$\alpha = \frac{B_r(T_2) - B_r(T_1)}{B_r(T_1)(T_2 - T_1)} 100.$$

(4)

One can similarly make a temperature coefficient for the coercive field by replacing B_r with H_c in the above equation.

Table 1 Properties of some permanent magnetic materials [66]. Temperature coefficient is reversible and for magnetization.

Product	B_r, kG	H_c, kOe	H_{ci}, kOe	$(BH)_{max}$, MGOe	Max T, °C	Temperature Coefficient, %/°C
Hard ferrite 1	3.8	2.4	2.55	3.4	200	− 0.2
Hard ferrite 2	4.0	3.65	4.0	4.0	200	− 0.2
Alnico 5	12.5	0.680		5.5	450	− 0.02
Alnico 9	11.2	1.375		10.5	450	− 0.02
SmCo$_5$	8.7	8.50	30.0	18.0	250	− 0.04
Sm$_2$Co$_{17}$	10.7	9.75	26.0	26.0	300–350	− 0.03
NdFeB 1	10.0	9.60	41.0	24.0	150–200	− 0.1
NdFeB 2	12.9	12.40	23.0	40.0	150–200	− 0.1

The second desirable property of a permanent magnet is a high remanent magnetization. Magnetization is from the alignment of magnetic moments being in one of three possible configurations of ferromagnetism, ferrimagnetism, or antiferromagnetism. Figure 2-2 depicts these three configurations as 2-D cartoons. In addition, the atomic moment of each constituent also plays a crucial role in determining the total magnetization. For example, when metals like W and V, with strong spin-orbit coupling, are alloyed with magnetic ions like Co and Fe,

hybridization between the elements can have strong and non-trivial phenomenon as discussed in Section 2.6.
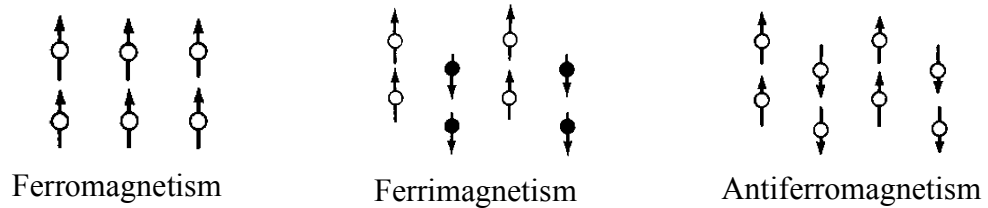
Figure 2-2 Three types of magnetism showing how different atomic magnetic moment configurations can contribute to the total magnetization. Circles represent atoms or ions and arrows represent the net magnetic moment. Open and solid circles represent different atomic or ionic species. Figure adapted from [66].

The interaction of magnetic moments in the solid requires complex first-principle calculations including fully relativistic effects to approach agreement with experiment. These theoretical treatments will be briefly introduced in Section 2.6. In addition, the direct experimental measurement of the contribution of each element is a challenging endeavor, but using relatively new tools like X-ray magnetic circular dichroism (XMCD), it is possible to measure the element specific contribution of magnetic moments to the measured macroscopic magnetization using traditional magnetometry techniques [67]. XMCD does not give quantitative information, but it provide relative magnetic moment so calibration with a standard is required for accurate comparison.

2.2 Basic Magnetic Quantities

The quantities used largely by applications engineers are explained and differentiated from the quantities used by scientists in the research of permanent

magnets. In addition, there is much confusion over units in the field of magnetism because of the ongoing transfer from the ancient centimeter-gram-second (cgs) convention based on forces between magnets, to the modern meter-kilogram-second (MKS) system which is established under the evolving *Système International d'Unités* (SI). I introduce here the basics of both systems but generally expect the reader to be comfortable with both systems using whichever is deemed appropriate throughout the dissertation.

This section on defining magnetic quantities will give the appropriate background for the next section explaining the figure of merit $(BH)_{max}$. The applications engineer in the design of magnetic circuits for motors and generators is largely concerned with the magnetic flux density, or induction (B) in the air gap, compared to scientists who often measure the magnetization M. The air gap is simply the empty space next to the magnetic pole where the magnetic flux outside the magnet can be used to do work. Magnetization in cgs units, or magnetic polarization, I in SI units, is an intrinsic material quantity related to the net number of magnetic moments per weight or volume. B and M are related as below in cgs and SI units where H is the external magnetic field.

$$B = H + 4\pi M \ (cgs) \qquad or \qquad B = \mu_0 H + I \ (SI) \tag{5}$$

For cgs units B, H and M must all be in equivalent units of maxwell/cm^2, but different names are used for each quantity where maxwell/cm^2 is called a gauss (G) when referring to B and oersted (Oe) when referring to H. However, in free space $M = 0$ and hence $B = H$, so it is common to see H expressed in gauss as in this

dissertation. We write M as emu/cm^3 (emu = erg/Oe) and $4\pi M$ in gauss since $4\pi M$ must be equivalent to B and H.

In SI units, magnetization is conceptualized as arising from loops of electrical current such that $H = ni\,(ampere\ turns)/l\,(meter)$ where n is the number of turns with current i, around a solenoid of length l and hence magnetic field is taken in units of A/m. Considering Faraday's law for inductance of voltage due to a changing magnetic field we find that the proportionality constant between the voltage and the changing magnetic field times the current is the permeability of free space, μ_0 or $4\pi\times10^{-7}H/m$ (henry per meter or $V \cdot sec/A \cdot m$). Finally, the magnetic polarization I in SI units is simply the magnetization M (A/m) multiplied by μ_0 which can then be written in units of tesla or μ_0(A/m). With these basic quantities defined we move onto describing the maximum energy product.

2.3 Maximum Energy Product

The single best indicator of performance for a permanent magnet is the maximum energy product (BH)$_{max}$. To understand why, let's consider an open magnetic circuit idealized as a magnetic ring with a gap as in Figure 2-3. We call this a magnetic circuit because a number of analogies are shared with electrical circuits, for example the similarity of the quantities for electric current and magnetic flux. We see that the magnetic poles are labeled north (N) and south (S) as well as the total flux (B_m), the field outside the magnet (H_m), the field in the gap (H_g), and the length of the air gap (l_g). Subscripts m and g then stand for magnet and gap, respectively.
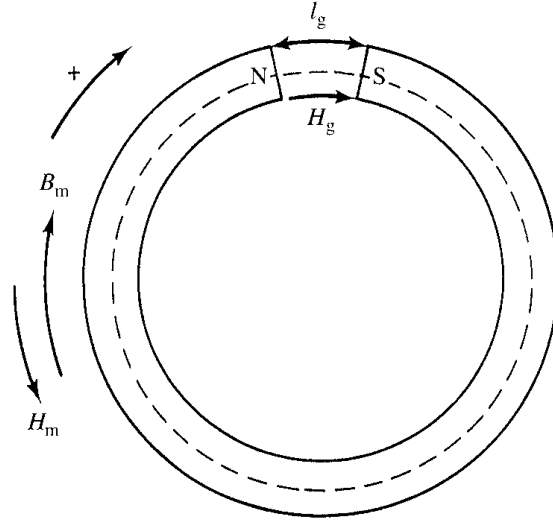
Figure 2-3 Example of an open magnetic ring with a gap of length l_g. Adapted from [66].

The job of the magnet designer is to determine the geometry of the magnet such that the operating point P is at the appropriate position along the demagnetization curve as shown in Figure 2-4. This is largely determined by the demagnetizing factor of the magnet, which can be altered based on the shape of the magnet. The slope of the line connecting line OC is determined by the demagnetizing factor N_d where the demagnetizing field H_d is proportional to the magnetization such that $H_d = -N_d M$. The importance of the demagnetizing factor for thin film samples will be discussed later in Section 2.4.3.

To determine the best operating point let's consider the magnetic fields present in the air gap of the ring and in the magnet itself. Given Ampere's law which says that the line integral of H around the circuit equals the electromotive force, we can say that since we have a permanent magnet ring and no current, we find the line integral must be zero:

$$\oint H dl = 0, \qquad \text{therefore} \qquad H_g l_g - H_m l_m = 0. \tag{6}$$

Since the magnetic flux of such a magnetic circuit is $\Phi = BA$ where A is the cross sectional area of the ring, and $B = H$ in the air gap we can also say

$$H_g A_g = B_m A_m. \tag{7}$$

By assuming the cross sections, A of the air gap and the magnet are the same, we can solve for the field in the gap, H_g for equations (6) and (7) and multiply the result finding that

$$H_g^2 V_g = (B_m H_m) V_m, \tag{8}$$

where $V_m = A_m l_m$ stands for volume of the magnet. This shows that V_m can be minimized when the product BH is a maximum. This is of principle interest for the engineer who can then make the best use of magnetic material in the circuit by maximizing the product BH for the particular application.
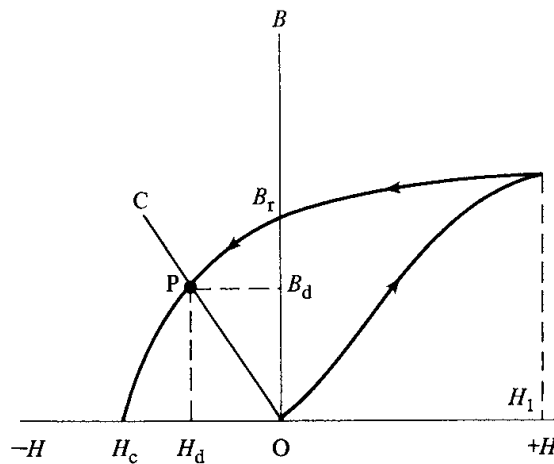
Figure 2-4 Virgin magnetization and demagnetization curve where B_r is the remanent induction. Adapted from [66].

Referring again to Table 1 we note that the units of the energy product is in MGOe (cgs), pronounced mega-gauss-oersted. Considering the product of the flux B in gauss and the field H in oersted, the units are consistent with the product BH. In consequence, $(BH)_{max}$ can also be thought of as the largest rectangular area under the demagnetization curve where one vertex lies on the demagnetizing curve and the other at the origin of the B and H axes.

2.4 Introduction to Magnetic Anisotropy

Before reviewing types of switching mechanisms one more important quantity for magnetism must be introduced which is largely responsible for the coercive field, which is the magnetic anisotropy. The magnetic anisotropy is simply the angular dependence of magnetic properties. We first consider the simplest case of a uniaxial anisotropy, which can have multiple origins including crystalline (magnetocrystalline) or shape anisotropy. Another type of anisotropy called stress anisotropy is possible which is considered in Part II, Section 4.4. The uniaxial anisotropy in general is such that the easy axis, or the most energetically favorable direction for the magnetic moments to point, lies along a line. The anisotropy energy is given by the anisotropy constant K, which is an energy density. Crystal anisotropy from the highly anisotropic f-orbitals of the rare-earth elements is considered to be the origin of the amazing coercive fields found in these compounds and so the careful determination of K and its origin is important to this dissertation. Shape anisotropy is thought to be the origin of the coercive field in the only competitive alternative to rare-earth permanent magnets called Alnico, which is discussed in Section 2.4.3.

2.4.1 Uniaxial Anisotropy: Simplest Case

In cgs units, the angular dependent energy for such a uniaxial anisotropy can be written as

$$E_u = K_u sin^2\theta, \tag{9}$$

where the angle between the magnetic moment and the preferred easy axis direction is θ and K_u is the uniaxial anisotropy constant. An additional energy term comes from applying an opposing magnetic field H written as

$$E_f = -M_s H \, cos\theta. \tag{10}$$

Now taking the sum of these two energies we find

$$E_u + E_f = K_u sin^2\theta - M_s H \, cos\theta. \tag{11}$$

To determine the stable positions of this angular dependent energy function we take the second derivative, set the function to zero, and solve for H where

$$\frac{d^2E}{d\theta^2} = 2K \, cos\theta - M_s H \, cos\theta = 0. \tag{12}$$

For $\theta = 0$, the field is aligned along the easy axis so we can solve for the field necessary to switch the direction of magnetization, called the anisotropy field:

$$H_K = \frac{2K}{M_s}. \tag{13}$$

This anisotropy field, which can be associated with the other types of magnetic anisotropies mentioned, is often equated with the coercive field H_c. This is the origin of the conception that a large anisotropy constant K will thereby provide a large coercive field. Hence, many studies are dedicated to finding ways to enhance the anisotropy constant.

2.4.2 Crystalline Anisotropy

Formerly known as magnetocrystalline anisotropy, this anisotropy originates from spin-orbit coupling. To understand this, let's review other interactions among the electron spin, orbit, and crystal lattice. We can consider the exchange interaction of neighboring spins as a spin-spin coupling. The exchange interaction is such that neighboring spins strongly prefer to point parallel or antiparallel to each other. However, the exchange interaction is isotropic and so cannot contribute to crystal anisotropy. The orbit-lattice coupling is strong and shares the symmetry of the crystal. While the orbits of a single atom may be circular, when they form part of a cubic crystal, the electric fields that join the atoms elongate the orbitals along the cubic axes of the crystal so the orbits are strongly coupled, or bound by the crystal lattice. Finally, we consider the spin-orbit coupling where an external field will try to reorient the spin of an electron and also its orbit. Since the orbit is strongly coupled to the lattice, it will resist reorientation, but the spin is also coupled to the orbit, thus sharing the crystal symmetry and will also resist the attempt to rotate the spin axis. The anisotropy energy required to rotate the spin system away from the easy axis is relatively small and thus the spin-orbit coupling is relatively weak. It only take a few hundred oersteds to rotate the spins from the easy axis. We can also consider the lattice of atomic nuclei and its coupling to electron spin is also weak. These relationships are summarized in Figure 2-5.
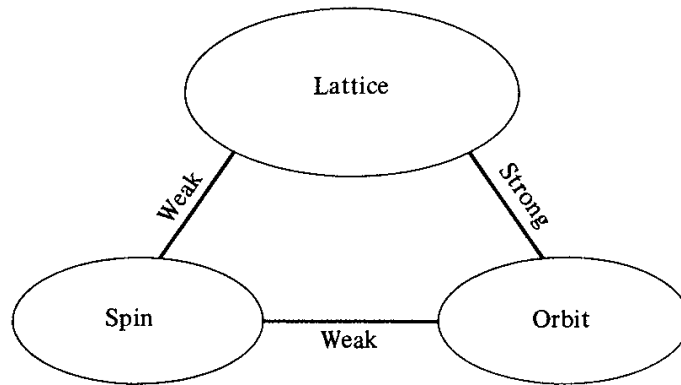
Figure 2-5 Interactions between the crystal lattice, electron spin, and orbitals. Figure from [66].

Now we explain the crystal anisotropy directions in cubic and hexagonal crystals to get a better practical understanding of crystal anisotropy. Starting with the cubic system, imagine taking a single-crystal iron piece and cutting a disk parallel to the {110} plane. As show in Figure 2-6, different crystallographic directions traverse the diameter of the disk at different angles. The measurements of magnetization along these diameters in the plane of the disk give the crystal anisotropy information about these directions. One can see the corresponding crystallographic directions in the inset at the top of Figure 2-6. We learn from this information that the easy axis of Fe is along the $\langle 100 \rangle$ direction while the hard direction is $\langle 111 \rangle$, and $\langle 110 \rangle$ is somewhere in between.

We can now use the area method to find the crystal anisotropy energy from the magnetization curves in the top of Figure 2-6. The work done in magnetizing to saturation is simply the area between the curve and the M-axis. We also need to remember that the formulation of the crystal anisotropy energy is taken as a series expansion of the direction cosines of M_S relative to the crystal axes. This formulation

57

results in the energy of the first anisotropy constant to be $K_1/4$ [66]. This gives the

energy to magnetize the crystal in the $\langle 110 \rangle$ noneasy direction. Knowing this and the

fact that we need to divide the induction (B) in the top of Figure 2-6 by 4π to get the

magnetization in emu/cm^3 we can then use the area method to calculate the

anisotropy constant. As example, we can roughly calculate the first anisotropy

constant K_1 for Fe by taking the area between the easy axis curve for $\langle 100 \rangle$ and the

noneasy direction $\langle 110 \rangle$. Taking the area simply as a right triangle we can multiply

the difference in remanent magnetizations and the saturation fields and divide by two.

This gives the work done as $\left(\frac{20,000 - 14,000\ G}{4\pi} \times 275\ \text{Oe} \right)/2 = 65,700\ \text{erg/cm}^3$. Now we

equate the work done with the anisotropy constant as $K_1 = 4W$ and find that for Fe,

$K_1 = 2.6 \times 10^5$ erg/cm^3. For this rough estimate, it agrees well with the integration

giving 2.72×10^5 erg/cm^3 [66].

For comparison we present the crystalline anisotropy values for the most

powerful known permanent magnet which is $Nd_2Fe_{14}B$ as 3.7×10^7 erg/cm^3 [68]. This

greater than two orders of magnitude increase is supposedly from hybridization of Fe

atoms with the Nd atoms which have strong spin-orbit coupling from their 4-f orbitals

[69], [70].

2.4.3 Shape Anisotropy

The second type of magnetic anisotropy explains how the shape of a magnet

influences its magnetic properties. This effect is particularly important in thin films,

where the shape of the magnet is essentially an infinite plane, and for permanent

magnets, where long and thin magnetic shapes can drastically enhance permanent

magnetic properties along that direction. The effect comes from the fact that a bar

magnet with poles at each end creates magnetic field lines radiating from the north pole to the south pole both inside and outside the magnet as shown in Figure 2-7(a). This internal magnetic field tends to demagnetize the magnet and is thus called the demagnetizing field, self-energy, or magnetostatic energy. Remember that the diagram is for a bar magnet without any external field, so the only field is created from the magnetization itself. Figure 2-7(b) shows that the B field lines inside the magnet are directed oppositely to the lines in (a).
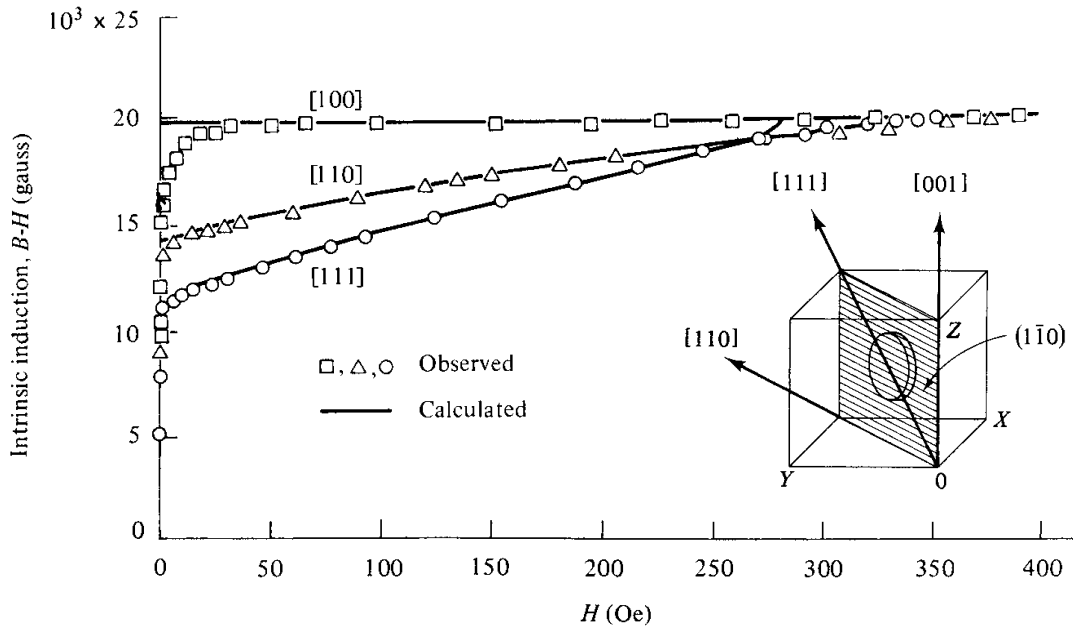
Figure 2-6 Calculated and measured magnetization curves for Fe-Si crystals. Inset shows the disk cut along the (110) plane and the respective crystallographic axis with respect to the disk. Figures adapted from [66].

To quantify this demagnetizing field we approximate its energy as

$$E_{\mathrm{ms}} = \frac{1}{2} H_{\mathrm{d}} \cdot M.$$

$$(14)$$

59

The demagnetizing field is $H_d = N_d M$ where N_d is the demagnetizing factor discussed next. The demagnetizing factor can only be calculated exactly for elliptical shapes, for example the prolate spheroid (cigar shape), which is often approximated as a cylinder. An example of the prolate spheroid is in in Figure 2-8.

The demagnetizing field energy in terms of N_d is

$$E_{ms} = \frac{1}{2} N_d M^2.$$
(15)

Considering the prolate spheroid in Figure 2-8, we can arrive at an equation for the angular dependent energy, reminiscent of the uniaxial anisotropy where:

$$E_{ms} = \frac{1}{2} [(M cos\ \theta)^2\ N_c + (M sin\ \theta)^2\ N_a]$$
(16)

Where the shape anisotropy constant is given as

$$K_s = \frac{1}{2} (N_a - N_c) M^2\ \frac{erg}{cm^3} (cgs).$$
(17)

The magnetization M is at an angle θ to the semi-major axis c, of the prolate spheroid. N_c and N_a are demagnetizing coefficients along the c and a axes, respectively. From Cullity [66], The demagnetizing factors for various geometrical cases are approximated below where the ratio of the two axes is taken as $c/a = m$.

$$\text{(long, thin rod)}\ N_c \approx \frac{C_3}{m^2} (\ln(2m) - 1)$$
(18)

$$N_a = N_b \approx \frac{C_3}{2}$$
(19)

$$\text{(oblate spheroidm, disk)}\ N_c = N_b \approx C_3 \left(\frac{\pi}{4m} - \frac{1}{2m^2} \right)$$
(20)

$$N_a \approx C_3 \left(1 - \frac{\pi}{2m} + \frac{1}{m^2} \right).$$
(21)

The value $C_3 = 4\pi$ (cgs) and $C_3 = 1$ (SI).
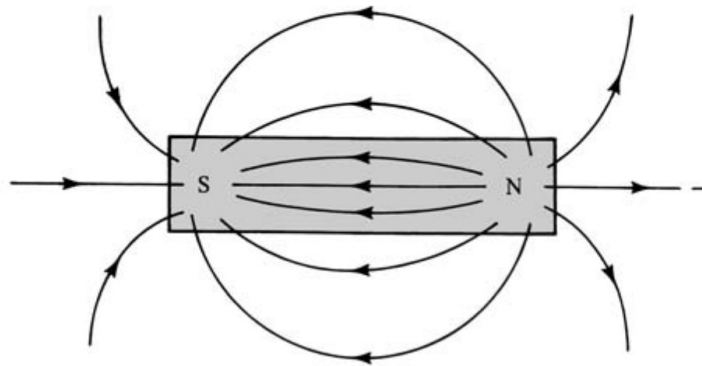
(a)
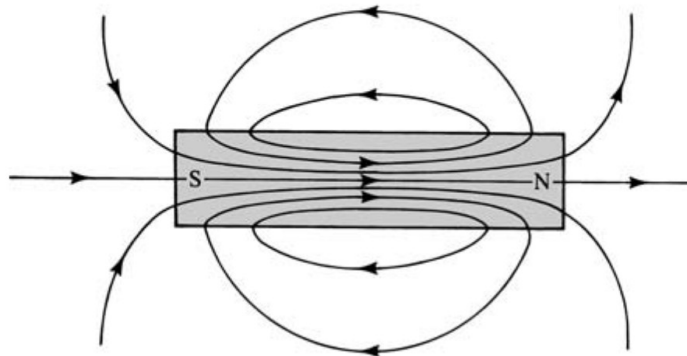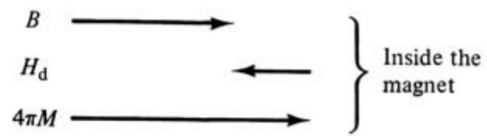
(b)

Figure 2-7 Fields of a bar magnet in zero applied field. (a) *H* field, and (b) *B* field. The vectors in the center indicate the values and directions of *B*, H_d, and $4\pi M$ (cgs units) at the center of the magnet. Figure from [66].
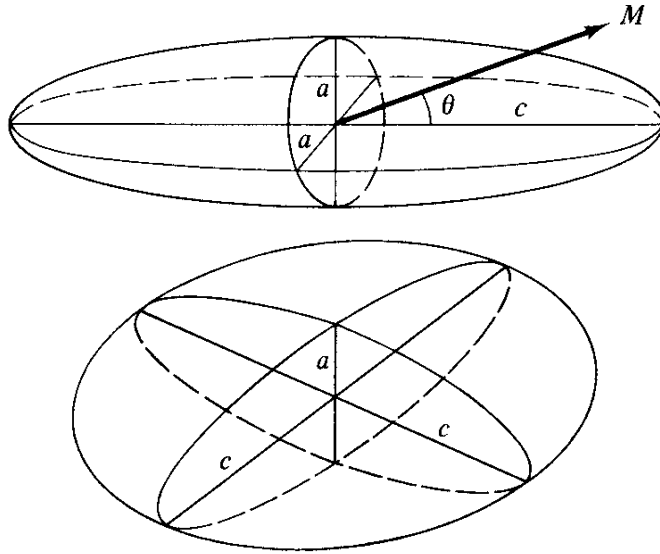
Figure 2-8 Example of a prolate spheroid (above) and an oblate spheroid (below). Figure adapted from [66].

For the case of the infinite plane (thin film geometry), we can approximate this as the oblate spheroid with large m=c/a ratio. Equation (20) gives the in-plane demagnetization factor $N_c = 0$ for large m, such that the demagnetizing field in the film plane equals zero. For the out-of-plane case with large m, equation (21) gives a demagnetizing factor of $N_a = 4\pi$. Thus, the out-of-plane demagnetizing field $H_d = N_a$ M $= 4\pi M$. We find that the out-of-plane demagnetizing field scales with the magnetization. This example in demagnetizing factors indicates that thin films prefer magnetic moments oriented in-plane because the large out-of-plane demagnetizing field will oppose any moments pointing perpendicular to the plane.

The example of a permanent magnet using shape anisotropy is alnico. Alnico is considered a spinodal alloy of Al, Ni, Co and Fe, and was a contemporary competitor of vicalloy. The microstructure of alnico is shown in Figure X where the long and fine Fe-Co particles deliver an $h_c = 1000\ G\ +$. Alnico remains a competitive bulk

permanent magnet but its market share continues to be eroded by rare-earth permanent magnets. Significant improvements on Alnico since the times 1950's have been increasing the energy product for Alinco V at 5 MGOe to Alnico 7 and 9 reaching 10 MGOe [71].
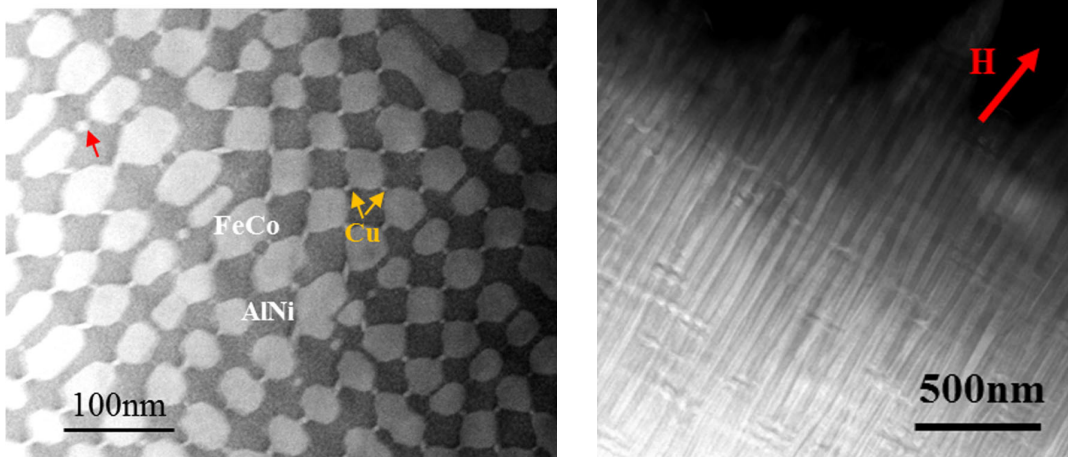
Figure 2-9 (left) High-angle annular dark field (HAADF) scanning tunneling electron microscopy (STEM) images showing the cross section of long particles in an alnico 8 sample. (right) Image showing the length of grains and the applied field direction (H) during annealing is indicated in red. Figure adapted from [71].

2.5 Switching and Pinning Mechanisms

A number of models have been developed to describe the behavior of magnetic materials with a variety of microstructures and switching mechanisms. We can learn about the type of mechanisms responsible based on the shape of the hysteresis loops and their angular dependence, which are easily measured in the lab using VSM. This effort aligns with the idea that improving understanding of known materials, for example Fe-Co-V alloys, will contribute to the search for new rare-earth free permanent magnets.

2.5.1 Stoner-Wohlfarth Switching

In the 1940's, Stoner and Wohlfarth proposed a model to describe the behavior of how a collection of aligned single-domain particles with some anisotropy rotate under an external magnetic field [60]. The model's success lied in its ability to describe the properties of particulate permanent magnets of the time and continues to be a robust model, sometimes combined with other models to describe a number of cases with easy axis aligned particles that are interacting or non-interacting [72].

For brevity, we will not derive the result from the beginning but simply describe the basic assumptions for the model as done by Cullity [66]. For particles of uniaxial anisotropy as defined in the previous section, consider a magnetic field H applied at an angle α with the easy axis as shown in Figure 2-10. The angle θ is the angle of the saturation magnetization of the single domain particle. In this case, the particle derives its anisotropy energy from shape anisotropy so the diagram shows an ellipse, which is the cross-section of a prolate spheroid.
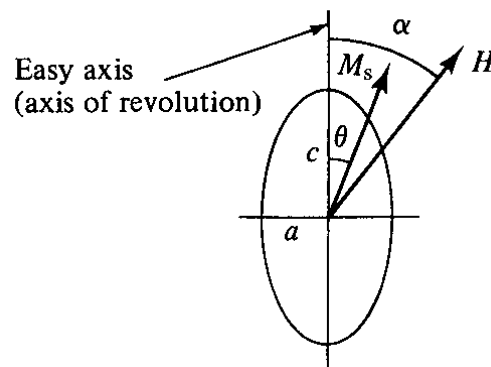
Figure 2-10 Coordinates with respect to the easy axis of a single-domain ellipsoid.

By solving for the equilibrium position as in the previous section using only the first derivative of the energy relation, the component of the magnetization in the field direction can be derived. Solving for the case of α is 90°, it's found that the magnetization along the field direction is a linear function of H with no hysteresis as shown in Figure 2-11:

$$\frac{M}{M_s} = H \frac{M_s}{2K_u}.$$ (22)

Saturation magnetization is reached when the field equals the anisotropy field value $H = H_K = 2K/M_s$. When the field is along the easy axis, a critical value is needed to account for the unstable equilibrium during 180° switching. Thereby the equation describing the switching field h_c, defined as the field at which the largest change in magnetization occurs, and the equation for the critical angle θ_c is given below:

$$tan^3\theta_c = -tan\,\alpha,$$ (23)

$$h_c^2 = 1 - \frac{3}{4}sin^2 2\theta_c.$$ (24)

This result is of practical interest because the equation shows a symmetric switching field about the applied field range from 0° to 90°. This can be easily seen in an angular dependent switching field measurement where magnetic hysteresis loops are measured at a number of angles within this range described in Section 3.3. Also of interest is the intrinsic coercive field h_{ci}, where magnetization is reduced to zero. Figure 2-11 shows the hysteresis loops derived from the above formalism and it is clear that h_{ci} steadily drops as the angle α increases. When the field is applied perpendicular to the easy axis (α is 90°) there is no coercive field.

The Stoner-Wohlfarth switching mechanism for single domain particles will now be compared to the starkly different case of the angular dependence of switching fields for 180° domain walls.
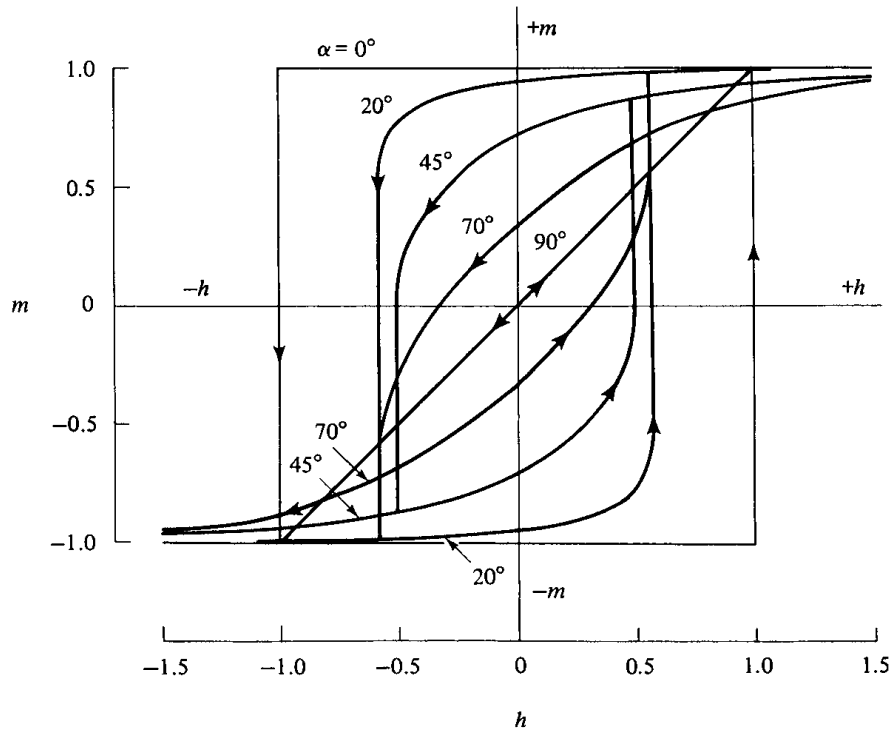
Figure 2-11 Magnetic hysteresis loops following the Stoner-Wohlfarth model of switching for single domain particles with uniaxial anisotropy; α is the angle between the field and the easy axis. Figure and caption adapted from [66].

2.5.2 Kondorsky Switching and Comparison to Stoner-Wholfarth Model

In 1940, Kondorsky derived a function describing the angular dependence of the switching field for a pinned domain wall of a magnetically uniaxial crystal [61], [73]. Domain wall pinning is associated with variations in the domain wall energy (ε_w) landscape for a domain wall traveling along direction s, through a magnetic

material [74] as depicted in Figure 2-12. The domain wall is simply the separation between two volumes of magnetization pointing in different directions.
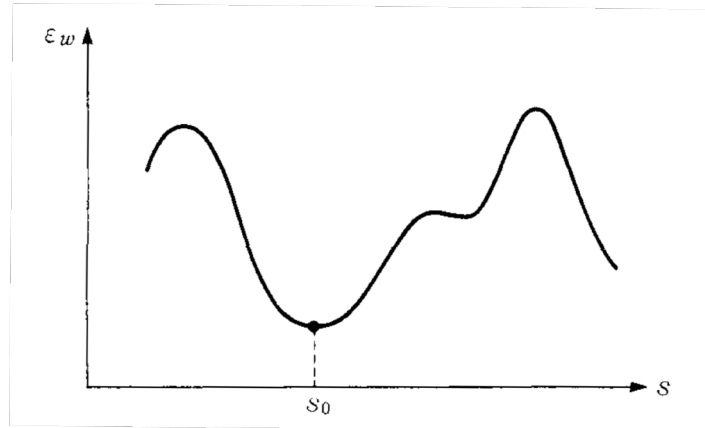
Figure 2-12 Schematic showing the variation of domain wall energy ε_w, with position s. Figure from [74].

In this case, we deal with 180° domain walls which separate magnetic volumes that point oppositely from one another depicted in the bottom of Figure 2-13. 180° domain walls form in a magnetically uniaxial crystal meaning that the magnetization prefers to point parallel, or antiparallel to a single direction. We consider a 180° domain wall with the applied field H pointing at an angle of φ_h with respect to the easy axis. From the component of the external magnetic field that points along the easy axis being $H \cos \varphi_h$, it's apparent that a large angle φ_h means less field will be applied to move the magnetic domain wall.
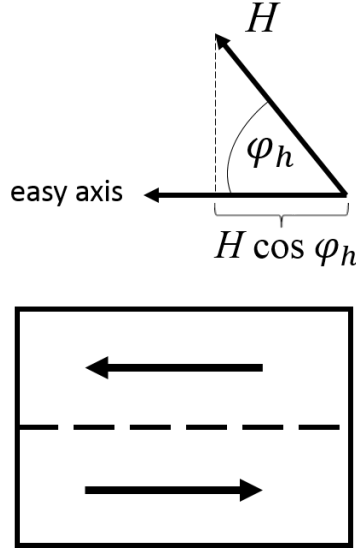
Figure 2-13 Coordinates for the Kondorsky function relation where φ_h is the angle of the magnetic field with respect to the easy axis.

To move the domain wall amount ds, the wall requires a change of field energy dE_H such that:

$$dE_H = 2S\mu_0 M_s H \cos \varphi_h \, ds, \tag{25}$$

where S is the surface area of the domain wall. The pinned domain wall can only be detached if the change of the field energy dE_H is greater than or equal to the change of the domain wall energy $d\varepsilon_w$. Referring to Figure 2-12, the change of domain wall energy will only move as far up the slope $\frac{d\varepsilon_w}{ds}$, as the field energy will push it. Equating these two energies together we find:

$$H_{sw}(\varphi_h) = \frac{1}{2\mu_0 M_s H \cos \varphi_h} \frac{d\varepsilon_w}{ds}. \tag{26}$$

$H_{sw}(\varphi_h)$ is the angular dependence of the switching field. If we plot the inverse of the switching field with $\cos \varphi_h$ it forms a straight line. This is a quick way to check if the sample follows Kondorsky's function for a pinning type domain wall motion.

An experimental example is shown next where actual hysteresis loops for different angles are presented. The switching field is labeled for clarity on Figure 2-14(c) & (d). The switching field dependence of the hysteresis loops shown here agrees very closely with the Kondorsky model.
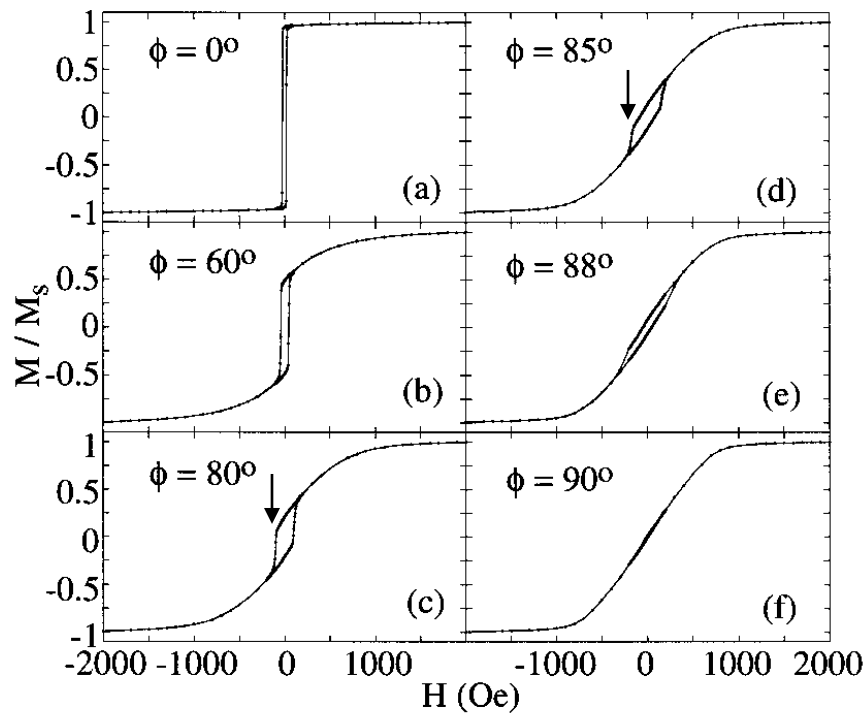
Figure 2-14 Hysteresis loops of 500 nm thick single-crystal CrO_2 films with magnetic field applied at different angles from the easy axis direction. Figure adapted from [75].

From our brief introduction to the two main types of switching mechanisms, we see that the angular dependent switching field is a powerful way to understand the type of switching mechanism present in a magnetic sample. We can compare the switching fields between Stoner-Wohlfarth model and the Kondorsky model to easily distinguish between the two as in Figure 2-15.
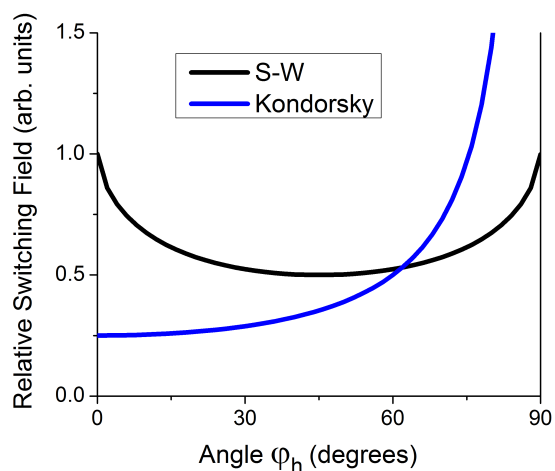
Figure 2-15 Relative switching field as a function of angle between the applied field and the easy axis for Stoner-Wohlfarth (S-W) and Kondorsky models of switching.

Although these models were developed for bulk samples with easy axis aligned particles, there are special cases where they do apply for thin films. For example, for a polycrystalline film with in-plane easy axis, the Kondorsky model can be applied to out-of-plane angles as done with a number of thin film systems [76], [77]. This is the justification for using this model to apply to our Fe-Co-V films studied in this dissertation.

2.6 Theory of Fe-X and Co-X alloys

One motivation for studying Fe-Co-X alloys where X = V, W, Ta, Zr, Mo, Hf, and Nb, are predictions and observations that X elements with large spin-orbit coupling can hybridize with Fe and Co and affect the crystalline anisotropy constant so important in permanent magnets. Hybridization is how the bonds between atoms effect the electron orbitals and therefore their spin density, charge density, and spin-orbital coupling. In this section we present studies on Fe-W [3], [78], Co-W [79],

70

[80], and Fe-V [81] that show tungsten, vanadium, and related 3d and 5d refractory metal substitutions in iron and cobalt have effects on the spin and charge density of iron or cobalt, which can affect the crystalline anisotropy constant so important in permanent magnets. A particular motivation for the present work is the prediction that using thin films may stabilize as yet unobserved phases which hold promising magnetic properties [79].

One study using Mössbauer spectroscopy finds that vanadium atoms substituted in Fe up to 18 at% reveals changes in the spin and charge densities [81]. However, the technique does not allow the distinction between the changes of s-electrons largely responsible for conduction, and the d-like electrons that are responsible for magnetism. Dubiel and Zinn suggest the change in density of 3d-like electrons is the more likely case because of related electronic structure calculations [82]. Dubiel and Zinn admit that an equally likely scenario that describes their data is the difference of the atomic volumes between the host and impurity atoms. However, preliminary work done with XMCD not discussed here does indicate V's strong influence on the 3d magnetic electrons of Fe.

Of related interest is the behavior of other refractory transitions metals like W when alloyed with Fe and Co. Kikuchi et al. calculated the changes in anisotropy constants for Co-W alloys [80] finding an increase in anisotropy constant K_1 and a suppression of K_2. Another investigation of first-principles of Fe-W and Co-W alloys found that anisotropy constants are sensitive to crystal structure and showed new crystal structures not observed in the system are candidate permanent magnets [79]. The authors cited recent improvement in experimental nanotechnology gives access

to the crystal structures not previously considered in the past [79]. In particular, thin film techniques are known to lead to metastable crystal structures giving yet another motivation for the current thin film investigation of these Fe-Co alloys with refractory transition metals.

2.7 Permanent magnetism in Fe-Co-V alloys

Here we discuss the history of the Fe-Co-V alloys focusing on the hard magnetic phases called Vicalloys. Small additions of vanadium up to 2 at% in Fe-Co alloys are known to result in soft magnets called Permendur which preserve the high flux and permeability of the pure Fe-Co alloy while making it less brittle so the alloy is capable to be machined for applications [83], [84]. The present work focuses on the Fe-Co-V alloy of higher vanadium content ranging from 9.5 at% to 13 at% called Vicalloy. The V is for vanadium, I for iron and C for cobalt, making the name Vicalloy. Nesbitt discovered and held the patent for Vicalloy in the 1940's and noted it as a "workable alloy for permanent magnets" [85]. This was because the combination of its easy machinability and reasonable coercive field of $h_c = 300\,G$, made it applicable in early sound recording tapes [85] and is still used today in modern hysteresis motors [5], [6]. In comparison, Alnico had considerable processing requirements of a heat treatment with applied magnetic field [71], was difficult to work with because of brittleness [86], and had an $h_c = 500\,G$ at the time of Vicalloy.

Different types of Vicalloy have been developed which have different annealing and cold-working processes. Vicalloy I has an optimal composition of $Fe_{38.5}Co_{52}V_{9.5}$ where the alloy can be machined as cast, then a heat treatment of 600

°C for 2 hours gives an energy product of 1 MGOe. Another variation, called Vicalloy II, requires significant cold working and can achieve an energy product of 2.0 to 3.5 MGOe. These higher energy products are achieved after an area reduction of 75 to 95 percent during cold working before the final heat treatment. The cold working hardens the material considerably so this can only be accomplished in fine wires. The compositions Nesbitt has studied are displayed in Figure 2-16. It's clear from the above discussions that the combinatorial method offers the ability to more systematically study a composition space than in the past.
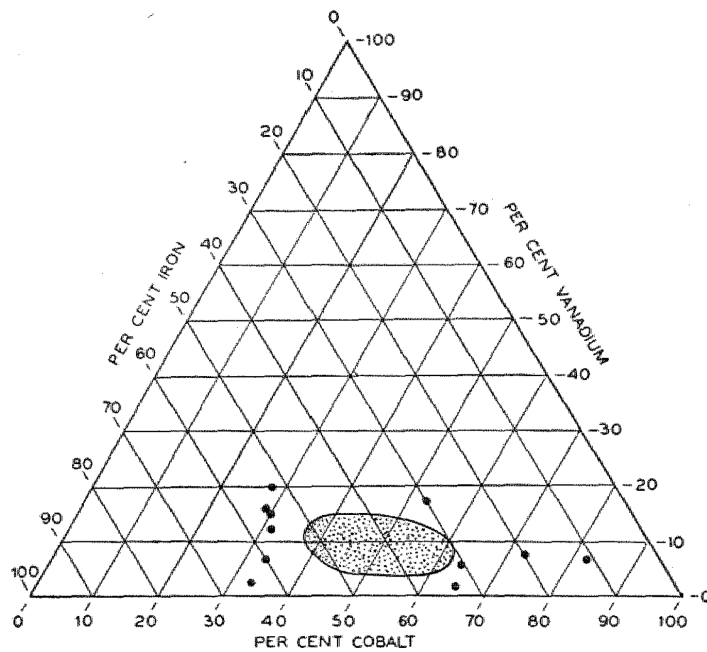
Figure 2-16 Fe-Co-V compositions tested in Nesbitt's seminal work where the shaded region shows the area extensively explored. Adapted from Nesbitt [85].

Although Sourmail cites in 2005 the considerable confusion over the Fe-Co-V phase diagram [7] we defer to the earlier work of Nesbitt who patented Vicalloy and most certainly had the best working knowledge of the system. Vicalloy is considered

special among the precipitation-hardened or fine-particle permanent magnets of its time because of its phase diagram. A number of other precipitation-hardened alloys such as Fe-Co-Mo, have a two-phase region stable at room temperature. A typical precipitation hardened magnet is quenched from a temperature above the solubility curve AC, as shown in Figure 2-17, thus freezing in the high temperature phase. The alloy is then raised to an intermediate temperature below the solubility curve to precipitate a small quantity of the low temperature gamma phase that imparts the good permanent magnetic properties. The alloys then contain a small amount of low temperature phase dispersed in a matrix of the high temperature phase. Previous work revealed the composition of the gamma phase [87], [88] to be approximately $Fe_{15}Co_{64}V_{21}$ which agrees with the proposed vanadium rich $(Fe\text{-}Co)_3V$ phase with $L1_2$ structure proposed by Ashby [89].
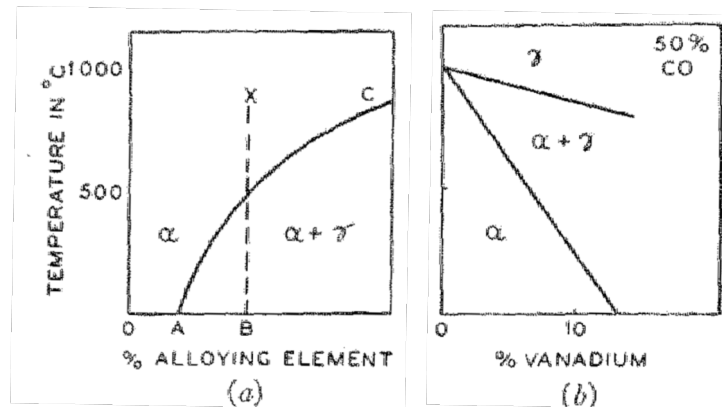
Figure 2-17 Comparing typical phase diagram of (a) dispersion hardened permanent magnet alloys to (b) Vicalloy. Adapted from Nesbitt [85].

74

According to the phase diagram of Martin and Geisler in Figure 2-19, room temperature Vicalloy at 9.5 at% V consists entirely of the low temperature phase as verified by X-ray and recently reported for similar compositions [5], [7]. This pure alpha phase does not have good permanent magnetic properties though. For optimal permanent magnetic properties, the alloy is first quenched or slow cooled from high temperatures of 1000°C. Then, the temperature is raised to the two-phase region at around 600°C which precipitates some of the high temperature gamma phase to disperse in the low-temperature phase matrix. In this sense, it is the opposite of other precipitation hardened alloys and explains some of the cold-working phenomenon.

It has been observed that cold-working of higher vanadium content Vicalloys above 10 at% V contain the second phase upon cooling. In general, cold working reduces the phase content to that chiefly of the low temperature phase. Cold working is also known to cause grain alignment thereby improving the permanent magnetic properties [90], [91].

Two ongoing debates about Vicalloy remain in the literature including (1) the precise origin of magnetic hardness [5], [90], [92], [93], and (2) the precise nature of the low-temperature two-phase region with higher vanadium contents near 10 at% V [7], [92], [94], [95]. Oron presents electron micrographs in Figure 2-18(a) of Vicalloy I, which show the precipitate phase has uniformly dispersed 50 nm particles with no indication for any shape anisotropy [90]. The micrograph of Vicalloy II in Figure 2-18(b) does indicate some evidence to support shape anisotropy. We are concerned with Vicalloy I results since our thin film samples were simply annealed and not cold worked like Vicaloy II. The possibility of strain induced uniaxial anisotropy had to be

abandoned after careful X-ray measurements showed gamma precipitate formation did not cause residual strains in Vicalloy [90]. Crystalline anisotropy still remains a possibility as the origin of magnetic hardness. The hard axis of cold-rolled samples changed from in-plane to out-of-plane direction after heat treatment, which was correlated with the recrystallization of alpha grains to the <111> axis using electron diffraction [90]. Finally, only recently has a pinning type mechanism been considered in Vicalloy I, but no quantitative evidence was given to support the claim [5]. The investigation by Zakharov et al. proposed that the gamma phase was not responsible for the magnetic hardness [5]. The authors showed this by using a commercial alloy of 7 at% V where the gamma phase precipitation is at a separate temperature than the atomic ordering of the Fe-Co phase. They used high temperature dilatometry and magnetometry to convince the reader of the separation of these two events but unexpectedly low coercive fields of 116 G (9.2 kA/m) are found. They explained that the proposed ordered B2 structure retains the lattice structure of the disordered structure and so the large expected pinning at antiphase domain boundaries was admittedly absent. The antiphase boundaries described qualify as a pinning site because if the crystalline anisotropy K, is closely related to the ordering of the alloy η, such that $K(\eta)$, then at the boundary there is a steep dependence of $K(\eta)$ causing a strong pinning site. From this review it seems only crystalline anisotropy or pinning of the domain walls are probable origins of magnetic hardness in Vicalloy I.

76
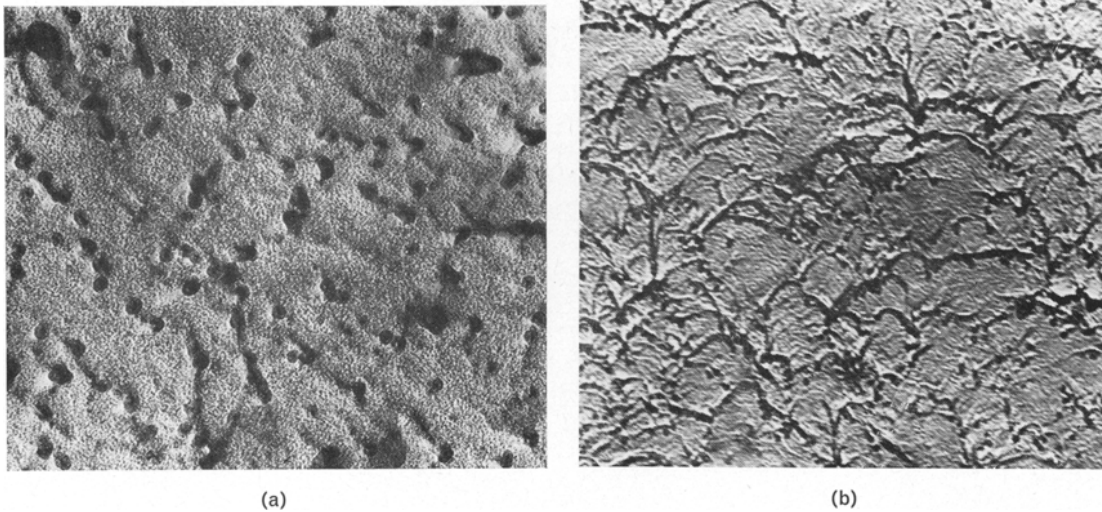
Figure 2-18 Electron micrographs of (a) Vicalloy I and (b) Vicalloy II, both at ×30,0000. Image widths are then about 3 μm. Figure from [90].

Concerning the second debate about the low-temperature two-phase region we present the incomplete state of published phase diagrams and some possible explanation. Josso [92] suggested a more careful study of the Fe-Co-V phase diagram in Figure 2-19 and admitted that for practical purposes, the metastable equilibria are of greater significance. It's known that vanadium tends to slow the ordering of the alpha Fe-Co body-centered cubic phase (α-bcc) and thus maintain soft magnetic properties while retaining higher electrical resistivity to reduce eddy currents [92], [95]. It's apparent that interesting properties arise from metastable phases in Fe-Co-V, which certainly motivates further study such as the current thin film study. The disagreement of the higher vanadium two-phase region is most clearly seen by comparing phase diagrams in Figure 2-19 with Figure 2-20. Bennett and Pinel suggest that the extreme sensitivity of the phases to annealing can explain the difficulty in resolving this equilibrium phase diagram. We offer that cold-working
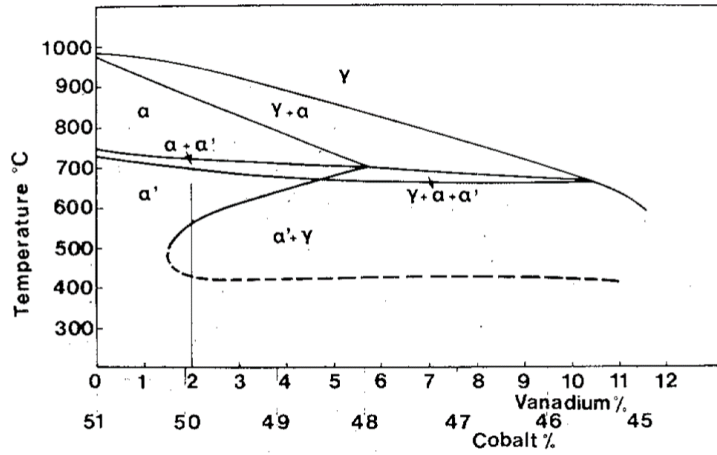
Figure 2-19 Oblique section through the Fe-Co-V phase diagram after Martin and Geisler. Figure from [92].
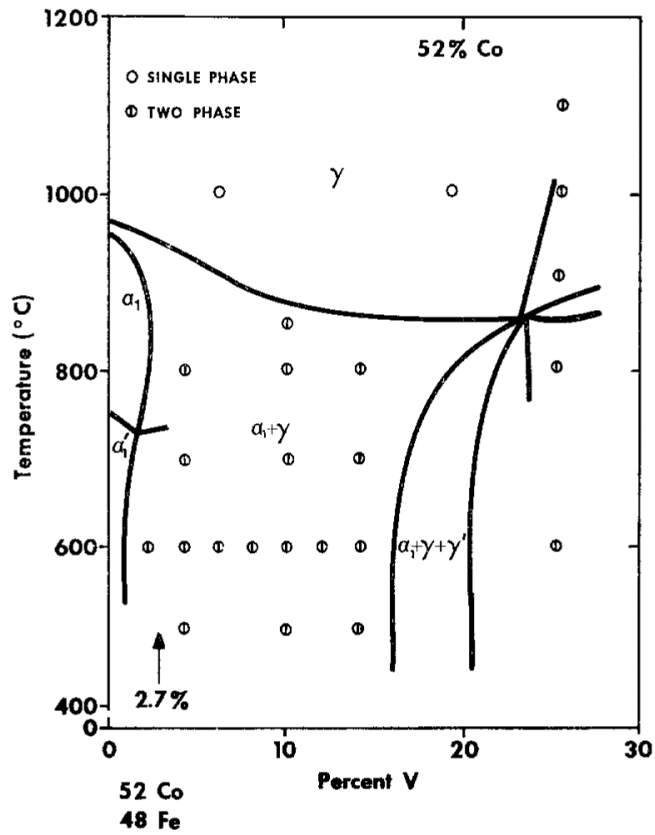
Figure 2-20 Isopleth through the Fe-Co-V ternary phase diagram from [94].

appears to accelerate the transformation of the gamma phase to the alpha phase as noticed by Oron [90].

Considering Fe-Co-V in the context of the other Fe-Co-X alloys we have studied we see that it is unique. The Fe-Co-W system described earlier appears to have an increased out-of-plane anisotropy from a platelet microstructure [59]. In the Fe-Co-Mo system the magnetic hardness seemed to originate from a slight tetragonal distortion in the unit cell [24].

Chapter 3. Combinatorial Investigation of Fe-Co-V system

The exploration of the Fe-Co-V ternary is in the interest of finding rare-earth free permanent magnet alternatives. Towards this goal the present study seeks to:

(1) Improve the understanding of existing systems,

(2) Explore for metastable phases of known compositions found in thin films,

(3) And search for overlooked structure or property features in the composition space.

We used the combinatorial thin film method to systematically explore the Fe-Co-V composition space for permanent magnets. In the following chapter we present the results of the combinatorial thin film libraries and compare our Fe-Co-V thin film samples to known bulk compositions and properties of vicalloy, a known permanent magnetic composition range in the system. In addition, the magnetization reversal mechanism, or switching mechanism of Vicalloy is rarely mentioned in the literature. We present switching field dependence of our Vicalloy thin film samples to gain insight into the precise switching mechanism.

We mention now that all the data and phase diagrams presented in our work from thin film samples. It is known that there are large differences between bulk and thin film properties of magnetic materials because of increasing surface area to volume ratio and associated increase of surface energy of thin films [96]. Despite this, thicknesses above about 100 nm are known to elastically relax from the substrate and therefore approach their bulk properties rapidly [97]. In addition, we conducted a thickness dependence study of the $Fe_{70}Co_{30}$-V thin films in order to account for the property and crystal structure dependence of the thickness. This not only helps us

confirm we are operating in the "bulk regime" where the crystal structure and properties agree with the bulk, but helps us find that transition accurately. In an effort to produce bulk-like properties we designed the combinatorial search of the Fe-Co-V system using film thicknesses approaching 500 nm, well above the 100 nm thickness known for displaying non-bulk properties [97].

3.1 Fabrication of Fe-Co-V Thin Film Libraries

A number of Fe-Co-V composition spreads were deposited using three elemental targets in the ultra-high-vacuum magnetron co-sputtering geometry described in Chapter 1. DC sputtering was used for this experiment. Some wafers were fabricated at Ruhr University in Bochum, Germany where a 4-inch Si wafer with a 5-gun sputtering chamber was used as shown in Figure 3-1. The Bochum sputter guns were 2-inches in diameter. Base pressures of both chambers were below 5×10^{-8} Torr. Sample to target distances during deposition was 10 cm. Sputtering pressures were 5 mTorr of ultra-high-purity argon gas.

For all wafers in this study the films were deposited for 45 minutes at room temperature followed by a post-anneal between 600-700 °C for 1 hr. The substrates were then allowed to cool down to room temperature on the substrate heater naturally. Typical gun powers were between 15-70 Watts for Maryland and 30-100 Watts for Bochum. Ternary composition spread films averaged 350 nm ranging from $250 - 450$ nm, while natural thickness spread films ranged from $500 - 50$ nm. Film thickness was measured with profilometer shown in Figure 3-20. The composition at each sample pad across the wafer was determined by WDS. Sputtering targets of Fe, Co, and V of at least three 9's was used (99.9% pure).

Natural composition/thickness spread films of $Fe_{70}Co_{30}$ -V alloy system were fabricated using an alloy target of $Fe_{70}Co_{30}$ and an elemental target of V. The films were co-sputtered onto 3 inch Si wafers with (100) oriented, Boron (p-type) doping with a 500 nm thick thermally oxidized SiO_2 layer. The oxide layer prevented diffusion of Si into the films while annealing at high temperature. The same SiO_2 layer was used for composition spread wafers. A micromachined physical shadow mask made from a Si substrate was used to separate the films into a grid of 3 mm x 3 mm regions separated by 1.5 mm as shown in the middle of Figure 1-5. Details of the micromachined shadow mask can be found in Olugbenga Famodu's thesis [98]. The pads not only made keeping track of sample positions easier but also allowed thickness measurements with profilometer.

3.2 Characterization of Magnetic Fe-Co-V composition spreads

The magnetic thin films in the combinatorial libraries must be characterized as easily and quickly as possible because of the large numbers of samples in a single library. While a number of high-throughput measurement techniques were mentioned in Chapter 1, more traditional one-by-one measurements are still needed such as the vibrating sample magnetometer (VSM). Traditional measurements were only used if necessary because of their time-consuming nature in a combinatorial study.

The Kerr effect used for the scanning MOKE is sensitive to the film surface since visible light only penetrates about 10 nm into the film [36]. In comparison, the VSM measures the whole volume of the magnetic sample gaining quantitative information about the total magnetization. A limitation for MOKE is that the change in polarization of light is only proportional to the magnetization so that the MOKE

signal needs to be calibrated to a known standard. While the MOKE "moment" is only qualitative, the coercive field measured by MOKE is reliable. The comparison of MOKE and VSM measurements was important for reliably using MOKE as a high-throughput screening tool for the very thick films of 400+ nm. We present the observed discrepancies between MOKE and VSM measurements in Section 3.2.2 on MOKE measurements.

Synchrotron X-ray diffraction was used to rapidly map the crystal structure of each sample on the wafer. If necessary, wafers were cut into the individual samples to measure with VSM for quantitative magnetometry, or for scanning electron microscopy (SEM), and transmission electron microscopy (TEM), to check the microstructure. The composition spreads were mapped using WDS to gain quantitative information about the composition. After fabrication we first measure composition with WDS, followed by MOKE screening, X-ray diffraction, and finally measure VSM, SEM and TEM, though the topics will not necessarily be introduced in that order.

3.2.1 Composition verification with Wavelength Dispersive Spectroscopy

Initial Fe-Co-V composition spread wafers were made in Bochum, Germany at the Ruhr University. The geometry of the Bochum sputtering gun was confocal such that the sputtering guns point towards the center of the wafer. The Bochum chamber is designed for 4-inch wafers and so 342 samples were measured for composition versus the 177 samples on the 3-inch wafer. A comparison of ternary plots and gun geometries for the Bochum and Maryland sputtering setup is in Figure 3-1. The Maryland sputter chamber uses a 3-gun non-confocal geometry. Non-

confocal geometry means that the sputter guns point directly downwards and are not adjustable. The confocal guns in the Bochum chamber were not properly adjusted to include the low vanadium area missing in the top ternary of Figure 3-1. An asymmetry in the shape of the composition points for the Bochum ternary is also noticed when comparing to the Maryland ternary. This can be ascribed to the fact that
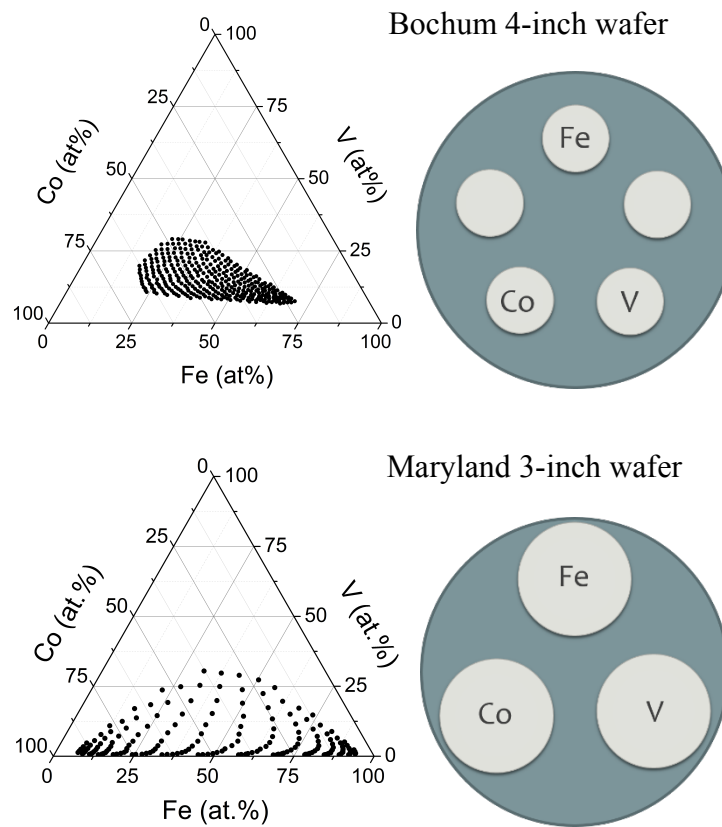
Figure 3-1 WDS results and gun configurations of Bochum and Maryland wafers. The 5-gun geometry was confocal while the 3-gun Maryland geometry was non-confocal. The confocal guns in the Bochum setup were not properly adjusted so the ternary composition diagram does not reach low V composition. In addition, the V target is closer to the Co target in the Bochum setup resulting in an asymmetry of the Bochum ternary.

the Co target in the Bochum setup is closer to the V target. The Maryland setup has equal spacing between the target and so the shape of the ternary plot is comparatively symmetric. The wafers are referred to as Bochum wafer and Maryland wafers. Details of the WDS measurement are described in an earlier introduction found in Section 1.4.1.

3.2.2 Scanning MOKE measurements

After composition measurements, the libraries are screened for magnetic properties using the scanning MOKE setup described in Section 1.4.4. We present the MOKE hysteresis loops with applied field from the Maryland wafer where a large fraction of the Fe-Co-V ternary was mapped. The goals of the screening MOKE measurements on Fe-Co-V films were to:

(1)   Establish MOKE as a high-throughput screening method for permanent magnetic films with about 500 nm thicknesses.

(2)   Identify discrepancies between qualitative MOKE screening and quantitative VSM measurements.

(3)   Use the MOKE screening capabilities in the study of composition gradient and thickness gradient libraries.

There are a number of high throughput magnetic characterization techniques including scanning SQUID magnetometer [99], XMCD [100], and the scanning hall probe [101]. Scanning SQUID has the advantage of quantitative magnetization information but cannot determine the coercive field directly. XMCD is a powerful element sensitive technique and can be used to measure hysteresis loops and determine magnetization semi-quantitatively with a calibration standard. However,

beam time for XMCD at national synchrotron facilities is competitive and costly. Finally, scanning hall probes are expensive and delicate instruments that have a limited scanning area of centimeters. MOKE has a number of advantages in that it is relatively affordable and robust and can measure the coercive field directly. This is particularly important for permanent magnetic materials. Disadvantages of MOKE include its limitation to measuring the surface and its semi-quantitative signal that requires a known calibration standard for attaining relative magnetization. MOKE imaging has already proven itself to be useful in determining magnetic properties of combinatorial diffusion couples in permanent magnetic systems [102]. As part of establishing MOKE as a high-throughput screening technique for thicker permanent magnetic thin films we will show that MOKE's qualitative results help to identify regions of interest for further study.

Next, we discuss the basic setup of the MOKE screening. Examples of individual hysteresis loops for in-plane (longitudinal setup) and out-of-plane (polar setup) directions are in Figure 3-2. This is in preparation for the hysteresis maps that show the loops for hundreds of different samples across the wafer without the axes. The direction of the applied magnetic field for in-plane and out-of-plane measurements is indicated in the top left of Figure 3-2. The longitudinal setup for in-plane measurements applies the magnetic field in the plane of the film and measures the component of magnetization along the field direction. Conversely, the polar setup applies an out-of-plane field and measures the out-of-plane component of the magnetization. As magnetic moments of each component change with the sweeping

of the external applied magnetic field, a magnetic hysteresis loop is traced out with the help of LabView.

In the interest of the second goal of finding discrepancies between MOKE and VSM measurements, we compared of VSM and MOKE loops for the same samples in Figure 3-2. The in-plane comparison of MOKE and VSM loops shows good agreement in the top right. Generally, in-plane MOKE loops were found to agree well with VSM measurements. The comparison in the bottom left for out-of-plane loops of VSM and MOKE is encouraging because the coercive fields agree for the two loops. However, the second comparison of out-of-plane loops on the bottom right shows considerable disagreement of the two different measurements. We can attribute these discrepancies to MOKE being sensitive only to the surface, while VSM measures the whole volume of the sample. There are a number of possibilities for surface effects of magnetic alloys including oxidation, elemental surface segregation (vertical composition gradient), and others [103]. More detailed discussion of discrepancies will be presented in Section 3.4 on the thickness dependent study.

Now for the third goal of applying the MOKE screening we now present some results on the MOKE screening of Fe-Co-V composition gradient libraries. A MATLAB program was used to automatically parse and plot the 177 hysteresis loop data files as in Figure 3-3 presented below. The maximum field for the out-of-plane hysteresis loop map is 5.3 kOe, and for the in-plane hysteresis loop map maximum field is 4 kOe. The hysteresis loops are plotted in their respective positions for each sample and no axes are included to ease viewing the large amount of data. The sputter gun positions are labeled with respect to the wafer position in the figure to indicate

the regions of high content for each of the three elements. The out-of-plane data had a positive slope subtracted from all the loops to better represent the saturation points of the hysteretic loops. Loops were corrected to look like a traditional VSM hysteresis loop where saturation magnetization with positive field gives a positive magnetization value. MOKE can sometimes reverse these values depending on the cross polarizer settings used to maximize the signal difference.
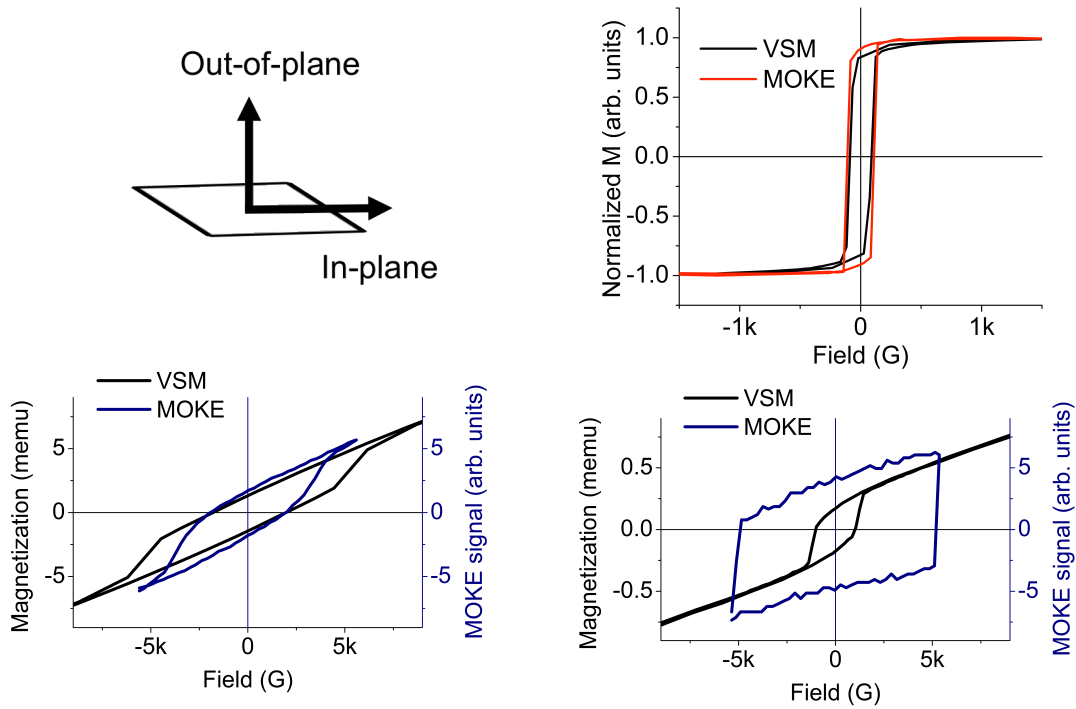
Figure 3-2 (top left) Arrow indicates field direction for the two orientations measured with MOKE where out-of-plane corresponds to polar mode and in-plane corresponds to longitudinal mode. (top right) Comparison of in-plane MOKE and VSM loops showing their good agreement. (bottom left) Example comparison of out-of-plane MOKE loop (blue) and out-of-plane VSM (black) loops. Measured on the same 350 nm thick $Fe_{52}Co_{39}V_8$ sample. Notice that both loops cross zero magnetization at the same field indicating they both measure the same coercive fields, but other features of the loops are different. (bottom right) Second out-of-plane MOKE and VSM comparison for thinner film of 83 nm and composition of $Fe_{64}Co_{28}V_8$. Large discrepancies are noted for coercive field and loop shape.

MOKE Out-of-plane hysteresis map
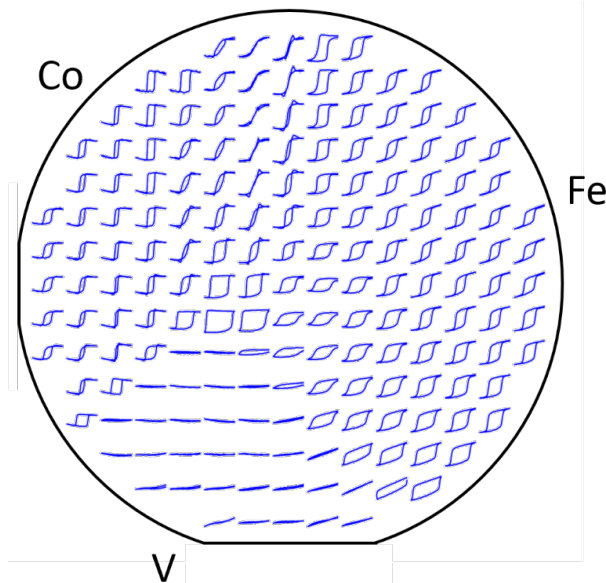
MOKE In-plane hysteresis map
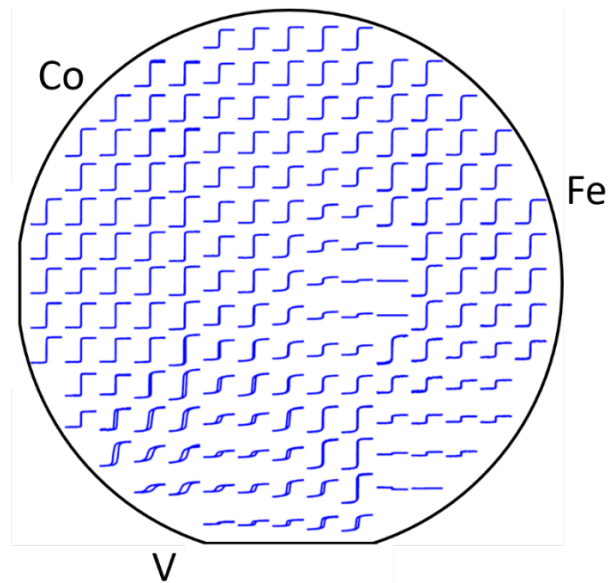
Single out-of-plane loop
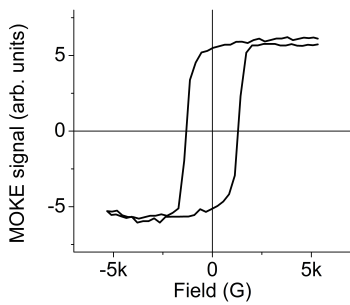
Single in-plane loop
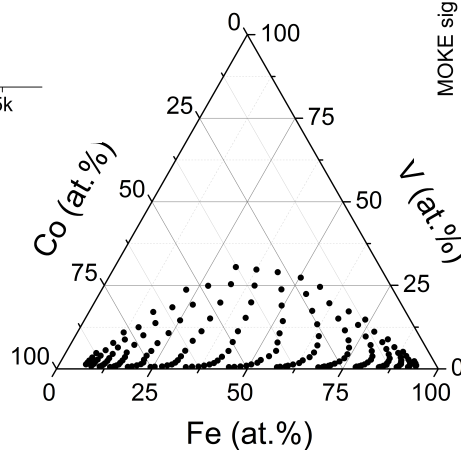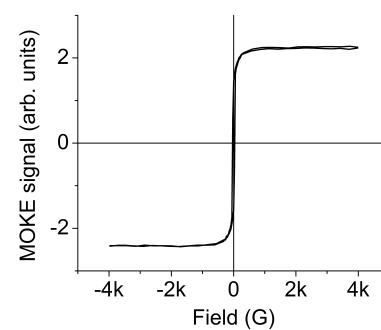
Figure 3-3 MOKE screening results of Maryland wafer showing the OOP hysteresis map on the top left where the shape of the loops clearly distinguishes between the V, Fe, and Co regions. The IP hysteresis map is shown on the top right where the loops are significantly skinnier than in the OOP map. The artifact in the IP map where there is no loop towards the iron rich side is likely an alignment error during the automated measurement. Examples of single loops give scales for the applied magnetic field for their OOP and IP counterparts. The ternary composition plot is given for reference at the bottom.

From the discussion of discrepancies, we can expect that the in-plane hysteresis maps should give reliable hysteresis loops that provide relative magnetization, coercive field, and even energy products. The value of MOKE screening cannot be overstated when we compare MOKE screening to the one-by-one method using VSM. The wafers need to be cut into separate pieces for VSM and the sample needs to be changed every 5 minutes for 20 hours if one wants in-plane and out-of-plane measurements. In comparison, the MOKE measurements require about 3 hours sample mounting and calibration for both in-plane and out-of-plane measurements and the rest is automated measurement.

The combinatorial scientist can look at the hysteresis maps and with reference to the ternary plot and general knowledge about the known aspects of the material system, could discover new and exciting regions of interest. If we compare this hysteresis map visualization to the one-by-one method of looking at each hysteresis loop individually, the task becomes a laborious guessing game. The advantage of the hysteresis map is that trends can be easily identified. In Section 3.4 we address this question using the thickness dependent library and show that while the MOKE screening is not quantitative for coercive field or for magnetization, the major trends of coercive force do agree between the screening results and quantitative VSM results.

The main result here is that MOKE screening is a valuable high throughput method to quickly find regions of interest in permanent magnetic thin film systems. Our MOKE screening results showed us that coercive fields from in-plane hysteresis loops for Vicalloy type compositions gave about 300 Oe which agreed with bulk

values. In addition, the out-of-plane map shows some more interesting results with coercive fields of about 5 kOe in the high V region. While these results appear promising they need to be confirmed with quantitative VSM measurements as in the next section. The in-plane hysteresis maps did not reveal any new regions of interest for Fe-Co-V.

Finally, the MOKE hysteresis loop contains information about the coercive field, relative magnetization, remanent/saturation magnetization ratios, and energy product, among other quantities that can all be automatically calculated for large numbers of samples and plotted versus composition, thickness, or other quantities. Detailed discussion will follow in Section 3.4 on the thickness dependent Fe-Co-V study that takes advantage of these capabilities.

3.2.3 VSM Measurements and Maximum Energy Product

Next, we confirmed the MOKE screening measurements using quantitative VSM. This was a necessary step in the process of confirming the use of MOKE as a screening tool for the thicker films used in the study. Initial discrepancies were found between MOKE and VSM measurements, however we will later show that trends are preserved across the two techniques. The basics of VSM measurement can be found in Section 1.4.5.

To carry out VSM measurements samples need to be smaller than 5 mm in diameter. To achieve this, the wafers need to be cut into smaller pieces for VSM measurement. An example of a chopped wafer is presented in Figure 3-4 for the 4-inch wafer from Bochum. Each square is a sample that was cut and labeled on the backside. Some of the wafer peeled at high vanadium content in the lower right side.
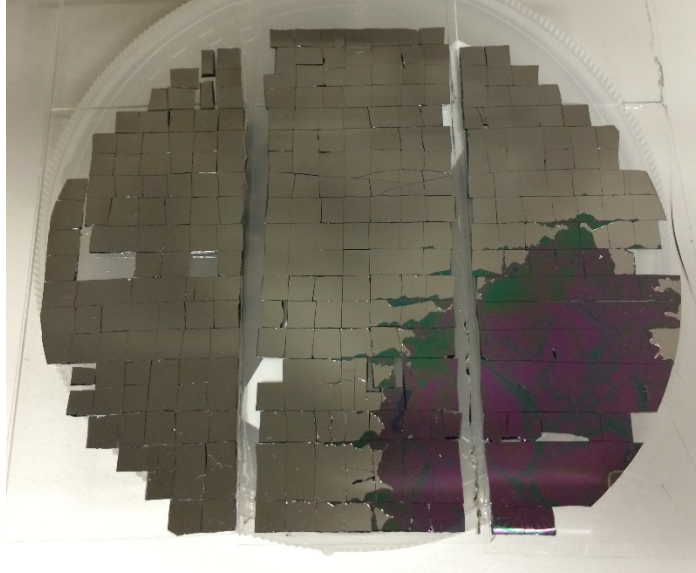
Figure 3-4 Chopped Fe-Co-V Bochum wafer showing the individual samples. The wafer has 342 samples on it and is 4 inches in diameter.

In Figure 3-5 we present the VSM M(H) loops for a representative $Fe_{38.4}Co_{53}V_{8.6}$ Vicalloy thin film of 350 nm thickness. The in-plane loop agrees well with MOKE results in Figure 3-2 and shows a coercive field of 300 G as expected for bulk Vicalloy samples [85]. It's apparent that the remanent magnetization, or the magnetization at zero applied field, is considerably lower than the saturation magnetization. This is most likely because the thin films are polycrystalline as later verified by X-ray diffraction. This means that a number of different easy axes lie in the film plane. Since we know that grains of different orientation switch at different fields, then the decrease in remanence is to be expected [74]. The saturation magnetization from the in-plane VSM measurement of this Vicalloy composition gave 10,000 G (SI) or about 800 emu/cm^3 (cgs) which also agrees with other investigations [85]. Based on the composition, the heat treatment, and the lack of cold-working this effectively a Vicalloy I thin film. We also calculated the energy

product for our thin film as 1 MGOe and found good agreement with literature for this particular Vicalloy [85] .
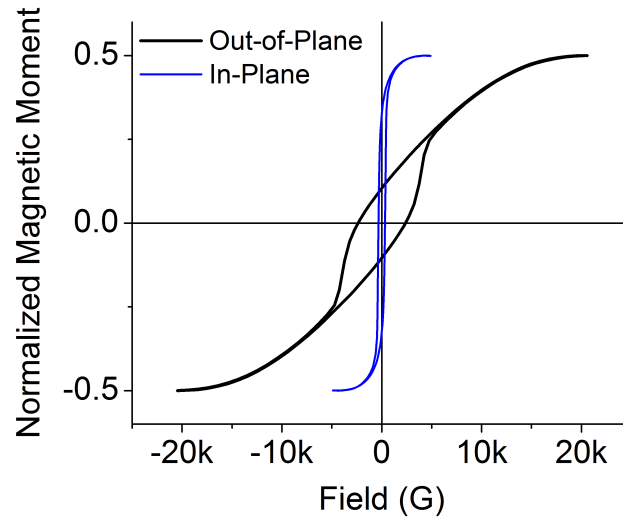
Figure 3-5 VSM results for in-plane and out-of-plane M(H) loops of an $Fe_{38.4}Co_{53}V_{8.6}$ sample. Data was normalized for ease of viewing between saturation of in-plane and out-of-plane loops.

The out-of-plane loop shows an increased coercive field with what appears to be a linear slope due to the demagnetizing field from the shape anisotropy of the thin film itself. In addition, the out-of-plane remnant magnetization is decreased dramatically. All these characteristics indicate an in-plane oriented easy axis and an out-of-plane hard axis. The precise switching mechanism can help understand the reason for this increased coercive field when measuring out-of-plane to distinguish if it is simply a thin film effect or is an intrinsic material property useful in new applications. Thin film effects can be any consequence of the material from being in an extremely flat and thin form. As described in Section 2.4.3 on shape anisotropy,

93
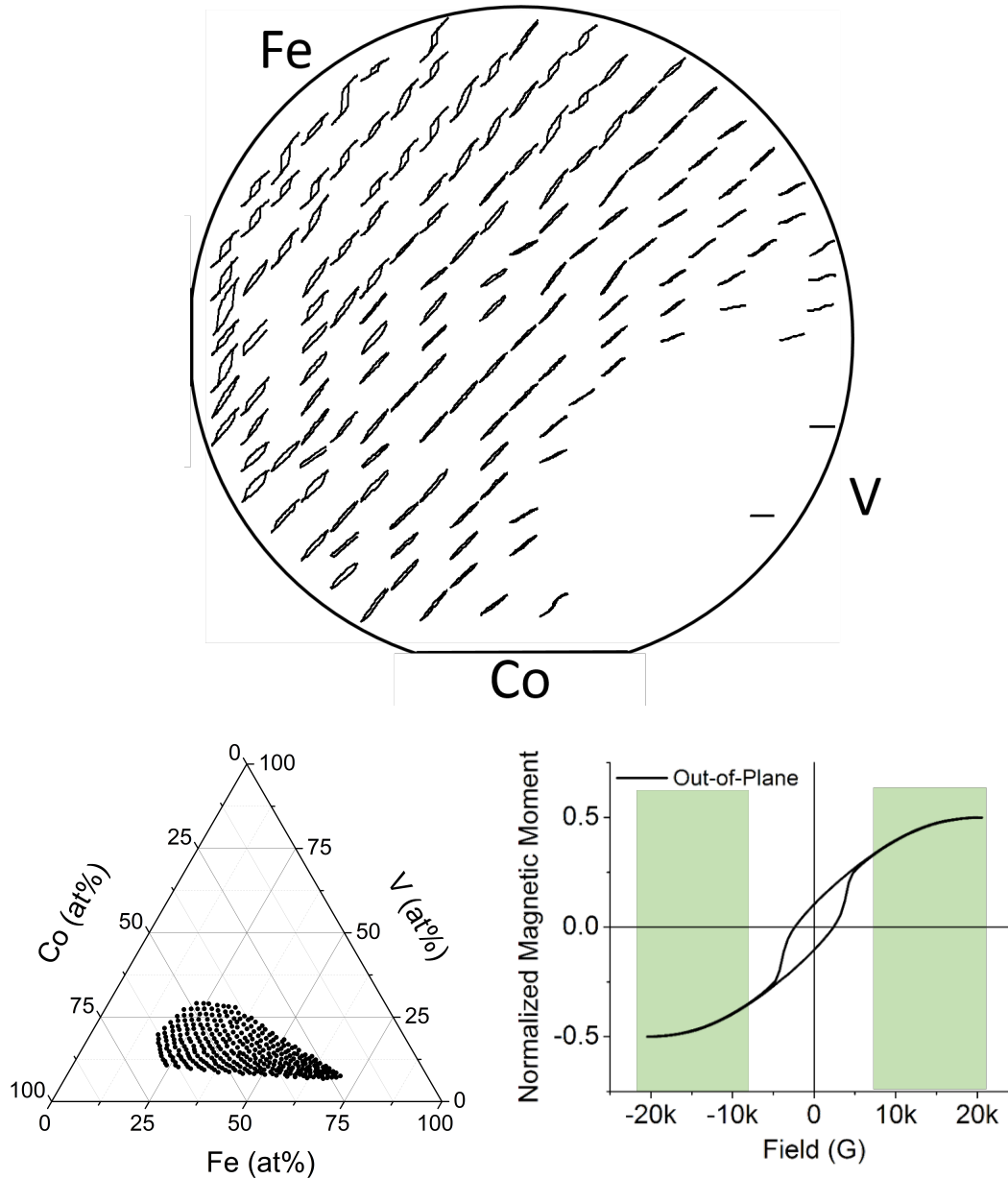
Figure 3-6 Out-of-plane VSM hysteresis loops presented in the form of a map on top. The ternary diagram of the same samples is presented for reference in the bottom left. The bottom right shows the areas of truncation that are shaded. By truncating the loops they are easier to display in the hysteresis lap without overlap while preserving the important information of the inner loop.

the fact that a thin film can be approximated as an infinite plane has considerable consequences for its magnetic properties. The precise consequence of being a thin film on the switching mechanism will be explored in Section 3.3 on switching fields.

For a more complete comparison of MOKE to VSM results we chose select samples for VSM measurements. Figure 3-6 shows the VSM hysteresis map of the Bochum wafer with the ternary composition diagram for reference. The usefulness of the hysteresis map is clear in that it increases the facility of finding regions of interest. For permanent magnets, one needs to simply look for wide loops in the hysteresis map to identify promising areas. In this case, the out-of-plane hysteresis loops were truncated as shown in the lower right of Figure 3-6, in order to ease displaying the large number of loops in such close proximity to one another.

From the quantitative information of the VSM hysteresis map it was possible to calculate the corresponding energy products from the loops and create an energy product map on the ternary composition diagram as displayed in Figure 3-7. To calculate the energy product we first used the thickness and size of each sample to calculate the magnetization from the moment measured by VSM. The M(H) loops were then converted into B(H) loops by adding the field to the magnetization as in equation (5) in Chapter 2. Then, the field and induction values were multiplied by each other for each different field and the maximum of this BH plot was hence the $(BH)_{max}$ value. The map shows a clear maximum of energy product around the previously known Vicalloy compositions of $Fe_{40}Co_{52}V_8$. The energy product of 2 MGOe is the value associated with a considerable cold-working and final annealing as discussed in Section 2.7. Although our samples did not undergo cold-working, they

certainly have a strong geometric restriction from being in the form of a thin film. We may attribute this increase above 1 MGOe as due to the thin film geometry. Thin film geometry simply refers to the fact that thin films have an infinitely larger length and width, than depth.

In-Plane Fe-Co-V Energy Product
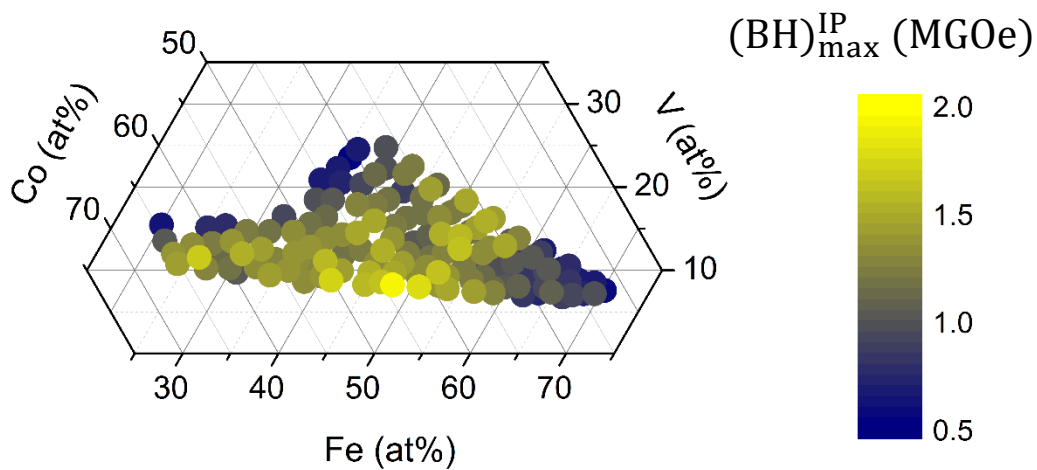
Figure 3-7 Energy product map calculated from in-plane VSM loops of the Bochum wafer. The energy was color mapped and the plotted on the ternary composition diagram for the Fe-Co-V system.

In addition to energy product maps on the Bochum wafer, we also analyzed an Fe-Co-V library made at Maryland to study the lower vanadium compositions (below ~6 at% V) which were not included in the Bochum wafer. The samples with the highest energy product were at the edge of the Bochum wafer so the Maryland library can confirm those are indeed the best compositions. Figure 3-8 shows the plot of in-plane maximum energy product, $(BH)_{max}$, versus the vanadium compositions of nominally equiatomic Fe-Co alloys from the Maryland library. The plot shows a clear

maximum in energy product of 1 MGOe at 8 at% V as found previously in our study

and supported by literature [85], [90], [92]. This confirms the results shown in the

previous (BH)$_{max}$ maps and shows that Vicalloy thin films have similar properties as

their bulk counterparts.
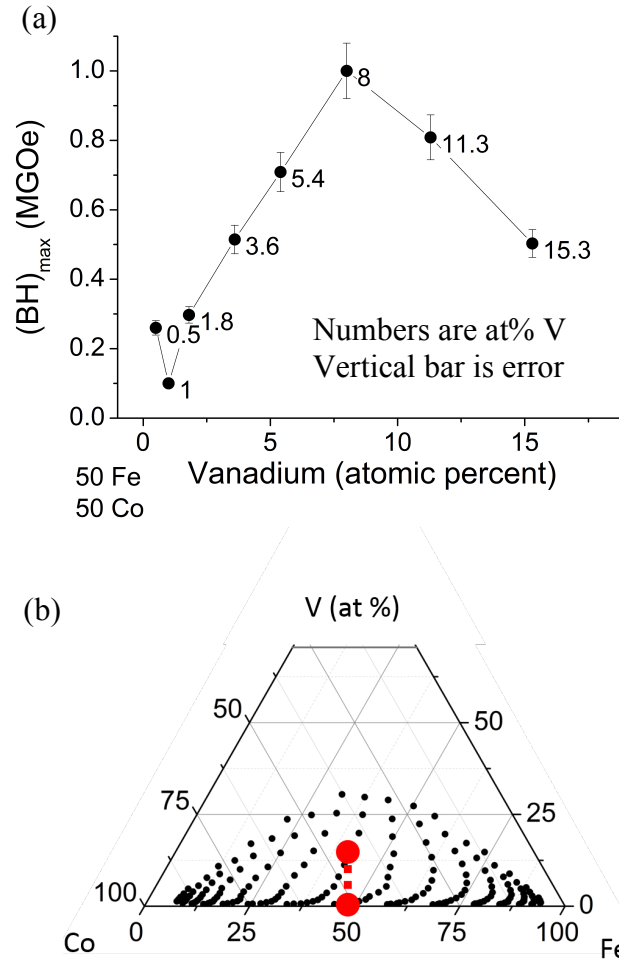
Figure 3-8 (a) Maximum energy product calculated from in-plane VSM hysteresis loops is plotted versus the vanadium content of equi-atomic Fe-Co alloys. Each point is labeled with at% V and the error in energy product is shown as vertical bars. (b) Ternary for the Fe-Co-V library where the red line shows nominal compositions which are plotted in (a).

Another interesting feature of the top plot in Figure 3-8 is the minimum of $(BH)_{max}$ at about 1 at% V. The Fe-Co-V composition with 2 at% V is the well-known Permendur alloy, popular for its soft magnetic properties and ease of machinability [7], [83]. A minimum of the $(BH)_{max}$ indicates a soft magnetic property which may be the Permendur effect. The utility of the combinatorial method is apparent here where it has allowed us to accurately confirm optimal compositions for two interesting engineering materials in different composition regions of a ternary system.

3.2.4 Transmission and Scanning Electron Microscopy

Microstructural measurements using SEM and TEM were carried out to understand how the microscopic shape and size of the alloyed grains might contribute to the observed thin film or intrinsic magnetic properties. Grain size and orientation play a huge role in magnetic materials. Shape anisotropy was responsible for the enhanced coercive field in alnico permanent magnets and pinning sites in nano-grained rare-earth permanent magnets were responsible for the increase of energy product since the discovery of Nd-Fe-B magnets.

We first present results of SEM images of the Vicalloy thin film cross section in Figure 3-9. The SEM cross-section images did not reveal detailed grain size or orientation information but did help confirm film thickness. The SEM planar image in Figure 3-10 revealed a fine grain size of about 50 nm and also showed distinct cracks in the film. The cracks in the films indicate there could be large stresses in the films but were relaxed through cracking. The images were taken with a Hitachi SU-70 operating at 10 kV.

TEM images were also taken on a representative Vicalloy sample. The bright field image in Figure 3-11 reveals a very fine grain structure similar to the period observed in planar SEM images. A number of sharp grain boundaries can be observed which are likely to be the (111)‖(011) orientation preference of the gamma and alpha phases respectively. This preferential direction will be shown in the X-ray diffraction spectra in Section 3.2.5 and the selected area electron diffraction of this section.
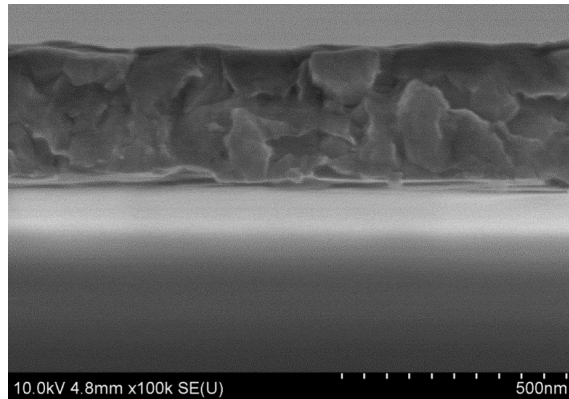
Figure 3-9 SEM cross section of a $Fe_{53}Co_{38}V_9$ Vicalloy sample. Microstructural information was not clear in the image. Image courtesy of NispLab.
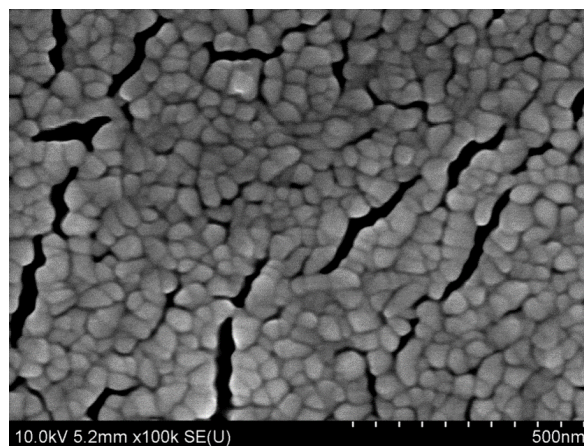
Figure 3-10 Planar SEM image of a $Fe_{53}Co_{38}V_9$ Vicalloy sample. The grain size is clearly shown to be about 50 nm. Cracks also reveal some relaxing of a highly strained film. Image courtesy of NispLab.

It appears there is some columnar alignment of the grains that could contribute to some out-of-plane shape anisotropy of the samples. Any measureable shape anisotropy would have a signature switching field dependence when measuring different out-of-plane hysteresis loops. This point will be considered in the switching field experiments in Section 3.3.
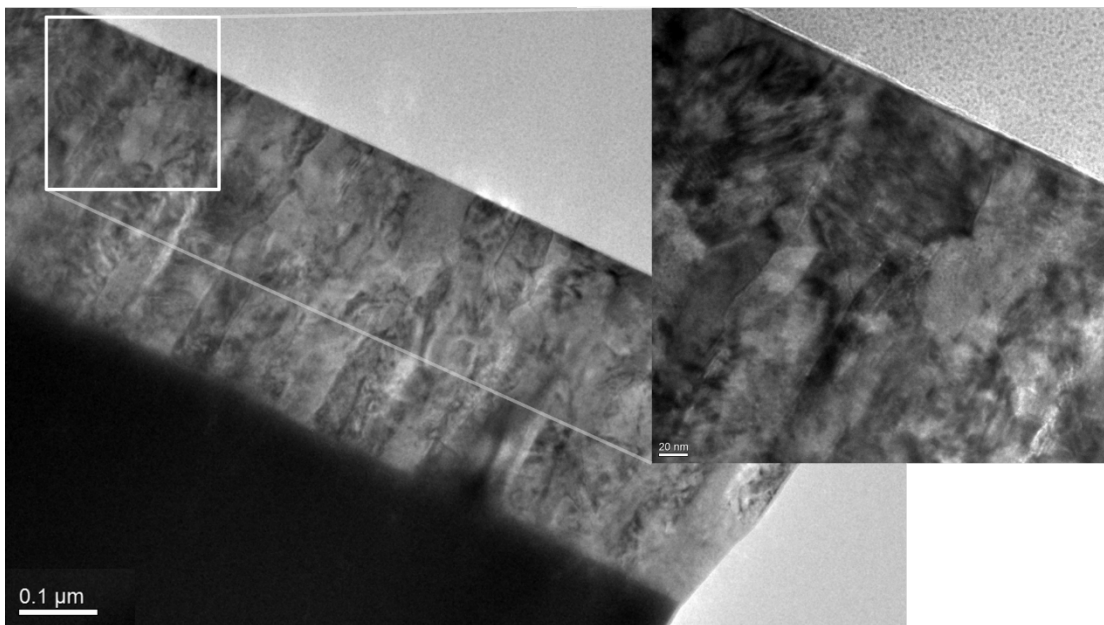
Figure 3-11 TEM images of the $Fe_{53}Co_{38}V_9$ Vicalloy thin film sample. The close-up region shows some clear grain boundaries indicating the (111)||(011) preference of the two phases. Images courtesy of Alfred Ludwig's lab and Dennis König.

The selected area electron diffraction (SAED) image is show in Figure 3-12. SAED is a TEM technique where an electron transparent sample has a focused electron beam shot through the sample as in transmission mode. The center bright dot in Figure 3-12 is the main electron beam coming through without being scattered or diffracted. Crystals with atomic planes that meet diffraction conditions create spots on

the phosphor screen at different distances from the center measured in inverse length. Figure 3-12 shows the scale bar of 21 nm^{-1}. The satisfaction of the diffraction axis is also synonymous with the alignment of the crystal zone axis. Different radial orientations of the planes give different spots along the radial angle depending on the rotation angle of the zone axis itself. Since we see only a number of dots we can assume the number of crystals struck by the electron beam was small during this measurement. If the beam activated a large number of randomly oriented crystals, the diffraction pattern would form rings. Similarly, an amorphous material would also form diffraction rings in an SAED pattern.
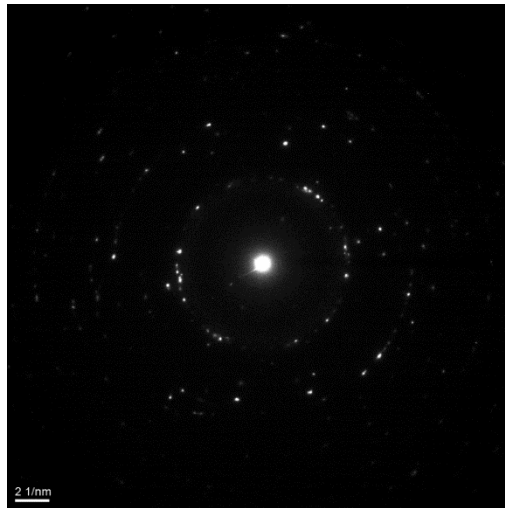
Figure 3-12 SAED image of the above $Fe_{53}Co_{38}V_9$ Vicalloy specimen. The center dot is the un-diffracted electron beam while spots indicate differently oriented crystals of varying lattice spacing and orientation. Image courtesy of Alfred Ludwig's lab and Dennis König.

The SAED image can be integrated radially to see the SAED spectra as in Figure 3-13. Similarly to the X-ray diffraction spectrum earlier, we have identified the main γ- and α- phase peaks and confirmed that they agree with literature.
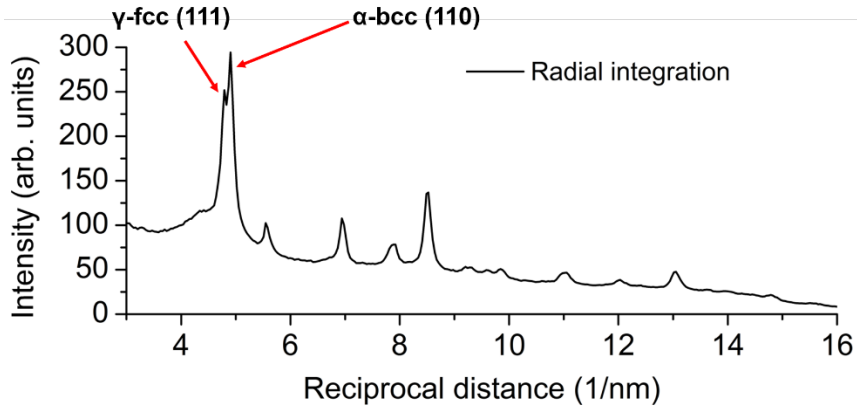
Figure 3-13 Radially integrated SAED image to get the SAED spectra for the $Fe_{53}Co_{38}V_9$ Vicalloy sample. Gamma and alpha peaks have been identified and were confirmed to agree with X-ray diffraction.

3.2.5 High Throughput Synchrotron X-Ray Diffraction

Figure 3-14 shows the synchrotron X-ray spectra for a typical thin film Vicalloy type sample. Data from the Bochum wafer and Maryland wafers are presented and agreement of the crystal phases was confirmed between them. Rietveld refinements were carried out on the X-ray spectra using the Bruker software package TOPAS. Rietveld refinement is able to input a crystal structure and its parameters and fine-tune the parameters' like lattice spacing (d-spacing), grain size, and texturing using known relations about their effect on the shape and position of the peak. We find the presence of the known body-centered cubic alpha (α-bcc) phase with a strong

(110) preference and the face-centered cubic gamma (γ-fcc) phase with a strong (111)

preference. Agreement in these relatively thick films with bulk crystal structure and

d-spacing was found where literature for bulk phases gave $a_\alpha^{lit} = 2.860$ Å and

$a_\gamma^{lit} = 3.575$ Å. Results of Rietveld refinement from synchrotron diffraction on our

thin film samples gave $a_\alpha = 2.900$ Å and $a_\gamma = 3.615$ Å. Some discrepancies of

lattice parameters have been previously mentioned and may give information about

the ordering in the vanadium rich gamma phase [7], [104].

Figure 3-15 displays a series of synchrotron diffraction spectra of different

vanadium contents. Higher vanadium phases include the expected tetragonal σ-phase

appearing above 20 at% V [105].
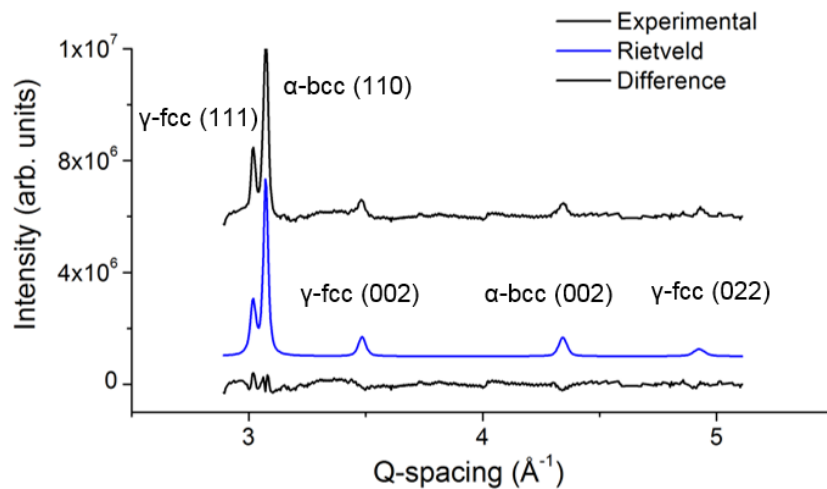
Figure 3-14 Synchrotron X-ray spectra from a $Fe_{56}Co_{23}V_{11}$ sample showing Rietveld refinement and the difference of the two. Peaks are labeled with phase and orientation.
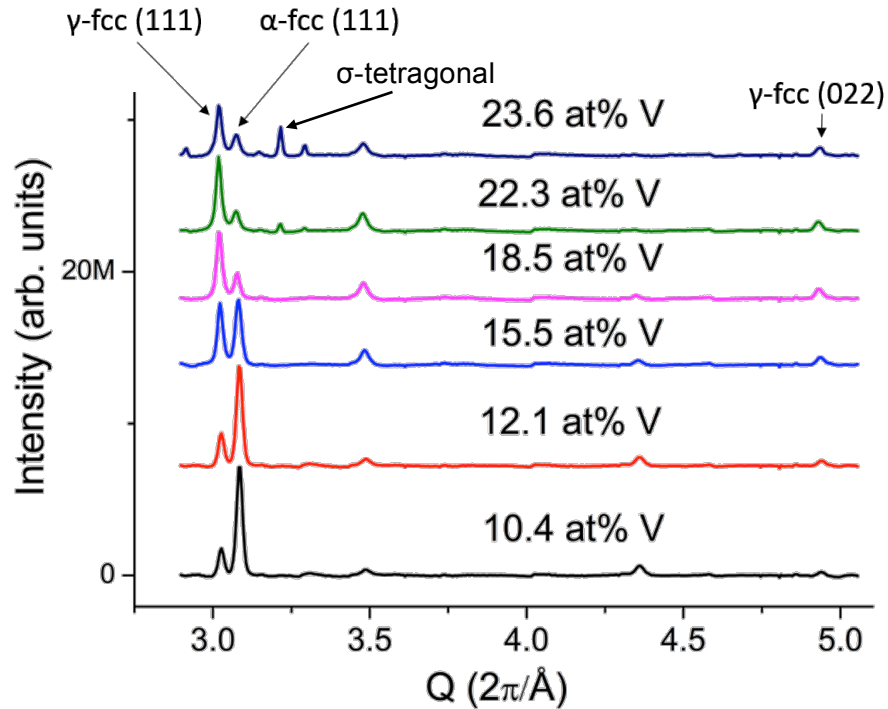
Figure 3-15 Synchrotron diffraction of a series of increasing vanadium Fe-Co-V alloys. The (110) α-peak is seen to dominate at lower vanadium content while by 15.5 at% V the (111) γ-peak overtakes the α-peak. Peaks of the σ-phase appear above 18.5 at% vanadium as expected.

3.3 Angular Dependent Switching Fields of Fe-Co-V Thin Films

The following study of angular dependent switching fields is to address the following issues that arose during the combinatorial thin film study of the Fe-Co-V system.

(1) What is the precise origin of the increased coercive field in the out-of-plane M(H) loops?

(2) Is there any shape anisotropy contribution to the Vicalloy sample as observed in TEM images?

(3) What can we learn about the magnetic switching mechanism in Vicalloys, which has received little attention in the literature?

First, we briefly discuss the validity of switching field experiments on our thin film samples and then introduce the experimental setup for the angular switching field measurements. The angular dependence of hysteresis loops is well known based on exact analytical solutions for different switching mechanisms including rotation and 180° domain wall motion [60], [61], [73], [76]. This background was discussed in detail in Section 2.5. The approach then is to measure magnetic hysteresis loops with the applied magnetic field at different angles with respect to the sample place. The validity of this measurement for use on polycrystalline thin film samples comes from the fact that the easy axis is well aligned in the film plane as discerned by the squareness of the in-plane loop compared to the out-of-plane loop. Thereby we can say that with respect to the out-of-plane axis, we are indeed measuring with respect to aligned particles that lie in a single plane of the film. These theories, for example, do not apply to randomly oriented magnetic particles or to the in-plane axis of a polycrystalline thin film sample.

The thin film samples are mounted on the VSM sample holder such that rotation of the sample rod changes the out-of-plane angle, φ_H, with which the magnetic field is applied to the plane of the thin film as in Figure 3-16. The operation of the VSM can be reviewed in Section 1.4.5. The switching fields were measured at a number of angles between 0° and 90° where 0° is the in-plane direction and 90° is the out-of-plane direction. Ten samples of different V compositions were chosen with nearly equiatomic Fe and Co from the Maryland wafer. The dependence of the

switching fields on vanadium content will help to understand how the different crystal phases influence the switching mechanism.
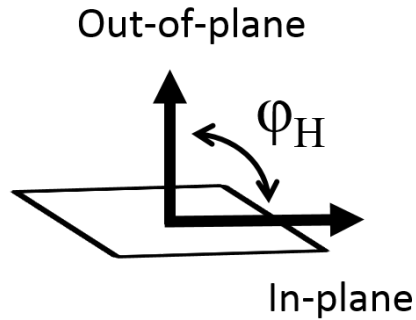
Figure 3-16 Definition of the out-of-plane angle, φ_H, where 0° is the in-plane direction and 90° is the out-of-plane direction.

The results of the angular dependent switching fields for vanadium compositions from 0.5 at% V to 8 at% V are presented in Figure 3-17. Because the Kondorsky function is an inverse cosine function we plot the inverse switching field versus the cosine of φ_H. This results in a linear function for easy detection of non-linear, and hence non-Kondorsky type relations. The first impression of Figure 3-17 is that for all the vanadium compositions shown, the switching fields are linear for the inverse switching field versus $\cos \varphi_H$. This result indicates that for the compositions shown that the switching mechanism is likely a Kondorsky type 180° domain wall switching mechanism. Angular dependence of switching fields is not conclusive evidence of the type of switching mechanism. Direct evidence would be microscopic confirmation using Lorentz microscopy or MFM images at different fields to observe to type of switching present at the grain size level [106].

106
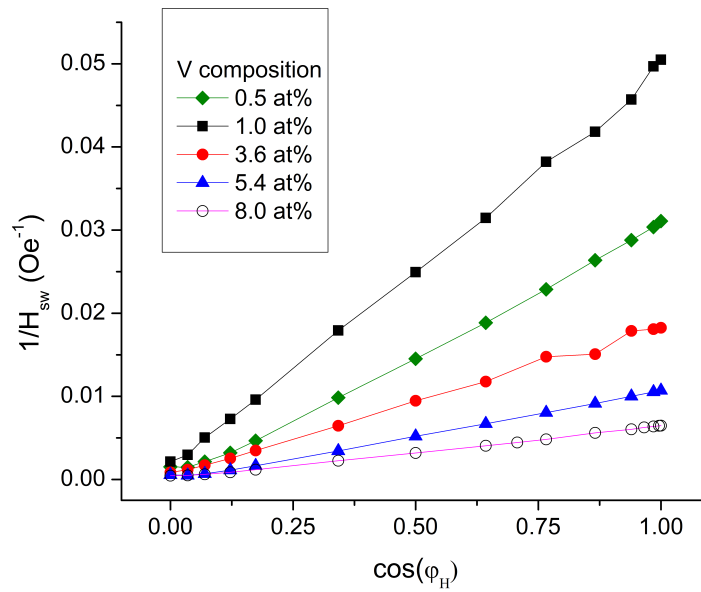
Figure 3-17 Angular dependence of switching field for vanadium compositions from 0.5 at% V to 8 at% V.

One can see that as the composition goes from 0.5 to 1 and the then 3.6 at% V, the slope increase and then decreases. The increase in slope indicates a magnetic softening while a decrease in the slope indicates a magnetic hardening, or an increase in the switching field. The highest slope at 1 at% V is near the known magnetically soft Permendur composition discussed in Section 2.7 and at the end of Section 3.2.3. As the vanadium composition continues to increase, the slope becomes smaller, indicating increasing magnetic hardness with vanadium.
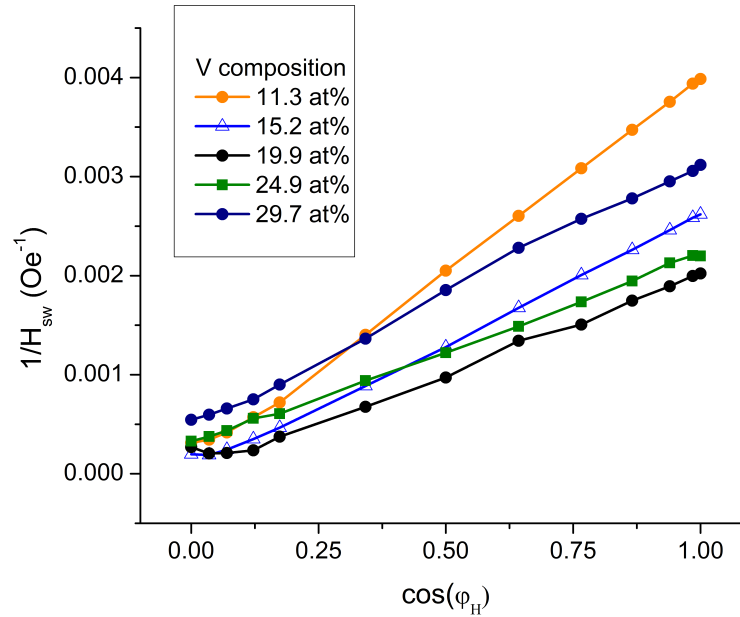
Figure 3-18 Angular dependence of switching field for higher vanadium contents of Fe-Co-V alloys.

A second switching field plot of even higher vanadium content is shown in Figure 3-18. Here, we see another transition for the slope of the switching field dependence where with increasing vanadium content from 11.3 to 19.9 at% the slope continues to decrease, however for compositions above 19.9 at% V the slope once again starts to increase for 24.9 and 29.7 at% V. A structural phase boundary was identified earlier in section 3.2.5 where the sigma phase was observed for Fe-Co-V alloys containing more than 20 at% V. We can say here that the magnetic softening on alloys containing over 20 at% V may be from the σ-phase shown in the X-ray spectra of Figure 3-15. Table 2 shows the precise compositions of the samples used in the switching field study for reference.

All the samples were found to agree with the Kondorsky relation indicating no contributions from shape anisotropy as expected from the TEM images. The

switching field relation for shape anisotropy has a non-linear contribution as explained in Section 2.5.2. The good agreement of all the Fe-Co-V samples to the Kondorsky function suggests that the switching mechanism of Vicalloys is a 180° domain wall switching. The nature of 180° domain wall switching indicates that the mechanisms for magnetic hardness in Vicalloys is a pinning mechanism as per the derivation of the Kondorsky function in Section 2.5.2. Thus, while stress and shape anisotropy [90] have been offered in the past to explain the magnetic hardness of various Vicalloys we can say that for Vicalloy I alloys without considerable cold-work, the mechanism is likely from pinning of 180° domain walls. Additional cold-working has been observed to increase the energy product in Vicalloy II alloys [90].

Models for domain wall pinning rely on knowing the size and distribution of pinning sites of magnetic inhomogeneities such as voids or non-magnetic inclusions [107]. In addition, the relationship between the domain wall thickness and the size of the pinning sites are also important. In our Fe-Co-V films we confirmed the presence of the non-magnetic γ-phase precipitates. We propose that 180° domain wall pinning at γ-phase precipitates is a likely scenario. Unfortunately, we could not learn their size or distribution from the TEM images. Further investigation would help identify the precise pinning mechanism and offer a clear road to improving the Vicalloy permanent magnet.

Finally, the increased out-of-plane coercive field observed in the VSM measurements is likely from applying the field perpendicular to the easy axis of the 180° domain walls in the Fe-Co-V samples. The close agreement between experimental and the Kondorsky function strongly support this argument. We do note

that the remanent magnetization does not decrease to zero like in the switching field study of single-crystal CrO_2 crystal described in Section 2.5.2. This likely occurs from the fact that our Fe-Co-V films are polycrystalline and so not all grains are oriented with their easy axis in-plane. The small fraction of grains pointing out-of-plane could account for the non-zero remanent magnetization when measuring out-of-plane.

Table 2 Compositions of samples for the above switching field measurements.

Fe (at%)	Co (at%)	V (at%)
37.5	32.8	29.7
39.4	35.6	24.9
41.1	39.0	19.9
41.9	42.8	15.2
41.9	46.8	11.3
42.2	49.8	8.0
42.4	52.3	5.4
41.6	54.8	3.6
49.3	49.8	1.0
57.5	42.0	0.5

3.4 Thickness Dependent Fe-Co-V Study

There are a number of motivations to conduct the present thickness dependent study for the Fe-Co-V system. These include:

(1) Verify the thickness dependence of expected bulk and thin film crystal structures.

(2) Understand discrepancies between MOKE and VSM measurements.

(3) Validate MOKE as a useful high-throughput screening tool for thick permanent magnetic films.

Towards these goals we fabricated a natural thickness gradient combinatorial library using an alloyed $Fe_{70}Co_{30}$ target and an elemental V target. Because of the three target geometry in the chamber, there was a thickness gradient perpendicular to the composition gradient. The library gave a large composition gradient as observed in Figure 3-19. The ternary diagram shows a line because the Fe-Co ratio is always maintained at 7:3 because of the alloy target. The composition gradient also gave a large film thickness range from 500-50 nm.

A Dektak 6M profilometer depicted on the right of Figure 3-20 was used for the measurements of the thickness map on the left of Figure 3-20. The map shows very high thickness under the $Fe_{70}Co_{30}$ gun of 500 nm, while under the V target there's a thickness of about 200 nm. The black boxes indicate samples of the same nominal composition of $Fe_{65}Co_{26}V_9$ but with decreasing thickness from left to right.

The MOKE screening of the sample is displayed in Figure 3-21. It's clear that high vanadium content samples are non-magnetic. Similarly, in this diagram as the thickness diagram, the black boxes indicate samples that are nominally $Fe_{65}Co_{26}V_9$. The hysteresis map clearly shows the strong dependence of the hysteresis loop shape versus thickness as the shape goes from a typical rounded loop to an increased coercive field with a high level of squareness, and finally quickly transition to what looks like a paramagnet. Of course, these MOKE screening results need to be considered carefully because they are only qualitative, but it is clear that a dramatic change is happening below about 100 nm.
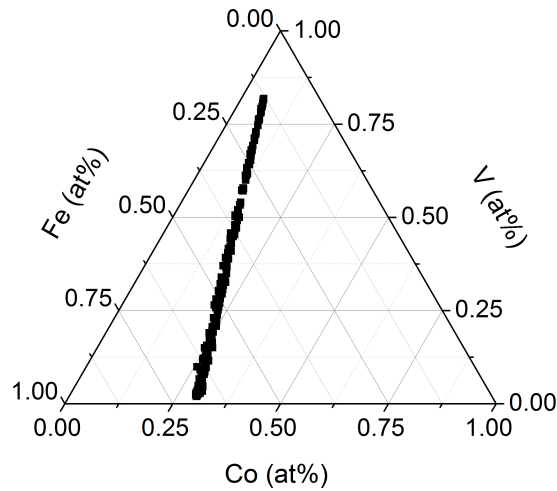
Figure 3-19 Ternary composition diagram for the $Fe_{70}Co_{30}$-V thickness dependent combinatorial library.
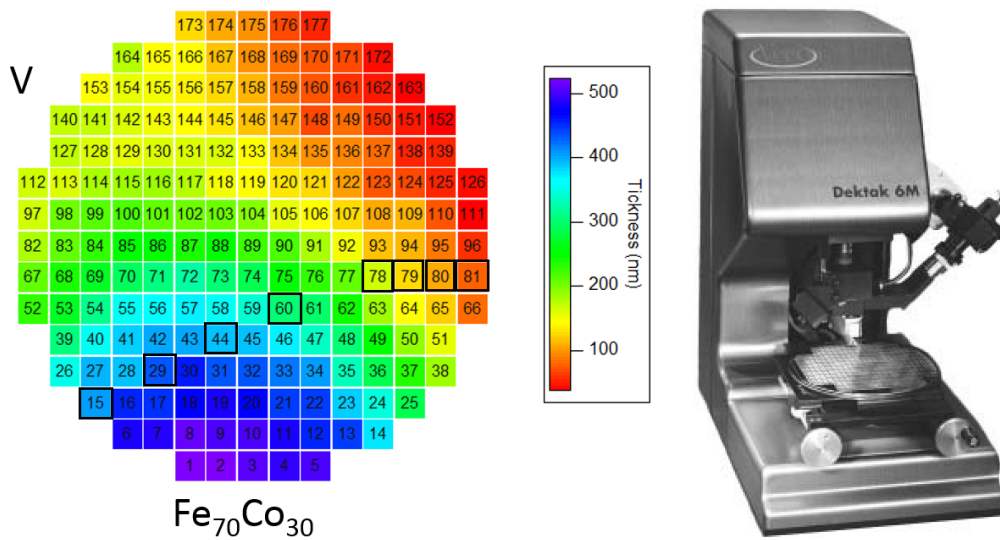
Figure 3-20 Color-coded thickness map the thickness dependent library on the left. The Dektak 6M profilometer used for thickness measurement of thin films is displayed on the right, thanks to Veeco.
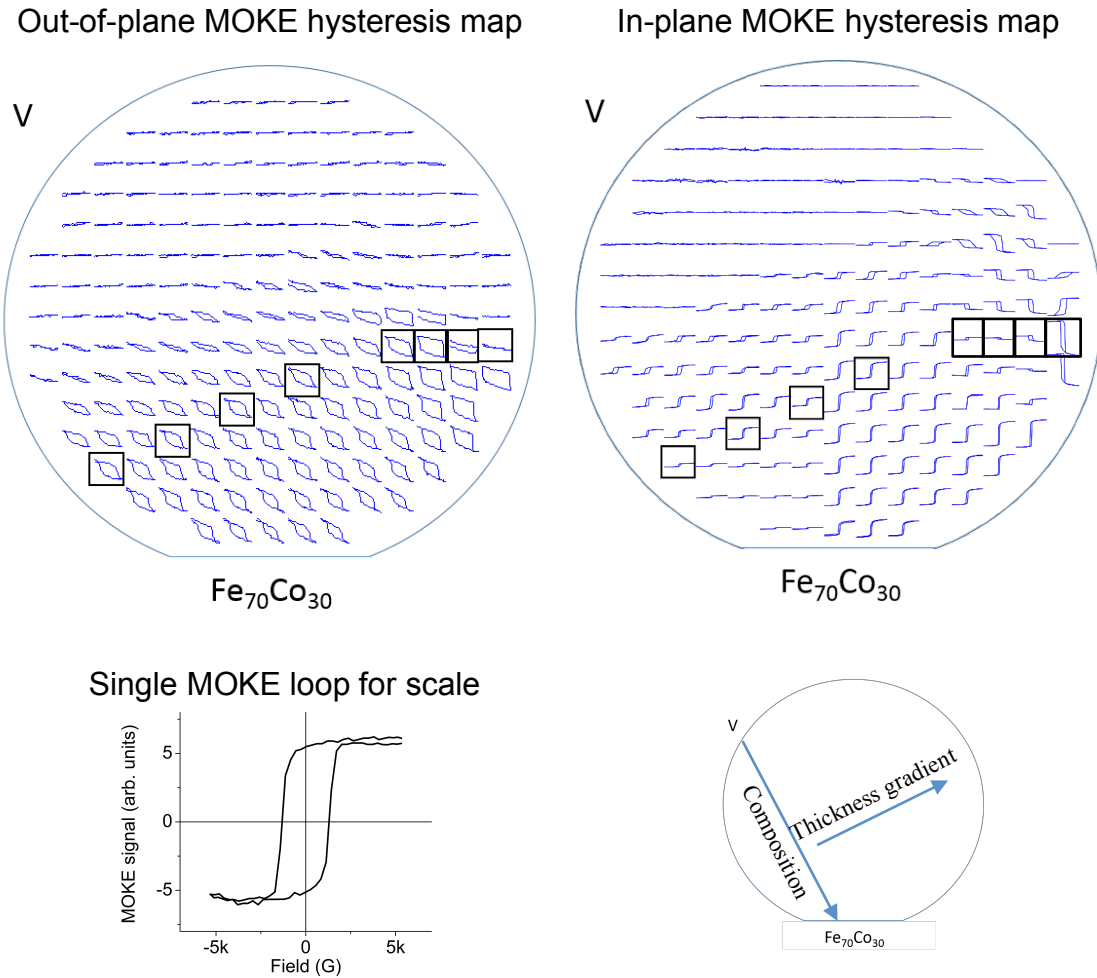
Figure 3-21 Magnetic hysteresis maps from MOKE screening of the thickness dependent library for out-of-plane (top left) and in-plane (top right). Hysteresis loops with black boxes are the same nominal composition of $Fe_{65}Co_{26}V_9$ with decreasing thickness from left to right. The hysteresis loop is seen to vary dramatically from the 500 nm thickness on the left to the 50 nm thickness on the right in both maps. A single MOKE loop is given for scale. A diagram indicating the composition and thickness gradient directions is on the bottom right. The wafers are 3 inches in diameter.

To get a closer look at the thickness dependent phenomenon we calculated the coercive fields from each of the MOKE loop using MATLAB and color plotted them on a thickness versus (vs.) composition diagram. We also measured select samples with VSM, so that they can then directly compare the results as in Figure 3-2. Figure

3-22 shows the MOKE results on top and the VSM results on the bottom. Despite the slight difference in scales for the coercive fields (H_C) there is an astonishing agreement with the trend of the coercive fields over large composition and thickness ranges. The relative coercive field of the thicker samples with low vanadium compositions agrees well between the two plots. As we go to thinner films with higher V content the trend of large coercive fields (red points) is also preserved between the plots. For thicker films with V above 20 at%, the coercive field suddenly rises and then gradually decreases until samples above 35 at% V are very soft.
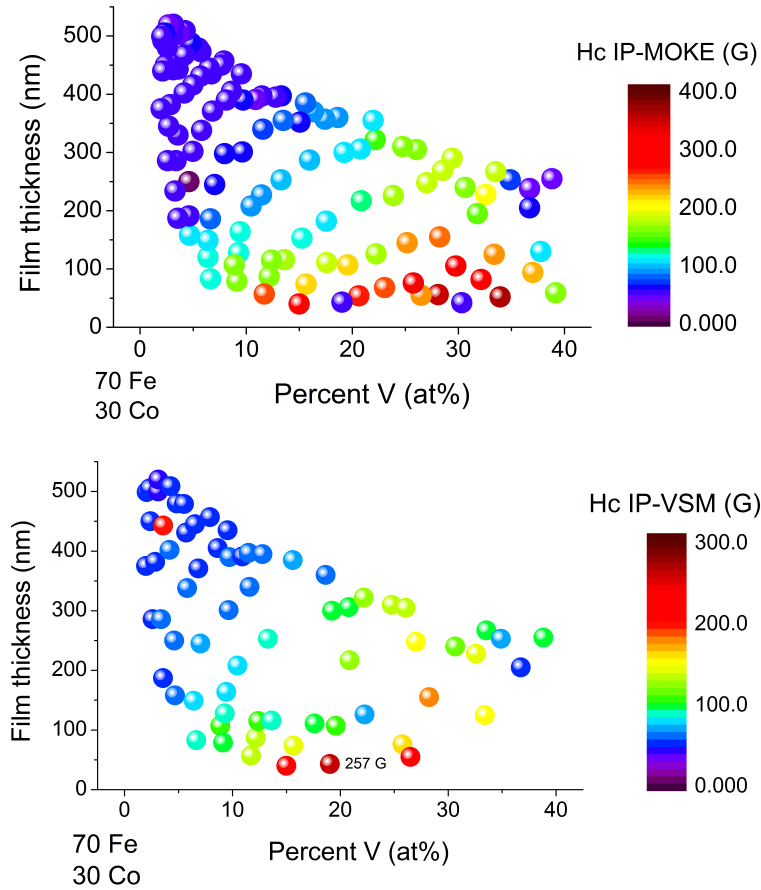
Figure 3-22 Thickness vs. composition map of in-plane MOKE coercive fields (top) and thickness vs. composition in-plane VSM coercive fields (bottom).

A slightly different case arises for the comparison of MOKE and VSM results for the out-of-plane hysteresis loops as in Figure 3-23. A larger discrepancy is noticed in the coercive field scales for the two thickness vs. composition maps. There is a maximum of coercive field of about 5 kOe for the MOKE measurements and a maximum of almost 2 kOe for the VSM measurements. This kind of discrepancy can be seen in the VSM and MOKE hysteresis loop comparison in the bottom left of Figure 3-2. It's been observed that surface oxidation can increase coercive fields of degrading magnetic films which is one possible explanation for the discrepancy [103]. Another explanation is an increased surface energy that can affect the appearance of the loop shape through different switching mechanisms [108]. Further studies using capped films could at least rule out oxidation. At this time, it is unclear whether we are measuring sample aging or a genuine magnetic surface effect.

In addition, very thin samples give essentially no coercive field in the MOKE plot while in the VSM plot, the thinnest samples show the highest coercive fields. This discrepancy can be addressed by observing the MOKE out-of-plane map in the top of Figure 3-23. We see that for the thinnest of samples that the out-of-plane MOKE signal decreases dramatically. A number of causes can account for this including surface oxidation of the 50 nm thick films or perhaps the segregation of vanadium to the surface [109], [110]. Both explanations are possible since the laser beam of the MOKE measurement only penetrates 10 nm into the magnetic film [36]. This study has quantified the discrepancy between MOKE and VSM measurements but more studies are necessary to understand the precise mechanisms underlying the discrepancies. In fact, for in-plane measurements along the easy axis of the film,

trends of magnetic properties are preserved allowing quick screening for regions of interest for further study with the slower VSM technique. Possible further studies to understand the precise mechanisms of the discrepancies between MOKE and VSM will be addressed in future work.
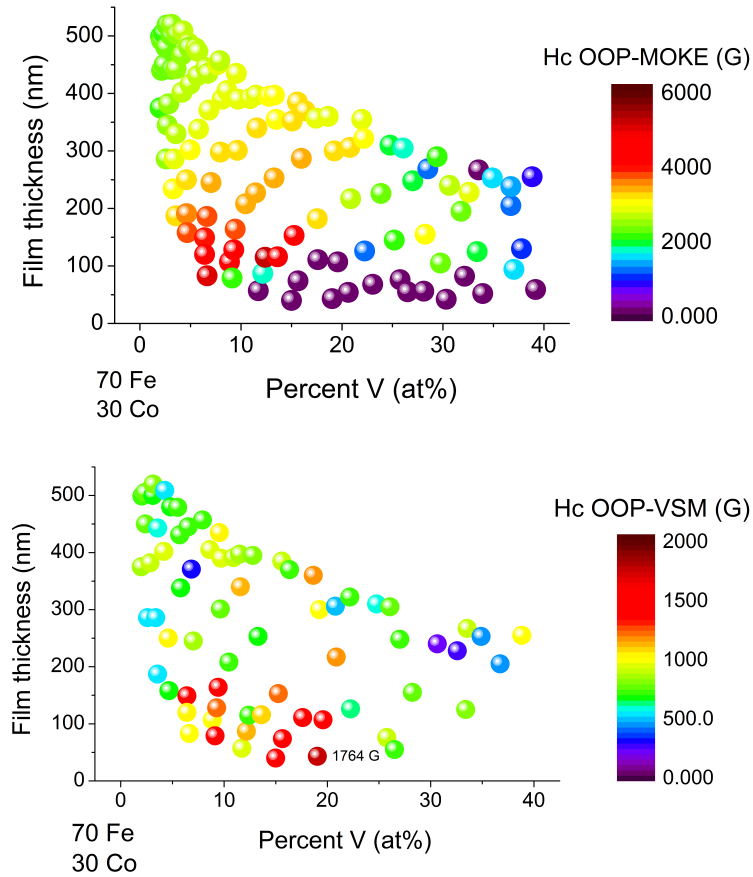
Figure 3-23 Thickness vs. composition map of MOKE out-of-plane coercive fields (top) and thickness vs. composition map of VSM out-of-plane coercive fields (bottom).

Finally, we present some NMF results of X-ray diffraction data plotted on the thickness vs. V composition axes of the thickness dependent library. Information from NMF analysis may provide insight about the relation between structural and

functional properties. The functional dependence of the magnetic properties versus thickness and composition were just discussed above.

NMF is able to find the X-ray spectra associated with pure crystal phases through deconvolution of many different X-ray spectra of different compositions as described in Section 1.5.2. Although the expected number of phases must be input into the program, this is the extent of the user's intuition used. The technique allows the user to dramatically reduce the number of X-ray spectra necessary for close analysis by finding representative spectra for each phase. Thus the technique dramatically decreases the time and effort necessary to identify the pure crystal phases and their quantities present in a combinatorial library. A database of crystal phases is necessary to easily identify known phases and to distinguish new, unknown phases.

Figure 3-24 shows the NMF results using MATLAB and the nnmf function. The number of constituent phases used was 3 as indicated by known phase diagrams. This number of pure phases did indeed give the best results agreeing with known aspects of the system. A bubble pie plot is used to present the data where at each data point a pie chart is used to show the contents of each phase. Red represents the α-phase, green is the γ-phase, and blue is the σ-phase. The bubble pie plot and the component phase diagram, or representative spectra diagram, are color-coded as in Figure 3-24.
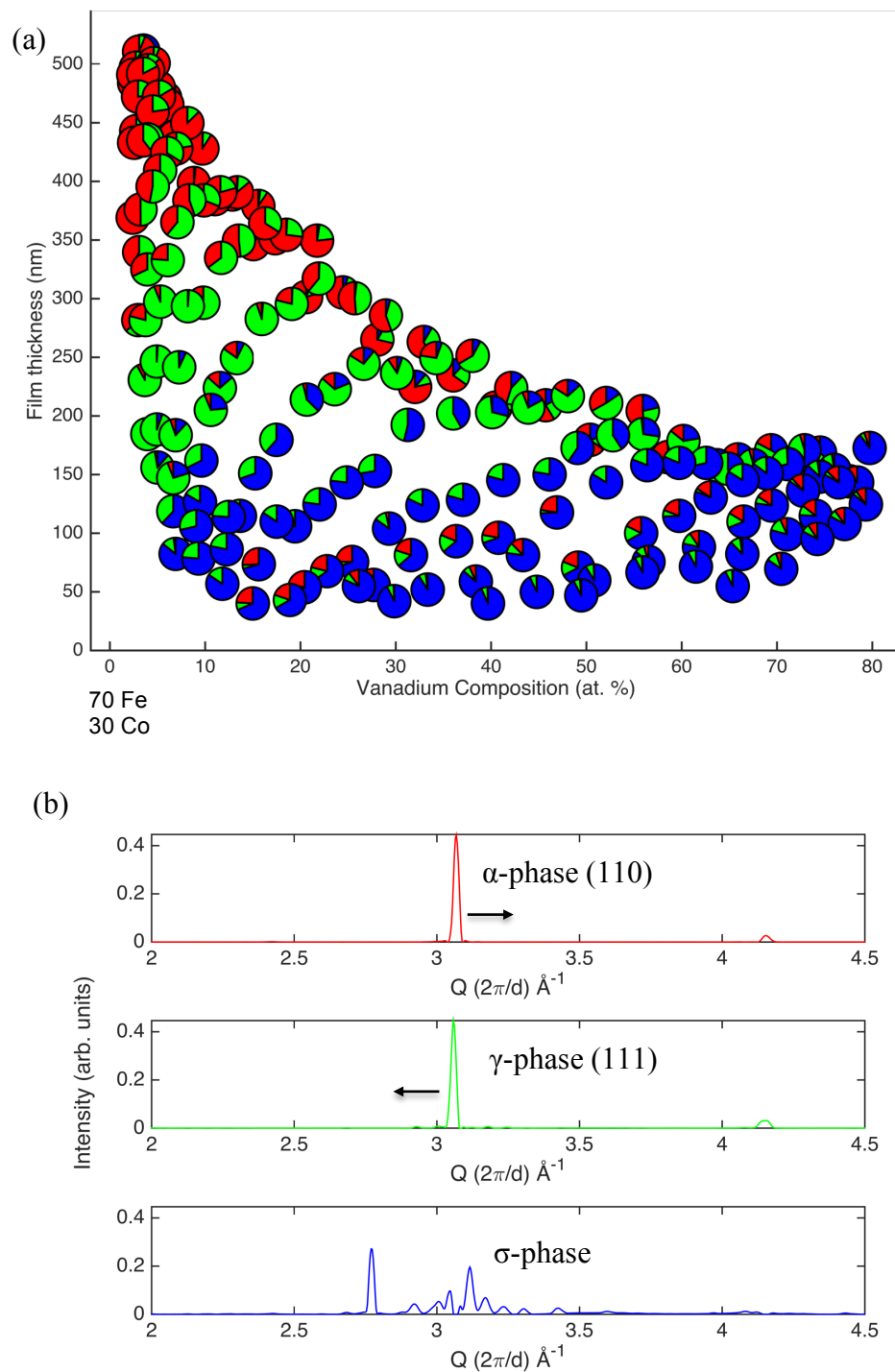
Figure 3-24 Results of non-negative matrix factorization analysis on synchrotron X-ray diffraction spectra of the thickness dependent library. (a) A bubble pie plot showing the weight of each component for each composition point. (b) NMF components. Representative phases are labeled and color-coded with the bubble pie plot where red is the α-phase, green is the γ-phase, and blue is the σ-phase.

One may note that the difference between the α-phase and γ-phase representative spectra is small. In fact the peaks are shifted away from each other as indicated by the arrows in Figure 3-24(b) which agree closely, but not perfectly with the experimental spectra. This is because NMF is indeed an approximation of the experimental data [50].

Background subtraction of the synchrotron X-ray diffraction spectra was carried out in an automated way using batch files in the analysis software "Match!" from Crystal Impact GbR. MATLAB was used to automate the creation of a batch file and data file for each spectra and then send instructions to Match! through the command prompt (or terminal for Mac) for running the batch script. An example script is provided in Appendix A.

Now I discuss aspects of the NMF analysis. Figure 3-24 (a) shows that the thickest films at low V composition (top left) have large fractions of the α-phase (red) with small quantities of the γ-phase (green), as expected. As the vanadium content is increased (going right), we observe that thicker films at the top edge of the plot have an increasing amount of γ-phase (green). When vanadium content increases past about 20 at% V, a small amount of the σ-phase (blue) is introduced as found earlier at this boundary in Figure 3-15, and as expected from literature phase diagrams [7]. For films above about 250 nm, phase quantities are as expected, confirming the accuracy of the NMF technique and the similarities between bulk and our thicker Fe-Co-V thin films.

However, below 250 nm and at low V content, we see that the σ-phase (blue) appears unexpectedly. As film thickness is decreased further in the composition range

below 20 at% V (the expected α-γ-region), we see increasing γ-phase and σ-phase fraction until there is no more α-phase. Below 150 nm the σ-phase is dominant. The α-phase (red) appears again below 75 nm and above 15 at% V. This reappearance seems to correspond to increased coercive fields as observed in the coercive field maps of Figure 3-22 and Figure 3-23. A side-by-side comparison of the structural phase diagram and the functional phase diagram is made in Figure 3-25. A number of effects could be responsible for such a relationship including surface strain, film clamping from the substrate, microstructure, the presence of metastable phases, or some combination thereof. Specific ways of discerning these differences are discussed in future work.

The thickness dependent result has a number of implications for studying permanent magnets using the combinatorial thin film method. First, if bulk properties are expected to be produced, then film thicknesses must be above 300 nm and preferably closer to 500 nm. Although this thickness effect may be well known within the magnetics and thin film community, published confirmation and quantification this thickness dependent effect needs to be discussed openly for the health of the combinatorial thin film and magnetic community. Second, this thickness dependent study verifies that bulk properties can be produced in thin films along their easy axis and we confirm the thickness requirements for such studies. Thirdly, the fact that good agreement of structural/functional boundaries is preserved between the high-throughput MOKE mapping and VSM supports the use of MOKE as a high-throughput technique for permanent magnetic materials in this paradigm of the combinatorial thin film method.
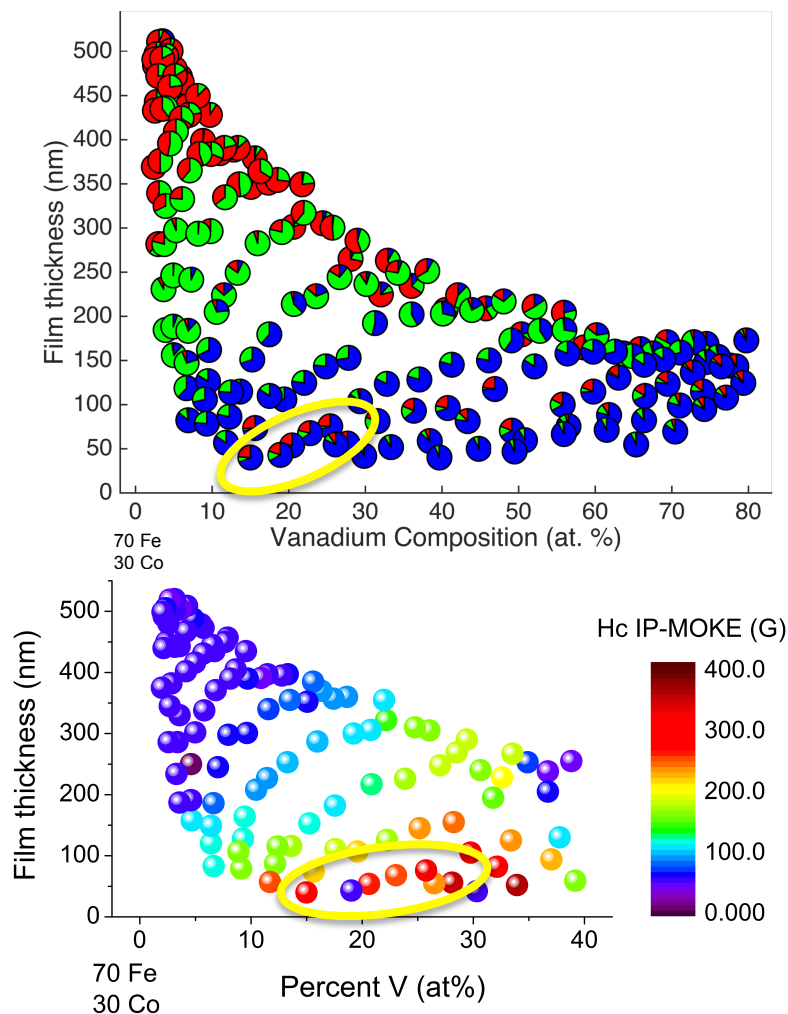
Figure 3-25 A side-by-side comparison of the NMF thickness phase diagram (top) and the coercive field map (bottom). Corresponding points are circled in yellow on both plots showing the agreement between the sudden re-introduction of the α-phase (red) corresponds with the increased coercive fields at films thicknesses near 50 nm and above 15 at% V. Representative phases are labeled and color-coded in Figure 3-24 where red is the α-phase, green is the γ-phase, and blue is the σ-phase.

3.5 Conclusions and Future Work for Part I

We performed combinatorial mapping of composition and thickness gradient Fe-Co-V thin film libraries using high-throughput synchrotron X-ray diffraction, MOKE, and WDS to understand structure, property, and composition relationships in

these permanent magnetic materials. We confirmed that bulk properties of the known Vicalloy permanent magnet are the same as our Vicalloy thin films for the in-plane direction with a coercive field of 300 G and over 800 emu/cm^3 magnetization. We observed an 8 times enhancement of the out-of-plane coercive field which prompted measurement of the angular dependent switching field to understand the result. Angular dependence of switching fields agreed with the Kondorsky model for pinned 180° domain walls over a large vanadium composition range from 0.5 to 24 at% V with equiatomic Fe-Co. This is the first time that quantitative evidence is provided to support that Vicalloy may be a pinning type permanent magnet.

Scanning MOKE measurements were also performed to accelerate the magnetic property screening of composition gradient and thickness gradient libraries. It was found that in-plane MOKE and VSM hysteresis loops agreed for all thicknesses and compositions. In contrast, out-of-plane MOKE and VSM hysteresis loops differed in their coercive fields and loop shapes. Nonetheless, a good agreement of magnetic property trends across most thicknesses and compositions were found for the coercive field in out-of-plane measurements. The scanning MOKE is shown to be capable of identifying trends in magnetic properties in order to identify new regions of interest. This result is supported by the agreement of the trends of magnetic properties with VSM, and the correlation between the structural and functional phase diagram from NMF results.

Non-negative matrix factorization (NMF) of synchrotron X-ray diffraction spectra was used to create the structural phase diagram of the thickness dependent library. The structural phase diagram indicated an unexpectedly large amount of the

σ-phase at compositions usually free of the phase. In particular, regions of thin Vicalloy films under 75 nm showed enhanced coercive fields for in-plane and out-of-plane directions. The feature of enhanced coercive fields was correlated with a feature in the structural phase diagram where the presence of the σ-phase, along with the re-introduction of the α-phase at film thicknesses under 75 nm might be responsible for the enhanced coercive fields. The current study was able to quantify the discrepancies between MOKE and VSM measurements but was not able to unequivocally identify the precise mechanism underlying the phenomenon. This work must be left to future studies described below.

The combinatorial study of the Fe-Co-V system has led to a greater understanding of the switching mechanism for the known permanent magnetic compositions called Vicalloys. Further studies could include confirmation of the proposed 180° pinning mechanism proposed in this thesis. Although Zakharov et al. proposed pinning of an ordered B2 phase on the anti-phase boundaries [5] as in Section 2.7, we proposed a pinning mechanism related to grain size and non-magnetic inclusions of the γ-phase as per the models of [111], [112]. Indeed, it has been recognized that understanding the microstructure, and hence distribution of grains, grain boundary compositions, and secondary phases is increasingly important for engineering magnetic materials[113].

Firstly, to distinguish the switching mechanism from other switching mechanisms such as nucleation type, minor hysteresis loop studies approaching the coercive field could discern the difference between pinning and nucleation type switching [114]. If the magnet saturates its coercive field with minor loops under the

coercive field, then a nucleation mechanism is likely. One approach to quantitatively understand the relation between coercive field and the phase content would be to first measure the distribution and sizes of the phases using dark-field TEM. Since the grains in our Fe-Co-V films appear to be columnar with radius of about 50 nm from the initial cross-sectional TEM images; a planar dark-field TEM image would be useful to discern the grain distribution. The planar imaging should help avoid overlapping grains and hence difficulties in distinguishing the phases since the grains are taller than they are wide. Then the non-magnetic γ-phase can be treated as a magnetic defect where pinning of the magnetic 180° domain wall occurs.

D. I. Paul has developed a simple domain wall pinning model where the size of the magnetic defect and the ratio of the magnetic properties like magnetization, anisotropy constant, and exchange energy between the two phases are considered [112]. This analytical method developed by Paul is useful for some initial analysis, but micromagnetic simulations can consider more complicated effects of stray fields, misaligned grains, and reduced anisotropies [114]. In addition, micromagnetic simulations offer the ability to work in three dimensions compared to most analytical solutions to magnetic pinning restricted to one or two dimensions. With a known phase distribution from dark-field TEM images and some initial numbers for magnetic properties from Paul's model, the application of micromagnetic simulations using OOMMF should offer insight into how to how to improve the permanent magnetic properties through microstructure engineering.

Matching of extrinsic properties with the precise switching mechanism is still difficult to determine and hence a route towards improvement of permanent magnetic

properties. An alternative method would be to use magnetic imaging to directly measure the movement of domain wall motion over magnetic impurities and domain walls. Lorentz microscopy studies of pinning mechanisms at grain boundaries and precipitates in $Fe_{49}Co_{49}V_2$ alloys have been considered previously and were used to show the direct correlation between increased density of grain boundaries and γ-phase precipitates with higher coercive field [115], [116]. Hence, this type of Lorentz microscopy study would be useful in determining pinning mechanisms in Vicalloys where size, and distribution of precipitates could be controlled through thermal processing and composition.

Other than the study of switching mechanisms and the effects of microstructure on magnetic properties, permanent magnetic materials characterization also deserves further attention beyond this dissertation. We showed the high-throughput scanning MOKE to be a reliable method for discovering new regions of interest in permanent magnetic combinatorial libraries, however further work is need to help the permanent magnetic community gain confidence in this technique. For example, further understanding of surface effects could help explain the discrepancy between MOKE and VSM results and thereby help reduce these effects or at least explain their occurrence.

A number of high-resolution techniques like electron energy loss spectroscopy (EELS), energy-dispersive X-ray spectroscopy (EDS), and selected area electron diffraction (SAED) offer ways to locally measure composition and crystal structure down to nanometers. In order to observe subtle changes at the surface of our Fe-Co-V films EELS can be used to measure the oxidation state of Fe and Co. Using a line

scan, the depth of oxidation could be measured precisely and compared to the penetration depth of the MOKE which is about 10 nm as discussed in Section 1.4.4. Through the use of a capping layer, surface oxidation can be largely eliminated. In addition, EELS can help determine elemental segregation at the surface. Vanadium is known to segregate at the surface, which could cause the change in coercive field measured when comparing MOKE and VSM [109], [110], [117].

Increasing the reliability of high-throughput MOKE benefits the whole magnetic community by avoiding unnecessary measurement with the traditional slow magnetometry methods like VSM. Indeed, a multitude of unstudied candidates for permanent magnets awaits screening using combinatorial high-throughput methods [102]. In addition, if quantitative and non-destructive magnetometry techniques such as scanning Hall probes could be made more affordable and more robust, the magnetism community would also benefit greatly.

The advantages of Vicalloy since its discovery have been its relatively high remanent induction, its high curie temperature, and its machinability for applications. If these advantages could be realized with an improved pinning mechanism to increase coercive field through further alloying, microstructure, or nanostructure engineering, we believe an improved permanent magnetic material could result. Although the cost of V has had it's own changes in price, most recently in 2008, the changes are nowhere like those of the rare-earth elements. Market fluctuations will always be a materials issue but by finding more alternatives, we protect ourselves from relying on only one resource.

Part II

Multiferroic Heterostructure of

Transcritical Permalloy on Barium Titanate

Chapter 4. Introduction to Composite Multiferroic Materials

In this chapter we start by reviewing the literature on single-phase and composite multiferroics. Next the basic theoretical description of the principles of composite multiferroics and the corresponding physical phenomenon of magnetostriction are explained. The important properties and characteristics of magnetic stripe domains used in the study are reviewed and finally, a brief explanation of the archetypal ferroelectric, barium titanate, and piezo-response force microscopy data, is covered. This background literature is to prepare the reader for the following chapter on the study of a heterostructure of transcritical Permalloy thin film on top of $BaTiO_3$.

4.1 Introduction to Multiferroics

A multiferroic material has at least two or more ferroic orders (ferromagnetic, ferroelectric, ferroelastic) interacting simultaneously. The possible combinations for different ferroic coupling are shown in Figure 4-1, where the various pathways to control each ferroic order parameter is pictured. Multiferroics were first proposed by Jean-Pierre Curie in 1894 based on symmetry considerations of the crystal structures required for such a material [118]. Some of the first experimental observations of multiferroics were in the 1960's where crystals of Nickel-Iodine Boracite showed a hysteretic behavior of voltage with applied magnetic field [119]. However, the effect in this and most other single-phase multiferroics requires cryogenic temperatures and large magnetic fields (Tesla) or electric fields (kV). We will call these types of multiferroics single phase because they are formed in a single crystal phase, as oppose to the composites discussed later.
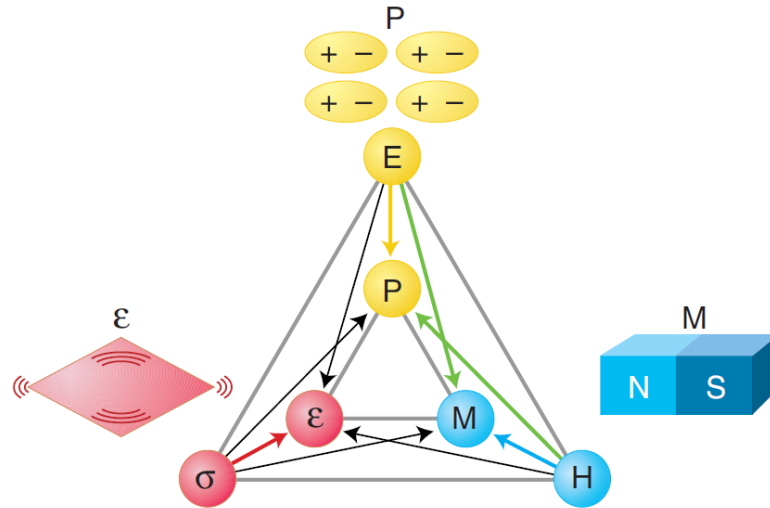
Figure 4-1 The connection between the electric (E), magnetic (H), and stress (σ) fields and their respective parameters of polarization (P), magnetization (M), and strain (ε). A multiferroic requires at least two of the ferroic orders which leads to interactions between them. For example, in a magnetoelectric multiferroic, the magnetic field may control electric polarization P, or the electric field may control magnetization M (green arrows). Borrowed from[120].

Other seminal findings in single-phase multiferroics include Dzyaloshinskii's prediction of Cr_2O_3 and the discovery of that material's properties the following year in 1960 by Astrov [121]. Unfortunately the magnetoelectric properties were observed to disappear just above 300 °K and the material was paraelectric and antiferromagnetic. This combination of Curie temperature and magnetic and electric ordering makes Cr_2O_3 impractical for device applications.

One of the most promising single phase multiferroics became of interest in the 1950's in then, Soviet Union, $BiFeO_3$ (BFO). BFO is one of the few strong room temperature ferroelectrics and simultaneously magnetic multiferroics, which made it of interest for applications. Original work to synthesize ceramics of BFO were

unsuccessful because of leakiness from parasitic reactions causing oxygen vacancies which increased conduction [121], [122]. In 2003, a surprising finding showed that epitaxial thin films of BFO had 15 times larger remnant electric polarization than the previously known bulk values [123]. The finding stimulated much work in the area of multiferroics, opening the doors for devices and applications previously not possible.

Unfortunately BFO is the only shining star in the world of single-phase multiferroics. But, a resurgence in the interest of magnetoelectrics, as shown by Figure 4-2, has led to a number of interesting physics and engineering feats including the new finding of ferroelectricity induced by spiral spin order [124] and a lead-free ferroelectric [125].
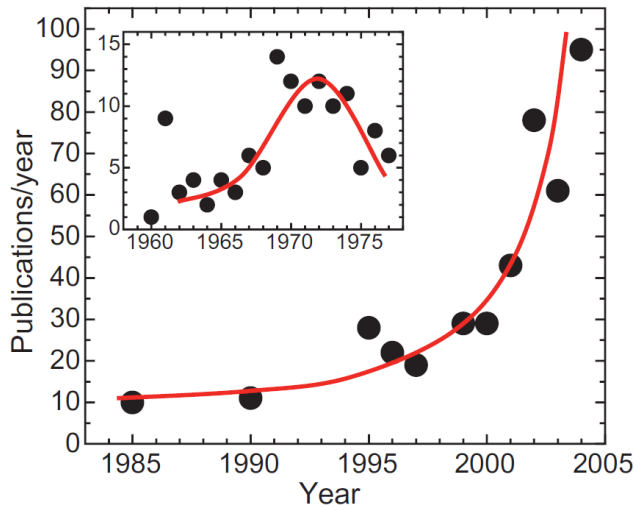
Figure 4-2 The number of publication with the keyword "magnetoelectric" showing a spike in activity in the seventies and the current resurgence of interest in the 2000's [126].

4.2 Strain-Mediated Multiferroic Heterostructures

The onset of high-quality bulk and thin film materials in the 1990's opened a new paradigm for artificially produced composite multiferroics. These composite multiferroics boasted orders of magnitude larger multiferroic effects and room-temperature operation [127]. The ability to (1) choose the ferroic materials separately, and (2) operate at room temperature, are the major motivations to study composite multiferroics. Composite multiferroics can operate under a number of regimes including strain-mediated, charge-mediated, and other exotic spin-orbit effects [128].

Studies have sought to explore the exact cross-over for where different regimes dominate. One such study used Ni thin films of different thicknesses on a $BaTiO_3$ substrate to understand where strain-mediated and charge-mediated regimes would dominate [129]. The authors found that at thicknesses below about 10 nm, a Ni film begins to change from the expected butterfly curve of a magnetoelectric and display a more linear dependence of magnetization with electric field, indicating a charge dependent mechanism. Magnetoelectric simply means that a material can induce an electric (magnetic) polarization with an applied magnetic (electric) field. Figure 4-3 shows Shu et al.'s results where the only difference between the two samples is a Au interlayer which is supposedly screening charges that are responsible for the interface charge-mediated mechanism present in the left figure.
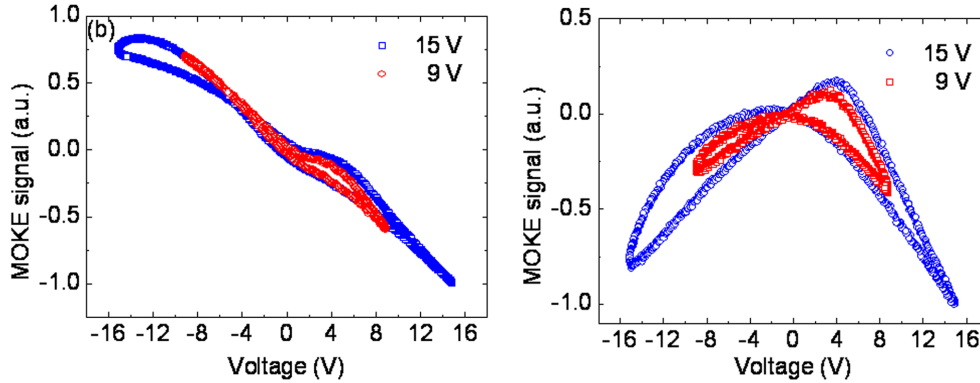
Figure 4-3 Voltage modulation of the magneto-optic Kerr signals for a 10 nm-Ni/BaTiO$_3$ heterostructure on the left and a 10 nm-Ni/8 nm-Au/BaTiO$_3$ heterostructure on the right. The authors argue that the Au interlayer in the sample on the right has screened the charges at the Ni/BaTiO$_3$ surface thereby only transferring strain and making the magnetoelastic contribution dominant and not the interface charge mediated mechanism as in the left [129].

We focus on the relatively well-understood strain-mediated regime where simple elastic coupling between film and substrate provides the basis of the effect. The strain controlled magnetic properties of thin films is widely investigated for future applications in random access memories [12], [130], sensors [131] and transducers [132]. Such devices for controlling magnetic domains and magnetization direction are typically made of magnetostrictive films in intimate contact with piezoelectric materials. In this thesis we take piezoelectric and ferroelectric materials to be synonymous. The effect of electric-field induced strains on these devices is usually studied by monitoring changes in macroscopic properties such as magnetic hysteresis loops [133]–[136].

In another study of a Ni/BaTiO$_3$ heterostructure, changes in the coercive field and remanent magnetization were observed at different applied electric fields [135]. Figure 4-4 shows the magnetic hysteresis loops at two different scales for applied

132

field to highlight the fact that the total saturation magnetization is not changing, simply the remanent magnetization. Other researchers showed a similar effect for a $Ni_{80}Fe_{20}/BaTiO_3$ heterostructure but they claimed the saturation magnetization of the $Ni_{80}Fe_{20}$ film was being changed [133]. We propose that the field for saturation was simply not reached in their study. For comparison, the $Ni/BaTiO_3$ study went to over 2,000 Oe to reach saturation while fields only to 75 Oe were used in the $Ni_{80}Fe_{20}/BaTiO_3$ study. Thus, careful consideration must be taken when studying macroscopic properties of magnetoelectrics.
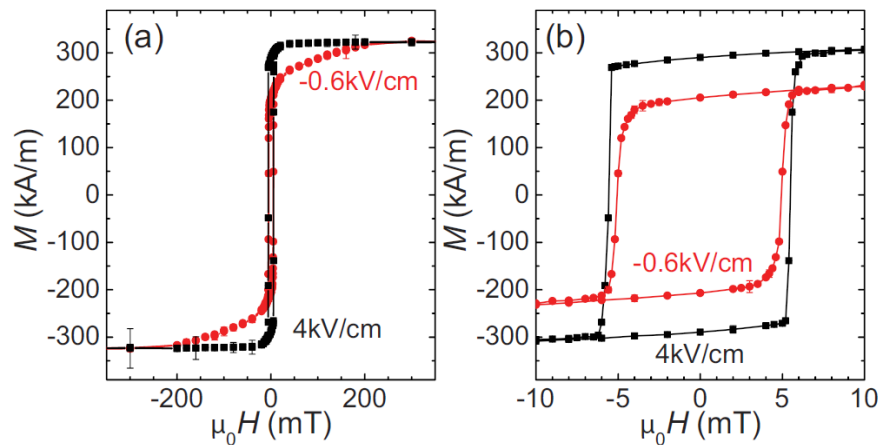
Figure 4-4 Both (a) and (b) show in-plane magnetic hysteresis loops of the $Ni/BaTiO_3$ heterostructure for different applied fields across the $BaTiO_3$ substrate. Different field scales between (a) and (b) highlight the changes in remanent, not total magnetization [135].

Considerable work has been done on heterostructures of a ferromagnet and $BaTiO_3$ including work with phase transitions of the latter [137], [138]. Sahoo et al. found that the magnetization of an $Fe/BaTiO_3$ heterostructure varies with temperature in coincidence with $BaTiO_3$'s phase transitions. Figure 4-5 shows the 10 nm

polycrystalline Fe film has distinct transitions, or changes of in-plane and out-of-plane magnetization, at each of the structural transitions of $BaTiO_3$. This study suggests that strain between the film and substrate during a phase transition is capable of changing the magnetization direction and coercive field significantly. This point is of particular interest for this dissertation where we use $BaTiO_3$'s phase transition to induce changes in a Permalloy film top.
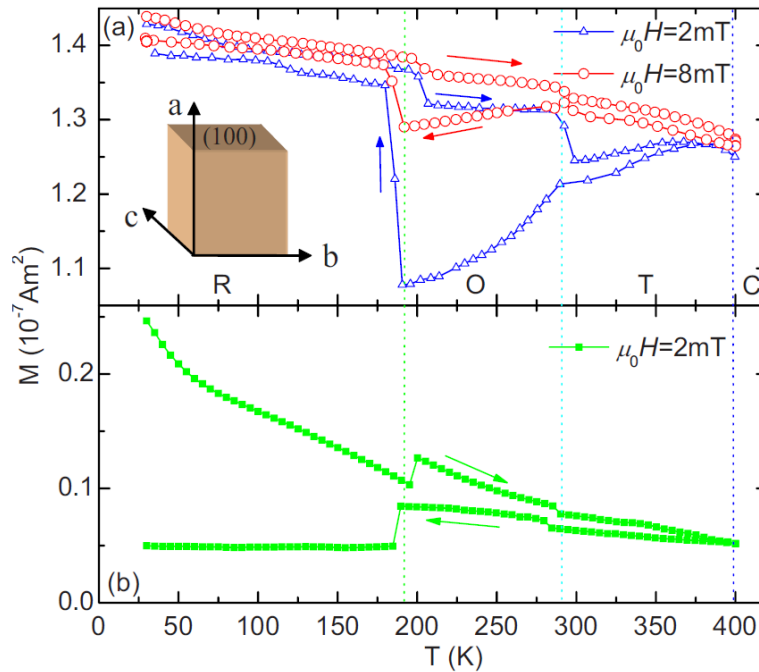
Figure 4-5 (a) In-plane magnetization of the Fe film, M, varying with temperature, T. Arrows point in the direction for temperature scans. Letters R, O, T, and C denote the rhombohedral, orthorhombic, tetragonal, and cubic states of $BaTiO_3$ single-crystal substrate, respectively. Dotted lines are the boundaries between respective structural phase transitions. The inset depicts a representative $BaTiO_3$ unit cell with reference axes. (b) Out-of-plane M vs T curve. Figure from [137].

There are, however, only a handful of studies investigating the local microscopic interactions of ferroelectric and ferromagnetic domains [139]–[144]. One study used polarized microscopy to observe local coupling of ferroelectric and

ferromagnetic domains for a 15 nm CoFe film on $BaTiO_3$ with applied electric fields [139], [140]. The results shown in Figure 4-6 show differences between as-deposited and applied electric-field states of the ferroelectric and ferromagnetic domains. The 15 nm $Co_{60}Fe_{40}$ film was deposited at room temperature by e-beam evaporation.
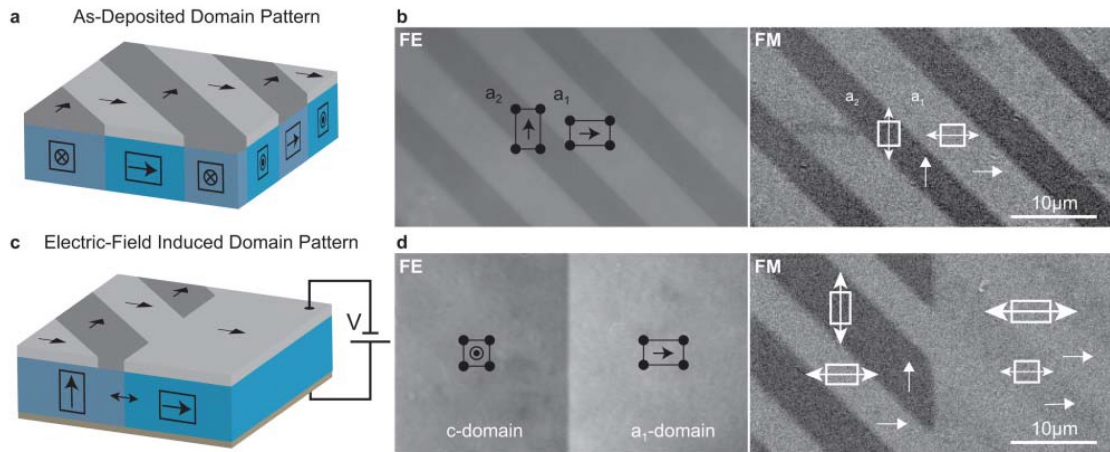
Figure 4-6 (a) Schematic of the as-deposited ferromagnetic CoFe film (grey) and ferroelectric $BaTiO_3$ (blue) microstructure. (b) Shows the optical polarization microscopy images of the as-deposited state where black rectangles and arrows show the lattice elongation and the polarization direction of the $BaTiO_3$ substrate. White rectangles and double –headed arrows show the orientation of the strain induced magnetic easy axis of the ferromagnetic film. (c) Schematic of the microstructure after the application of an out-of-plane electric field of 10 kV/cm. (d) Corresponding polarization microscopy images of the electric field induced domain pattern [140].

In the as-deposited state the ferromagnetic domains followed the pattern of ferroelectric domains showing a regular ferroelectric a_1 and a_2 pattern where the ferroelectric polarizations are pointed in two different in-plane directions. After applying an electric field of 10 kV/cm the ferroelectric domain pattern changed to a ferroelectric a-c-domain pattern where the ferroelectric domains point in-plane and out-of-plane, respectively. C-domains present a square lattice face to the crystal

surface so the authors argue that is why the ferromagnetic pattern now over the ferroelectric c-domain was preserved, as in Figure 4-6(d). The ferromagnetic domains over the now larger ferroelectric a-domain were all switched to point along the a-domain polarization direction, which has an associated strain. This study showed the clear local pattern-matching abilities of ferromagnetic/BaTiO$_3$ heterostructures and that strain could deterministically decide the local ferromagnetic domain patterns. Optical methods are, however, not the only way to observe such local coupling in multiferroic heterostructures.
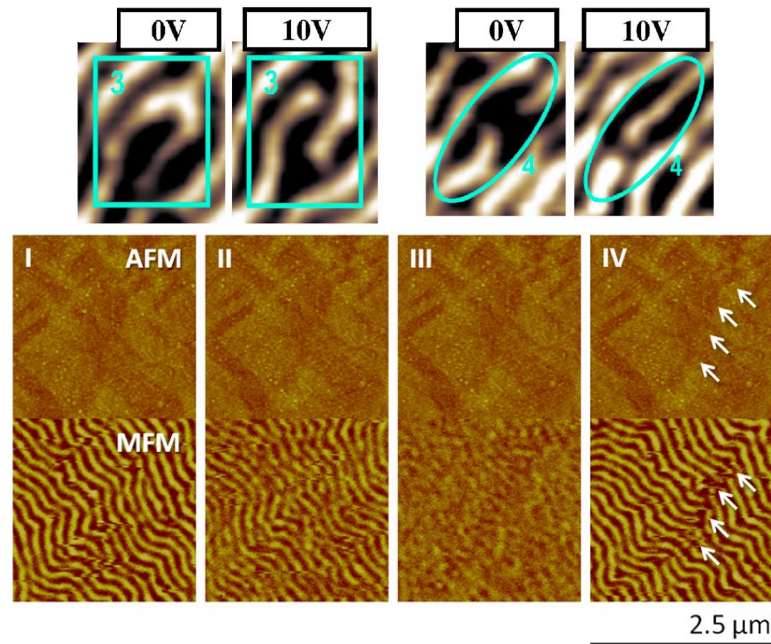
Figure 4-7 The top shows Chung et al.'s work displaying the branching, and elongation type alterations observed in the thinfilm Ni/PZT device[141]. The bottom shows Hsu et al.'s work where AFM and MFM images are presented for different applied electric fields where (I) 0 MV/m, (II) 0.4 MV/m, (III) 0.8 MV/m, and (IV) 0 MV/m [145].

Scanning probe microscopy was also used to show local changes in magnetic stripe domains of an all-thin-film Ni/PZT device[141] and in a Ni/PMN-PT heterostructure [145]. In the first study, Chung et al. found that magnetic stripe domains in their 100 nm Ni film had reversible curving, bending, branching, and elongation under an electric field. The study used magnetic force microscopy (MFM) to observe these very local changes shown in the top of Figure 4-7. In the other study by Carman's group, Hsu et al. found that magnetic stripe domains in their 60 nm Ni film reversibley disappeared from an in-plane isotropic compressive strain from the PMN-PT (001) substrate with applied electric field. The result is shown in the bottom of Figure 4-7 where increasing electric field eliminates the stripe domains and thereby reversibly changing the out-of-plane magnetization.

In addition, scanning electron microscopy with polarization analysis [146] (SEMPA) proved to be a useful tool for the local characterization of multiferroic heterostructures. Advantages include the simultaneous imaging of ferromagnetic domains using SEMPA and the imaging of ferroelectric domains use the backscattered electron (BSE) image. The resolution of this technique is also very high where SEMPA images can approach 2 nm resolution of magnetic features and also 3-D spin information is also possible to gather. Hence, SEMPA offers the resolution of SPM techniques but with quantitative capacity and simultaneous ferroelectric imaging. Disadvantages include the required vacuum environment of the scanning electron microscope, the inability to apply large magnetic fields which will compromise the electron beam, and the small penetration depth of the SEMPA measurement at only 5 nm.

4.3 Introduction to Theory of Strain-Mediated Multiferroics

Strain-mediated multiferroics are composite materials with separate magnetostrictive and piezoelectric parts which when mechanically coupled together, gives them multiferroic properties. A magnetostrictive material can change the magnetic moment directions with an applied strain. We can consider this a mechanical/magnetic effect. In a piezoelectric material a voltage can produce a mechanical strain. We can consider this an electric/mechanical effect. Separately, these materials are not multiferroic, however with mechanical coupling, the composite has extraordinary multiferroic coupling. This effect is described by a product tensor property where it's the product of the magnetostrictive and the piezoelectric effects as noted below [127].

$$Converse\ ME\ effect = \frac{electric}{mechanical} \times \frac{mechanical}{magnetic}.$$

The converse magnetoelectric effect is such that when an electric field is applied, the piezoelectric phase changes its shape piezoelectrically. The strain is then passed along to the magnetostrictive phase resulting in an altered magnetization as per magnetostriction discussed in the next section. This formulation was originally proposed by van Suchtelen [147] in 1972 where the we can describe the piezomagnetic and piezoelectric coefficients of such a converse magnetoelectric as:

$$\frac{\partial S}{\partial H} = e^m$$

for the piezomagnetic phase, and

$$\frac{\partial P}{\partial S} = e$$

for the piezoelectric phase, where S is the strain and e^m and e are the piezomagnetic and piezoelectric coefficients, respectively. We can then characterize the two-phase composite material by

$$\frac{\partial P}{\partial H} = \alpha = k_c e^m e,$$

where k_c is a coupling factor such that, $0 \leq |k_c| \leq 1$, and α is the magnetoelectric coefficient of the composite. We see that a new property of the magnetoelectric coefficient appears in the composite consisting of both magnetic and piezoelectric phases even though neither singular phase is magnetoelectric. This type of elastically coupled composite multiferroic favors a high piezomagnetic (magnetostrictive) and piezoelectric coefficients and a strong coupling factor k_c for a large magnetoelectric coefficient.

Additional models have been formulated to gain detailed microscopic understanding of various phenomena in magnetoelectrics. For example, ab-initio models were used to understand the temperature dependence of magnetization for FeCo and Ni/BaTiO$_3$ heterostructures [148]. A two-region model was used to gain understanding of the converse magnetoelectric effect for an Fe$_3$O$_4$/BaTiO$_3$ heterostructure [149]. Finally, phase field models were used to understand real-space, time-dependent local elastic interactions of the previously mentioned Co$_{60}$Fe$_{40}$/BaTiO$_3$ system[150]. We show in Figure 4-8 an example of the phase field modeling of the magnetic (top) and ferroelectric (bottom) domain structures at one point in the sweeping of electric field.
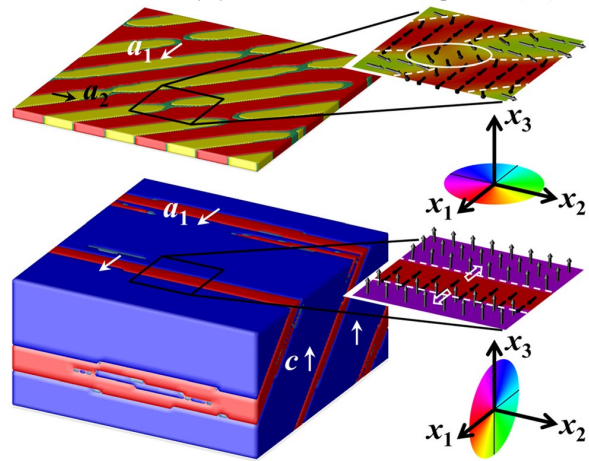
Figure 4-8 Phase field simulation of an example $Co_{60}Fe_{40}/BaTiO_3$ system where the magnetic domain structure is on top and the ferroelectric domain structure is on the bottom. Ferromagnetic domain directions a_1 and a_2 are from a previous configuration of the ferroelectric substrate. The above figure is as the electric field is lowered from a saturated state with a single c-domain state and the red a-domains begin to appear. White arrows indicate polarization directions of the magnetic and ferroelectric phases. On the right, close-up vector plots of the magnetization and polarization are shown. Dashed white lines indicate the domain boundary while arrows indicate the direction of boundary movement. The white solid circle in the top right indicates the region undergoing magnetization rotation. The color wheels with axes directions indicate the crystalline orientation of the magnetic and ferroelectric regions. Figure from [150].

4.4 Magnetostriction and Stress Induced Anisotropy

In this section we give a very brief introduction to magnetostriction and present the basic equations to describe magnetostriction induced anisotropy for use in the following chapter. Magnetostriction is the property of a material to change shape under a magnetic field or conversely, change the direction of magnetic moments when under a stress. James Joule first observed this strain induced by a magnetic field in 1842 when he saw that an iron sample changed its length when magnetized. The magnetostrictive strain is defined as $\lambda = \Delta l/l$, where l is the unmagnetized length and Δl is the change in length after the material is magnetized. We are interested in

the converse effect where strain is used to control the direction of magnetic moments. In this case, the stress is said to induce a magnetic anisotropy energy K that's proportional to the magnetostrictive constant, λ, and the stress, σ, such that

$$K = -\frac{3}{2}\lambda\,\sigma.$$

The magnetostrictive constant is a strain usually measured in parts per million (ppm) because of the small size of the effect. The stress takes into account the Young's modulus (Y) of the material, the strain ε, and the Poisson's ratio, ν, such that

$$\sigma = Y\varepsilon/(1 - v^2).$$

The stress induced anisotropy energy, K, from magnetostriction is uniaxial meaning that the magnetic moments like to point parallel or antiparallel with the axis of anisotropy. Depending on the sign of λ, the anisotropy direction can be parallel to the strain direction (positive magnetostriction) or can be perpendicular to the strain direction (negative magnetostriction). To get a better understanding of this we present some magnetic hysteresis loops of Permalloy thin films [151] under different strains in Figure 4-9. For a positive magnetostriction like the top of Figure 4-9, a tensile stress induces an easy axis and a compressive strain induces a hard axis behavior. For a negative magnetostrictive material like the bottom of Figure 4-9, a compressive stress induces the easy axis, while under a tensile stress we find a hard magnetic axis. This shows how dramatically the stress induced anisotropy can affect the magnetic properties and how small composition changes can dramatically effect magnetostrictive behavior. Permalloy is known to be particularly sensitive to strain and composition.
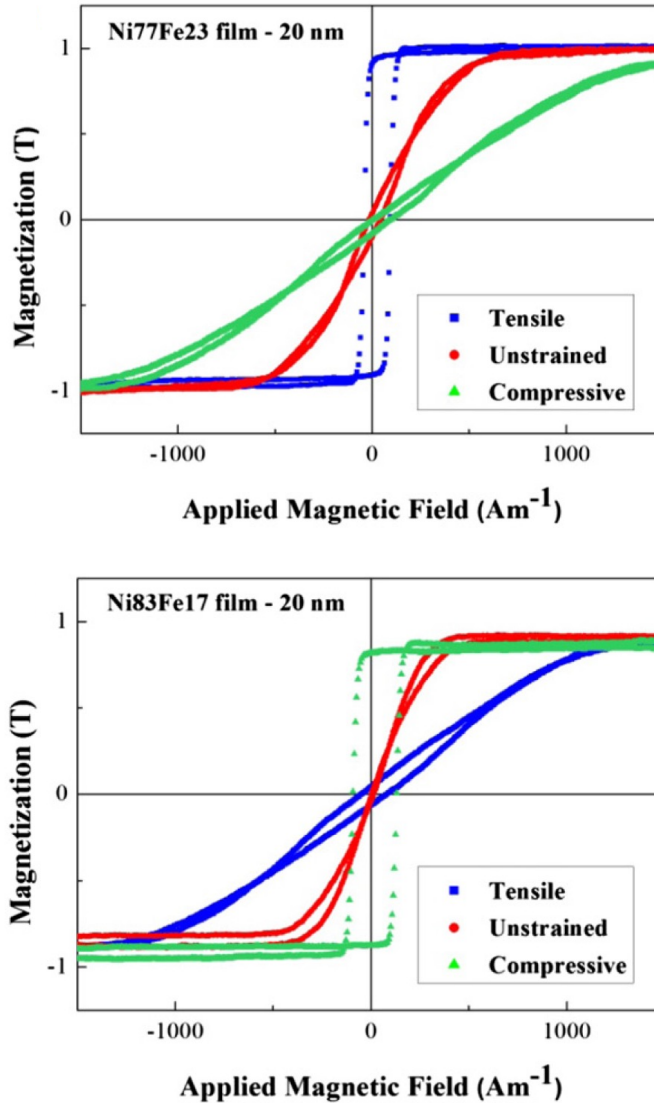
Figure 4-9 Magnetic hysteresis loops for unstrained conditions and with equal applied stress for a positive magnetostrictive thin film of $Ni_{77}Fe_{23}$ (top), and a negative magnetostrictive thin film of $Ni_{83}Fe_{17}$ (bottom). Figure from [151].

4.5 Magnetic Force Microscopy and Piezo-response Force Microscopy

Here we discuss the operation of the important scanning probe microscopy (SPM) techniques used in this study. Both techniques operate chiefly through the use of a cantilever which can be thought of as a flexible mirror with a spike sticking out of one side which is collectively referred to as the tip. As the tip is dragged across the

surface of a sample, the spike encounters objects. Changes in the height of the mirror

are measured by reflecting a laser beam off the top of the tip and into a position

detector or photodiode as depicted in Figure 4-10.

Magnetic force microscopy (MFM) makes use of a magnetic tip operating in

non-contact mode meaning that the tip is lifted at a fixed height away from the

sample surface. This is achieved by first scanning the sample surface in contact mode,

recording the height variation and then following this height variation at a fixed

distance from the sample surface in the so-called interleave mode. Because the

magnetic tip is attracted to or repulsed by a magnetic sample, a force is felt by the tip

and corresponding variations in the tip are measured, thereby giving contrast in the

MFM image.
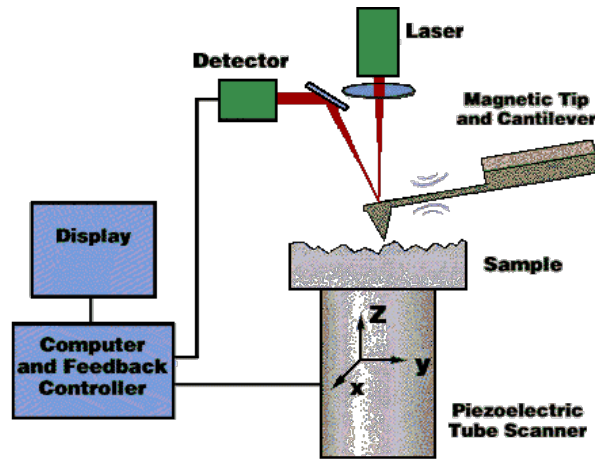
Figure 4-10 Schematic of a scanning probe microscope with major components
labelled. From http://www.engr.sjsu.edu/WofMatE/Mat'sChar2.htm.

In piezo-response force microscopy (PFM) a metallic tip is used in order to be

able to apply a voltage to a piezoelectric sample. Because piezoelectrics respond to an

electric field by deforming, small height variations are detected as an alternating voltage is applied to the tip and through the sample. In all SPM techniques the tip moves in a raster motion across the sample surface with a steady back and forth motion progressing along incrementally with each pass. The raster motion allows the formation of an image through many scans.

In PFM, a distinction can made between torsional forces on the tip which indicate lateral motions of the sample surface, and deflection forces on the tip which indicate vertical motion of the sample surface. These two types of motion can be imaged simultaneously and are called lateral PFM and vertical PFM. As Figure 4-11 indicates, these two types of motions are associated with ferroelectric domains where lateral PFM is associated with ferroelectric a-domains and vertical PFM is associated with ferroelectric c-domains. This point will become important when we confirm the strain directions of the different a-domains present in our $BaTiO_3$ substrates in Section 4.7.
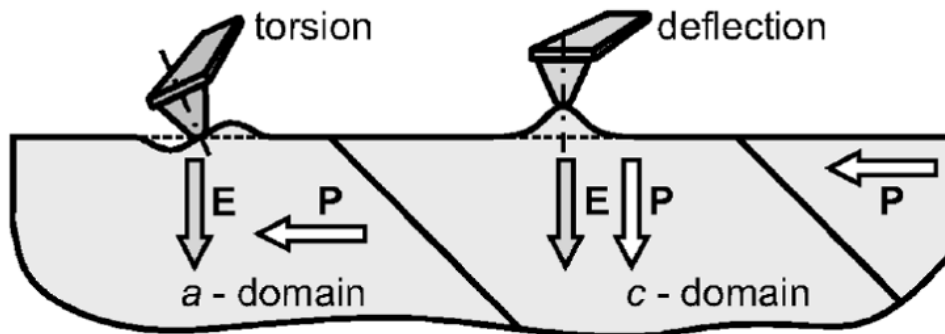
Figure 4-11 Schematic explaining contrast formation in PFM. The applied electric field E, causes surface displacements due to the converse piezoelectric effect. P represents the ferroelectric polarization direction. Figure from [152].

144

4.6 Magnetic Stripe Domains in Permalloy Films

We use magnetic stripe domains as an easy way to observe local average in-plane magnetization direction of our multiferroic heterostructure using MFM. Magnetic stripe domains (MSDs), like those depicted in Figure 4-12(c) and Figure 4-14(a), give accurate information about the magnetization direction which can be used to track changes in magnetic anisotropy, both in-plane and out-of-plane. Since the 1960s, transcritical Permalloy thin films (tPy) have been studied because of their dense MSDs which are sensitive to strain [153], thickness [154], and magnetic anisotropy energy [155], [156]. They are called transcritical because MSDs form only above a critical thickness. In applications, the stripe domains were actually avoided because of their increased coercive fields which would hamper the soft magnetic properties if high susceptibility films were desired. The MSDs are said to arise from a weak out-of-plane magnetic anisotropy [154], [155], [157]–[160] which will be discussed later. We now present our results on a thickness dependent study of tPy films to find the value of our critical thickness.

The critical thickness is important for the present study of the tPy/BaTiO$_3$ heterostructure because if the film is too thick the film will not couple mechanically with the substrate and so the heterostructure won't have a large coupling factor k_c and will not show magnetoelectric properties. Permalloy films were grown at different thicknesses of 205, 135, 95, and 65 nm using an Ar pressure of 15 mTorr (20 mbar). MFM images and hysteresis loops were taken for each thickness and are displayed in Figure 4-12. From thickest on the left to thinnest on the right, the MFM images go through a clear progression of labyrinth domains, stripe domains, and no stripe

domains for the last two images. The in-plane hysteresis loops also go through a progression of having the characteristic transcritical hysteresis loop shape with the linear segment before saturation for the two thicker films, and then back to standard easy-axis loops for the thinner two films. The critical thickness is then easily found as 115 ± 20 nm and visualized by plotting the coercive field of the hysteresis loops versus film thickness as in Figure 4-13. The plot agrees nicely with a similar plot from Svalov et al.'s work [160].
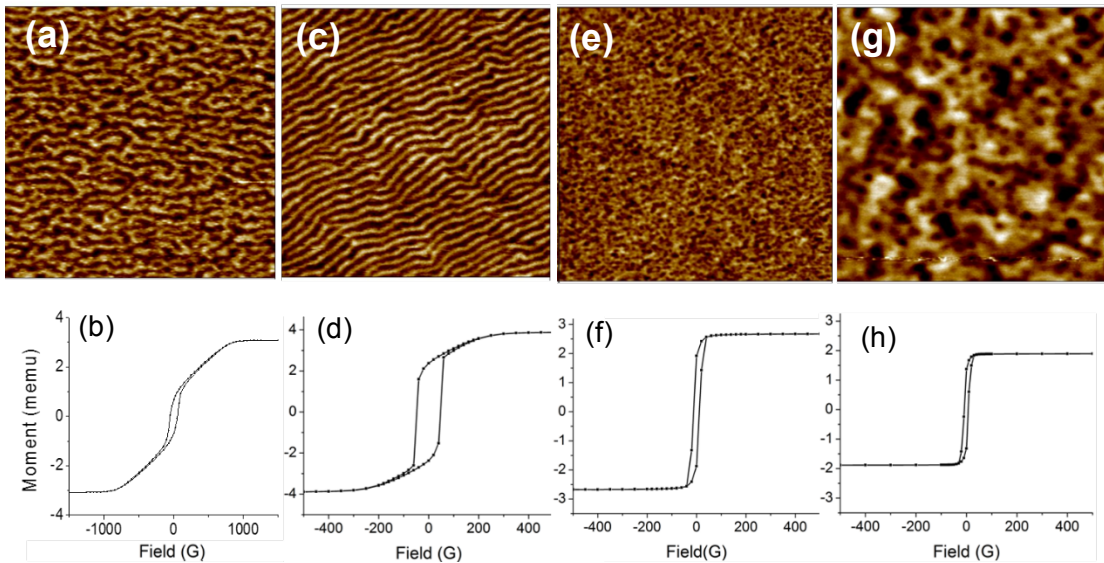
Figure 4-12 Progression of MFM images on top and in-plane magnetic hysteresis loops on the bottom for different thicknesses of Permalloy films from (a-b) 205 nm thick, (c-d) 135 nm, (e-f) 95 nm, and (g-h) 65 nm. Widths of the MFM images are 5 μm except for image (g), which is 2 μm.

Next, we want to understand the origin of the magnetic properties in the tPy films. Figure 4-14(b) shows a cross-sectional scanning electron micrograph of a tPy film [159]. The columnar microstructure in the tPy can be clearly seen which may contribute to the out-of-plane magnetic anisotropy through shape anisotropy. The

competition between shape anisotropy, out-of-plane magnetic anisotropy, magnetostatic, and magnetic exchange energies in the tPy results in the alternating up and down magnetic moments giving the strong contrast in MFM images as in Figure 4-14(a) [161].
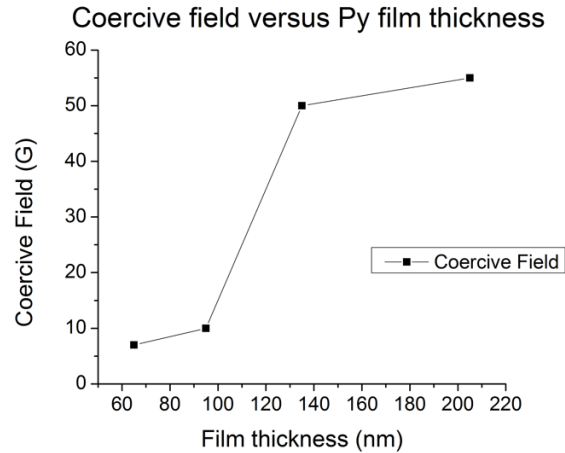
Figure 4-13 coercive fields from the above hysteresis loops versus their respective film thicknesses.

There is, however, still a large in-plane component to the magnetization taken as the direction of the stripe domain lines. Figure 4-14(c) shows the in-plane magnetic hysteresis loop of tPy where at low fields a sharp switching occurs and at higher fields a linear slope is present until saturation [160]. The remnant value of the in-plane hysteresis loop indicates that there is still a large in-plane component of the magnetization lying along the direction of the stripes despite the alternating out-of-plane magnetization components [157], [161]–[163]. The fact that the magnetization points along the MSD direction was also confirmed by MFM images showing that the magnetic stripe domains align along the direction of an applied magnetic field.
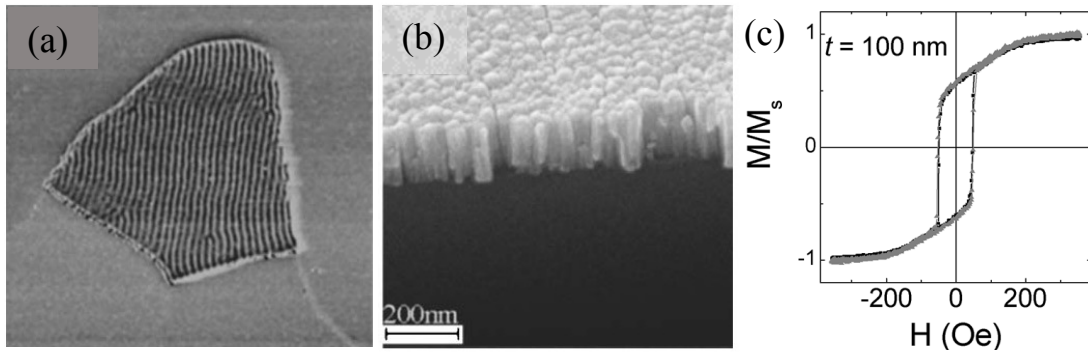
Figure 4-14 (a) 20um^2 AFM/MFM images of Permalloy patches. (b) SEM cross-sectional imaging of sputter-deposited Permalloy thin film from [159]. (c) Transcritical Permalloy in-plane magnetic hysteresis loop. "t" is film thickness from [160].
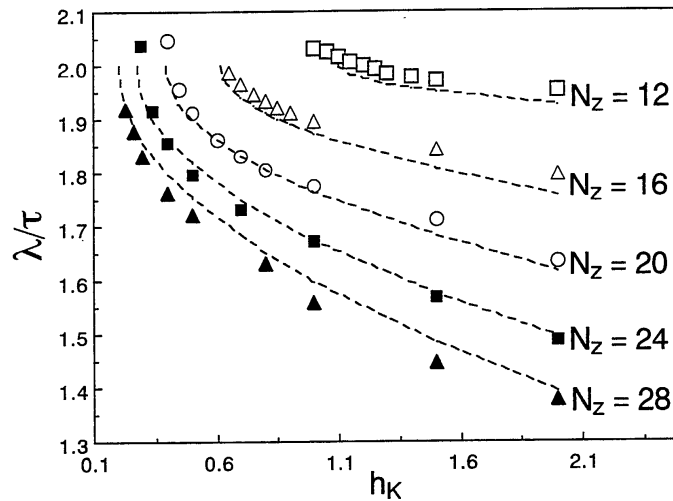
Figure 4-15 Stripe wavelength, λ, normalized by film thickness, τ, vs. the scaled out-of-plane anisotropy energy, h_K, for a number of different film thicknesses, N_Z. Figure from [156].

Numerical and semi-analytical solutions have been formulated to model the behavior of magnetic stripe domains for their critical thickness and stripe width dependence on thin film thickness and anisotropy energy. Figure 4-15 presents the work of Pant et al. [156] who pointed out that stripe domain period should increase as

out-of-plane anisotropy energy is lowered. This trend was also suggested by Murayama et al., from his description of critical thickness [155]. Based on this we expect the stripe domains with larger period to have less out-of-plane magnetic anisotropy energy.

4.7 Ferroelectric BaTiO$_3$

Now we discuss the substrate of our multiferroic heterostructure that provides the necessary strain for the strain-mediated multiferroic. BaTiO$_3$ is a well-studied ferroelectric material where at room temperature a spontaneous electric dipole points along the tetragonal distorted length of the unit cell. BaTiO$_3$ is synonymously considered a piezoelectric material because if an electric field is applied then a strain is induced. Conversely, if a stress is on the crystal, a voltage across the sample is induced. Because of the tetragonal symmetry of the unit cell, there are six possible directions for the electric polarization and only three for the spontaneous strain. BaTiO$_3$ loses its polarization and concurrently its spontaneous strain at its ferroelectric Curie temperature (T$_C$) of 120 °C. BaTiO$_3$ is cubic above T$_C$. Below T$_C$ and at room temperature BaTiO$_3$ is tetragonal with a c/a value of about 1.1%. The balancing of elastic and electrostatic energies of the system creates ferroelectric domains in an effort to minimize the energy. The tetragonal distortion of domains across the crystal surface have been confirmed with X-ray diffraction techniques [164].

The ferroelectric domains can be imaged locally using PFM. An alternating voltage is applied to the sample in contact mode using a conducting tip and the sample vibrates due to the piezoelectric effect. Vertical and lateral motions of the tip are

149

measured by reflecting a laser off the conducting tip and onto a position diode. While the tip rasters over the sample surface, the amplitude and/or phase of the tip deflection is recorded and compiled into an image. The images reveal ferroelectric domains down to tens of nanometer precision. An example PFM image of $BaTiO_3$ a-c-domains is shown in Figure 4-16.
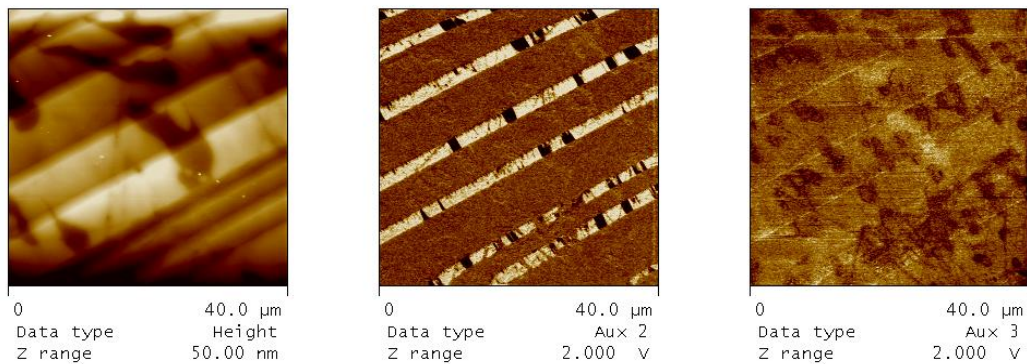
Figure 4-16 PFM images of an etched $BaTiO_3$ surface. The left image is topography, the middle is lateral PFM amplitude, and the right image is vertical PFM amplitude.

In the topography image of Figure 4-16 it's clear that diagonal stripes correspond to the diagonal ferroelectric domains in the lateral PFM image. The $BaTiO_3$ surface topography arises from the tetragonal lattice distortion which causes height displacement at the surface in order to lattice match the differently oriented ferroelectric domains [165].

The a-domains in Figure 4-16 are long in the crystallographic (100) direction and the ferroelectric c-domains are wider [165]. The strain direction for a-domains lies perpendicular to the length of the a-domain [166], [167], or the (010) direction. The ferroelectric c-domains are strained out-of-plane in the (001) direction (out of the

150

page) hence presenting a cubic face of the tetragonal unit cell to the surface. A corresponding modulation in strain is present at the surface of the $BaTiO_3$ crystal from the ferroelectric a-c-domain pattern [168]. More specifically, there is an isotropic strain over c-domains and a uniaxial tensile strain over a-domains of 1.1%.
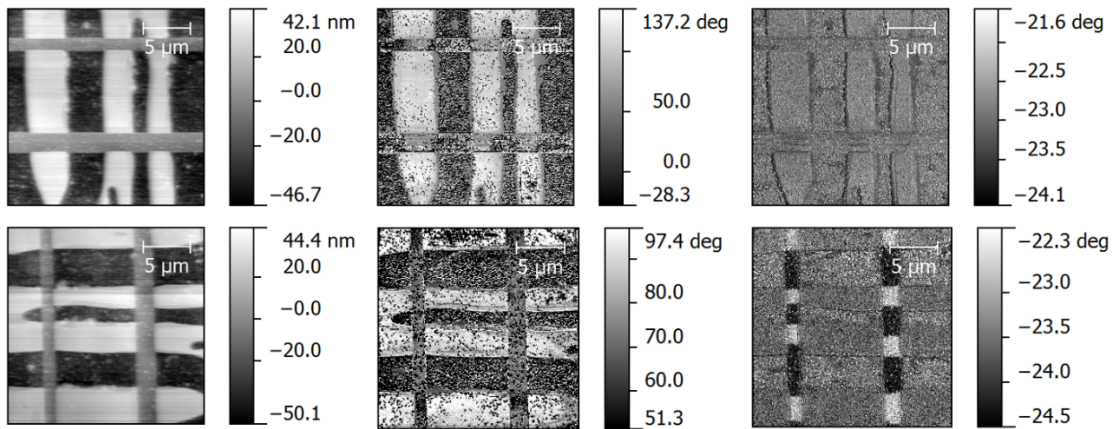
Figure 4-17 Two PFM image set measured on the same spot after 90 degree sample rotation show the differences in lateral PFM signal in the right-most images. Images from left to right are topography, vertical PFM, lateral PFM. The top and bottom sets of images are rotated 90° from one another.

The strain directions mentioned in the previous paragraph were confirmed using PFM by taking two scans of the same area but physically rotating the sample by 90°. This method takes advantage of the lateral PFM signal which only has signal when a force is applied laterally to the tip as explained in Section 4.5. Because a-domains have a strain in the plane of the surface they will give an in-plane strain when an electric field is applied. In Figure 4-17 the scan direction is horizontal in the images and the tip is pointed vertically, so lateral PFM contrast is only seen when a lateral force on the tip is made as in the bottom right image. The black and white areas are

151

different a-domains pointing left and right. The vertical PFM images are in the middle and are very similar since the vertical component of motion is not change by rotation of the sample. This confirms that the strain direction of ferroelectric a-domains is pointed perpendicularly to the length of the a-domains, which becomes important later for interpretation of magnetostrictive films coupled to ferroelectric a-domains.

Chapter 5. Transcritical Permalloy on BaTiO$_3$ Study

5.1 Summary and Methods for Composite Multiferroics Study

In this study we used MFM to image the magnetic domain pattern of transcritical Permalloy (tPy) films deposited on BaTiO$_3$ single crystals. We experimentally observed local changes in the magnetic anisotropy of tPy consistent with the ferroelectric a-c-domain pattern of a BaTiO$_3$ crystal after cooling from above the Curie temperature (T$_C$) of BaTiO$_3$. MFM images of the magnetic domain patterns give us quantitative information about average in-plane magnetization direction and out-of-plane anisotropy energies. Micromagnetic simulations of the MSD orientation and the periodicity show that inverse magnetostriction from a uniaxial tensile strain on the tPy over ferroelectric a-domains can account for the observed changes.

The motivation for this study comes from the desire to make low-power memory and logic devices. Due to Moore's law, integrated circuits have reached such a high density that heat dissipation has become a problem on-chip. Multiferroic heterostructures offer particularly promising properties for memory systems because they use an electric field to alter magnetic domains rather than electric currents like in hard-disc drives or spin-torque transfer type memories.

Next we describe in some detail the various steps to prepare the sample. A number of different BaTiO$_3$ substrates were studied to determine which one had the smoothest surfaces to provide the appropriate test bed to clearly show any local magnetoelectric effect. Any roughness or junk will complicate coupling and compromise any imaging necessary to observe the effect. Commercial substrates deemed optically smooth have considerable roughness from left over polishing slurry,

recrystallization during final annealing and unknown junk and particles. Commercial BaTiO₃ substrates use the top-seeded growth (TSG) method much like the Czochralski process used to grow silicon boules for the semiconducting industry. The substrates then need to be cut, polished, and recrystallized for various applications. In contrast, the flux method uses a mechanism similar to the growth of sugar crystals where a solute is used to dissolve the crystal constituents and as the solution slowly cools, the crystals nucleate and grow. The advantage of the flux method is that atomically flat surfaces are grown natively during the process which are optimal for the sensitive interface based strain mechanism we want to study here. This was the crystal of choice for this study.

One disadvantage of the flux grown crystals is that iron is added to improve oxygen deficiencies and lower conductivity. As noted by Remeika, an addition of 0.2% ferroic oxide improves the quality of the crystals [169]. We used WDS to measure our crystals for iron and found approximately 0.1 atomic % Fe. After etching the surface for a few seconds in aqua regia (1:3 ratio of nitric to hydrochloric acid) the iron value dropped to 0.05 at%. TSG crystals do not contain Fe, which may be seen as an advantage in the present study since additional magnetic particles may complicate analysis.

During the film optimization process we verified that the stripe domain period (Λ) had the expected square root dependence on the tPy film thickness [155], [157], [159] as shown in Figure 5-1(a). The MSD period and orientation were determined by atomic force microscope (AFM) calibrated with a 3 μm grid. Two dimensional Fast Fourier Transform (2D-FFT) analysis of MFM images was used to obtain accurate
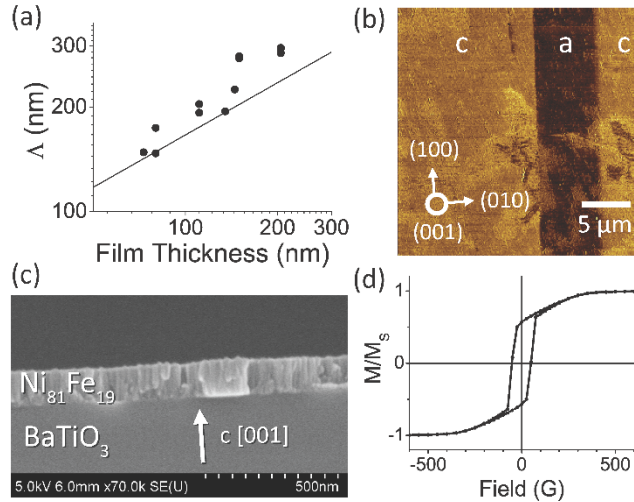
Figure 5-1(a) Thickness dependence of stripe domain period (Λ) on log scale. (b) Typical PFM image of the BaTiO3 single-crystal with ferroelectric a-c-domains labelled. (c) SEM cross-section of our tPy/BaTiO3 heterostructure showing the microstructure of the tPy. (d) Normalized in-plane magnetic hysteresis loop of tPy.

stripe domain information. The thermal treatment was done in air by placing the heterostructure on a hotplate and immediately after reaching 150 °C was set on a metal block to cool to room temperature. The experimental procedure is as depicted in Figure 5-2 where piezo-response force microscopy (PFM) is first used to confirm the ferroelectric a-c-domains are present on the sample where some example PFM images are shown in Figure 5-1(b). Next, the 100 nm tPy film is deposited at room temperature onto the BaTiO$_3$. Then the "before" MFM images are taken at dozens of areas on the sample, then the sample is brought up to BaTiO$_3$'s T$_C$ of 120°C. Finally, the "after" MFM images are taken and the images are compared. Two separate simulations using the object oriented micromagnetic framework (OOMMF) software were carried out to quantify the changes that occurred.
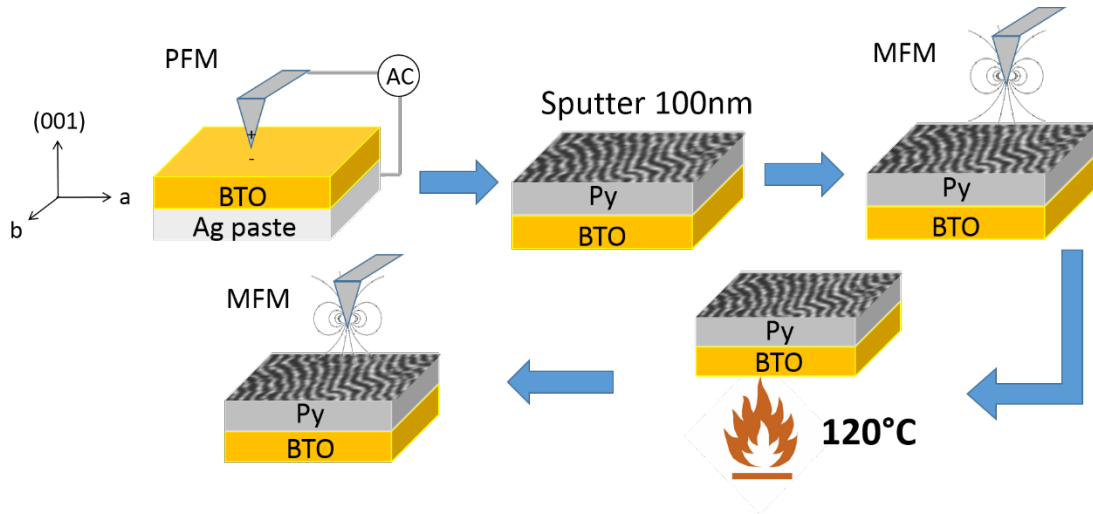
Figure 5-2 Experimental procedure for the tPy/BaTiO$_3$ heterostructure from confirming the ferroelectric a-c-domains are present, to thin film sputtering, to MFM images being taken before and after the heat treatment.

5.2 Changes in Magnetic Stripe Orientation

Dozens of areas were imaged with MFM before and after cooling the tPy/BaTiO$_3$ heterostructure from above the T$_C$ of BaTiO$_3$ to room temperature. Before thermal treatment, stripe domains were found covering the sample and often pointed in a single direction irrespective of the underlying ferroelectric BaTiO$_3$ domains (as shown in Figure 5-3(a)). This indicates that the magnetic anisotropy of the as-deposited tPy was not affected by the underlying ferroelectric substrate before thermal treatment. The initial stripe domain direction shown in Figure 5-3(a) is an arbitrary angle since no deliberate magnetic fields were applied during the deposition.

Figure 5-3(b) shows the MFM image after cooling from above BaTiO$_3$'s T$_C$ back to room temperature. The striking result is the sharp break of stripe domain orientation at the ferroelectric domain boundaries observed only after thermal treatment. The ferroelectric domain boundaries depicted in Figure 5-3 are deduced

from the simultaneously captured AFM images (not shown). One clearly sees that stripe domain orientation changes only over the ferroelectric a-domain area and remains in the same direction over c-domains. As a comparison, we also investigated the strain effect of Si on the magnetic domains of tPy in a tPy/Si sample that was made with the same conditions as tPy/BaTiO$_3$. No changes were observed in the MSD configuration comparing the MFM images before and after thermal treatment for the tPy/Si sample. This is due to the fact that Si does not have strain modulation over its surface. Therefore, the change of MFM images in the tPy/BaTiO$_3$ before and after thermal treatment is from the uniaxial strain of BaTiO$_3$'s ferroelectric a-domains.
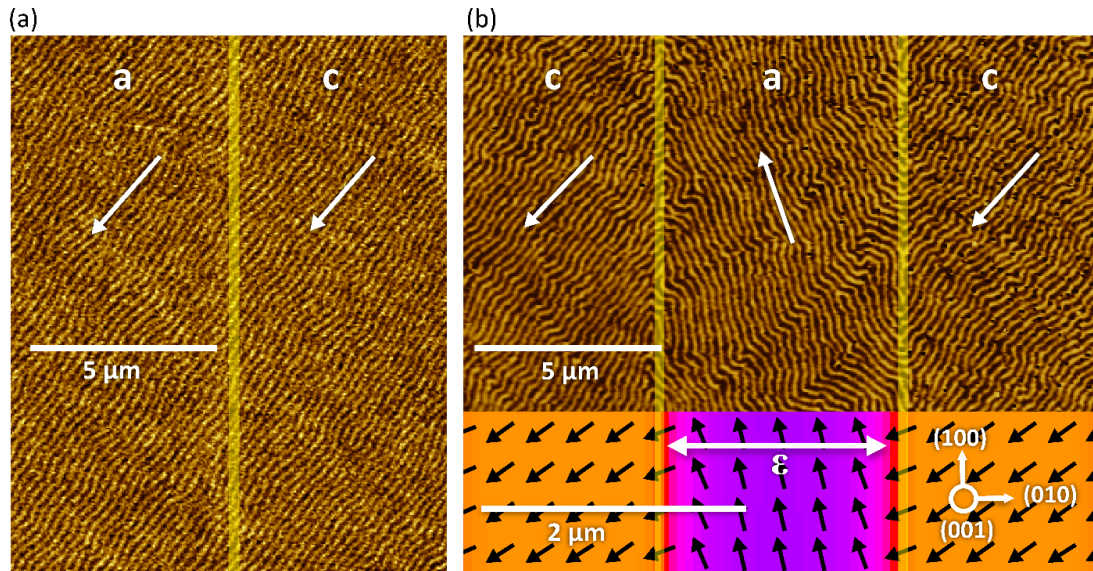
Figure 5-3 MFM images of the tPy/BaTiO3 heterostructure before thermal treatment (a) and after thermal treatment (b). Ferroelectric domain boundaries are indicated by translucent yellow lines. White arrows indicate average stripe domain orientation. The double-sided arrow in (b) points along the uniaxial strain direction over the a-domain. Ferroelectric a-c-domains are labelled in white. Results of in-plane OOMMF simulation are pictured below experimental MFM results in (b).

Changes of the stripe domain orientation are due to the inverse magnetostrictive effect of tPy. Permalloy at the $Ni_{81}Fe_{19}$ composition is slightly negative magnetostrictive. Applying tensile strain to a negative magnetostrictive material forces the magnetic moments to point perpendicular to the direction of tensile strain[33]. Figure 5-3(b) shows that stripe domains were forced to point almost perpendicular to the uniaxial tensile strain or along the a-domain length. The competition of in-plane magnetostatic, magnetoelastic, and exchange energy in the tPy prevents a full alignment of the stripe domains along the a-domain length. On the other hand, stripe domains over ferroelectric c-domains do not change after the thermal treatment because the strain over c-domains is always isotropic. $BaTiO_3$ is cubic above T_C [170] and below T_C, the cubic side of the unit cell faces the surface for ferroelectric c-domains.

5.3 Introduction to numerical micromagnetic simulation

Micromagnetics is the study of how magnetism behaves at the sub-micron scale. The Landau-Lifshitz-Gilbert (LLG) equation offers an iterative solution to solve for the distribution of magnetic moments throughout the volume of a sample. The National Institute of Standards and Technology (NIST) has developed a user friendly interface called Object Oriented Micromagnetic framework (OOMMF) [171] to apply the LLG equation. OOMMF is applicable to solutions tractable on a single PC or to solutions requiring the power of many collective computers.

A number of parameters are entered into the micromagnetic solver in OOMMF including materials parameters (magnetization, M (A/m), exchange stiffness A (J/m), crystalline anisotropy (J/m^3) , anisotropy type (uniaxial, biaxial),

anisotropy direction), in addition to sample dimensions, cell size, and any external magnetic fields desired. The cell size serves as the dimension of a brick used as the basic block of a calculation. In addition to these parameters solvers can take into consideration periodic boundary conditions to reduce computational expense in the case of repeating structures. The cell size and sample dimensions require ample consideration because these determine the time the simulation will take to reach a stable state. Presented in Figure 5-4 is a screen shot of the software where the magnetization and Zeeman field plots are displayed.
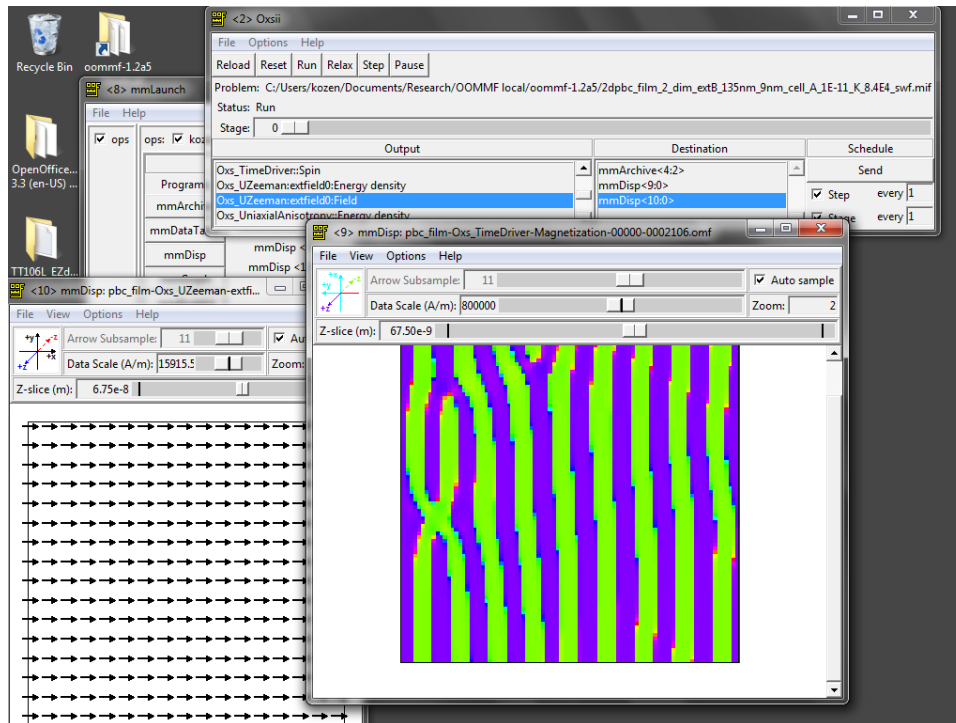
Figure 5-4 A screen shot of the OOMMF software.

The selection of boundary conditions was particularly important in the second simulation for magnetic stripe domain period. One can easily see in Figure 5-5 how drastically the use of periodic boundary conditions (PBCs) on the right, compared to open boundary conditions on the left. The PBCs also dramatically reduce the computational cost for repetitive domain structure like stripe domains.
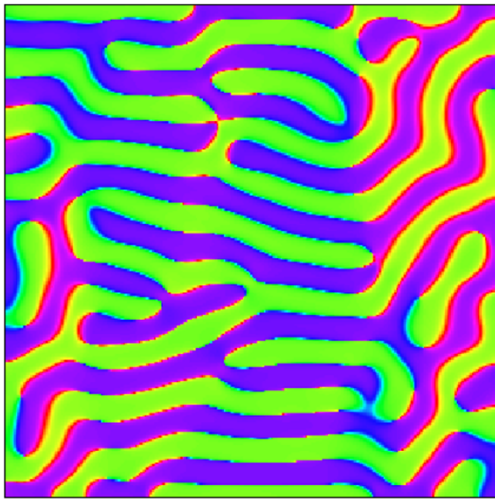
Boundary conditions
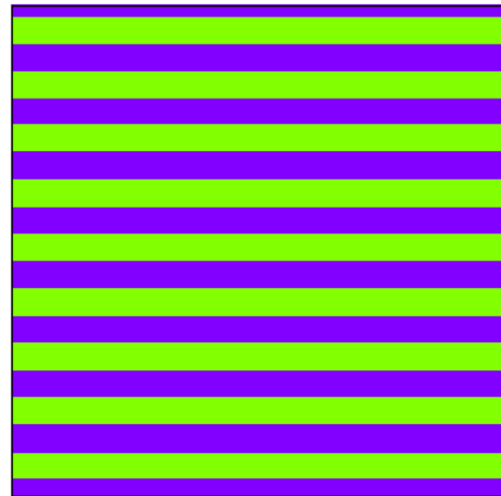
Figure 5-5 Comparison of open boundary conditions on the left to using periodic boundary conditions in the horizontal direction for the right image.

5.4 OOMMF Simulation of Transcritical Permalloy

Micromagnetic simulations of the stripe domain pattern were carried out to support the hypothesis that local magnetic anisotropy of tPy can be controlled by strain from $BaTiO_3$'s ferroelectric domains. The first simulation is of the sharp breaks in

MSD orientation in Figure 5-3(b). Based on previous work for tPy [155], [157], [161], we take the direction parallel to the stripe domain lines in the MFM images to be the direction of the average in-plane magnetization. We set the in-plane magnetic anisotropy energy of the simulated tPy as K^{IP} = 3 kPa which is close to other cited values[172]. In the c-domain areas we chose a magnetic anisotropy direction the same as the stripes in Figure 5-3(a) before thermal treatment. The magnetic anisotropy over the ferroelectric a-domain area points along the domain length as deduced from the phenomenology of inverse magnetostriction described above. Using the same crystallographic axes and domain configuration as Figure 5-3(b) we input an initial magnetization direction of $(1\bar{1}0)$ to OOMMF. The simulation dimensions were 4096 nm × 4096 nm × 8 nm with a cell size of 8 nm. Edge effects were reduced by doing an edge-field computation [173] for each of the four edges in the x-y plane and any edge effects were cropped from the figure.

The bottom of Figure 5-6(b) shows the results of the in-plane simulation where the direction of magnetization from OOMMF agrees with the stripe domain direction in experimental MFM data above. The in-plane magnetic anisotropy magnitude was used to match simulated and experimental magnetization directions over the ferroelectric a-c-domain pattern. If K^{IP} is too small the moments over the a-domain turn towards those of the c-domains. If K^{IP} is too large then moments over the a-domain point directly along the a-domain length, in contradiction with experiment. Now we use the equation for inverse magnetostriction to show that this magnetic anisotropy energy originates from strain. The magnetic anisotropy energy $K^{IP} = -\frac{3}{2}\lambda\sigma$ where λ is the magnetostriction constant and the stress is $\sigma = Y\varepsilon/1 - v^2$.
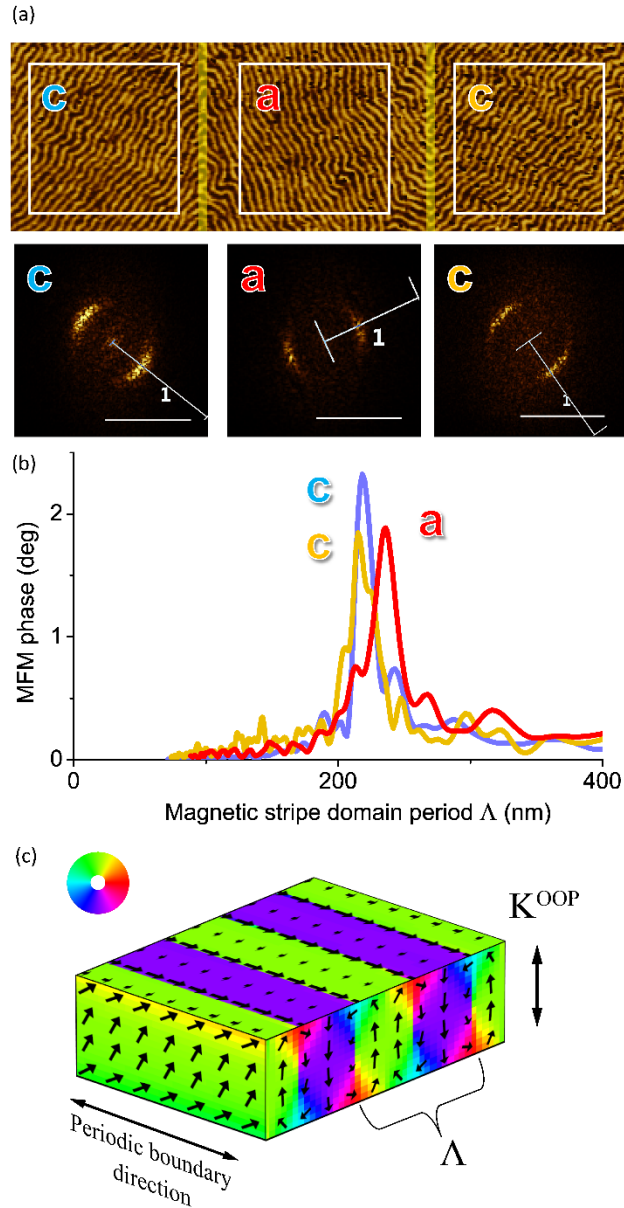
Figure 5-6 White boxes surround representative areas of the MFM image for 2D-FFT analysis. The transforms below each respective area have radial lines where cross-sections were taken. The bar is 10 μm^{-1}. (b) Cross-sections of each transform were overlaid, color-coded, and plotted versus stripe domain period. (c) Cartoon of out-of-plane OOMMF simulation showing the stripe domain period Λ, direction of the out-of-plane anisotropy energy KOOP and direction of the periodic boundary conditions. Black arrows are simulated magnetic moments in their respective planes and the color wheel indicates the magnetic moment direction on each plane.

Constants used for tPy were Young's modulus [174], [175] $Y = 190 \pm 13 \, GJ/m^3$, Poisson's ratio $v = 0.37$ and strain from the BaTiO$_3$ substrate was $\varepsilon = 1.1 \pm 0.1\%$. We solved for the magnetostriction constant of tPy as $\lambda_{IP} = -0.8 \pm 0.1$ ppm. This calculated magnetostriction value agrees with recent studies [151] and is convincing evidence that the magnetic anisotropy energy is from the elastic coupling of the tPy to the ferroelectric BaTiO$_3$ substrate.

We also observed a modulation of stripe domain period, or stripe domain width, over the ferroelectric a-c-domain pattern after the multiferroic heterostructure was cooled from above the T$_C$ of BaTiO$_3$. Figure 5-6(a) and Figure 5-6(b) show that stripe domain period changed systematically over different ferroelectric domains. Figure 5-6(b) shows that stripe domains over ferroelectric a-domains have a larger period than over c-domains. 2D-FFT analysis [176] taken over the whole image gave the MSD period over ferroelectric a-domains as $\Lambda_a = 233 \pm 1$ nm and MSD period over ferroelectric c-domains as $\Lambda_c = 226 \pm 1$ nm. The error in period is calculated as the total image width (20 μm) divided by the number of pixels (512 pixels) divided by the number of stripes averaged over (30 stripes) and rounded.

To confirm this strain-based control of out-of-plane magnetic anisotropy we carried out a second simulation on the change observed in the MSD period. We used one-dimensional periodic boundary conditions parallel with the stripe domain line direction to reduce computational expense. Figure 5-6(c) shows a cartoon of the second simulation where simulated in-plane and out-of-plane magnetic moments can be visualized as black arrows and as color. The simulated stripe period is from the z-component of the magnetization averaged through the thickness of the film. The full

simulation is a cross-section of the stripe domains of dimensions 8192 nm × 64 nm (periodic) × 114 nm with a cell size of 2 nm. An out-of-plane anisotropy energy for the ferroelectric a-domain of $K_a^{OOP} = 27$ kPa gave a calculated stripe domain period of $\Lambda_a^{sim} = 233.9$ nm. A larger out-of-plane anisotropy energy over ferroelectric c-domains of $K_c^{OOP} = 30$ kPa gave $\Lambda_c^{sim} = 227.5$ nm. Some boundary effects in the cross section were evident and were not included in the calculated stripe period.

The calculated stripe domain periods agree with their experimental counterparts assuming the trend of stripe domain period with out-of-plane anisotropy energy suggested earlier by Pant et al. Notice that $K_c^{OOP} - K_a^{OOP} = 3$ kPa is the same energy for the change of stripe domain orientation in-plane. The reduction of the out-of-plane anisotropy energy over the ferroelectric a-domain is the same as the energy it takes to change the stripe domain orientation in-plane. We propose that the thin-film geometry causes a preference for the magnetic anisotropy to turn in-plane instead of the less energetically favorable out-of-plane direction.

5.5 Conclusions of Composite Multiferroic study and Future Work

In conclusion, we experimentally observed the modification of magnetic stripe domain orientation and period in tPy after cooling the tPy/BaTiO$_3$ (001) heterostructure from above the T_C of BaTiO$_3$ to room temperature. MFM investigation shows that the stripe domains sharply changed orientation at the ferroelectric domain boundary and the stripe domain period is larger over the ferroelectric a-domains compared to stripe domains over ferroelectric c-domains. OOMMF simulations indicated that a 3kPa in-plane magnetic anisotropy energy accounts for the change in the magnetic stripe domain orientation over the ferroelectric a-domain. An equal

decrease in the out-of-plane anisotropy energy accounted for the increase of the stripe period over the ferroelectric a-domain. This nanoscale control of magnetic anisotropy energy arose from the 1% strain of the $BaTiO_3$ substrate on the magnetostrictive tPy film.

Future studies will include both experimental and modeling of unique ferroelectric heterostructures. The next experimental step is to induce magnetic switching with an applied electric field as oppose to the thermal approach taken here. However, large voltages are needed to switch a thick $BaTiO_3$ substrate, making the heterostructure presented here unrealistic for applications. Thin films can be used to reduce the voltage required for switching of the strain state in the ferroelectric. However, the ferroelectric film would be strongly clamped to the substrate, which greatly reduces the strain actuation of the ferroelectric film. One possible solution has been developed by our group where bi-layer ferroelectric thin films have two different crystal structures of $Pb-Zr-TiO_3$ (PZT) that allows the film to retain the large strain of the bulk material even when it is "clamped" to a substrate [177]. Hence, future studies should use bi-layer PZT with magnetic bits patterned on top in an all-thin-film device structure. The all-thin-film device would lower the voltages required for switching to below 10 V allowing in-situ MFM measurements with standard equipment.

Use of the all-thin-film approach will be more viable for applications in digital memory, but the optimal shape and size of the patterned magnetic bit is non-trivial because the strain-based geometry only switches the magnetization by 90°. 180° switching is preferable for switching of the magnetic state to have the largest signal to noise ratio when using the giant magnetoresistance (GMR) effect. GMR is a viable

option for the reading of strain based magnetic switching state [178]. Shape anisotropy and quick voltage pulses is one way to address the apparent limitation of 90° magnetization switching in strain-based devices. For example, phase-field simulations have been carried out for a patterned Ni nanomagnet with a four-fold magnetic easy axis undergoing a 180° magnetization reversal from a magnetoelastic effect [179]. This type of magnetic bit pattern could be realized on the bi-layer PZT films described above. More compact and efficient memory devices are not that far in the future.

In addition to the above outline for future experimental work, some future modeling work would also greatly benefit the efforts taken thus far to understand the local control of strain on magnetization. A number of interesting effects were found experimentally by other groups including the disappearance of magnetic stripe domains with an isotropic strain from the substrate, as well as stripe domain wall changes [141], [145]. These types of sensitive magnetic systems near critical points are of interest for application as sensors and in digital memory. For example, if the parameters necessary for the switching of magnetization from in-plane to out-of-plane direction could be optimized, then a viable perpendicular oriented type strain-based magnetic memory could be fabricated. The goal would be to find the optimal materials and geometric requirements for such a metastable state first using modeling and then testing experimentally. The advantage of modeling today is that powerful computation has become easily available. In addition, reliable programs like OOMMF have proven they are up to carrying out simulations in an automated way to explore the large phase spaces of magnetic phenomenon [180]. In this way, a phase diagram for the different

states in magnetic stripe domains could be created to understand its meta-stable

regions where a small energy can induce a large change in magnetization direction.

Appendix A: Batch Background Subtraction with Match!

Here is an example MATLAB script to automate the process of doing background subtraction using the analysis software Match! from Crystal Impact GbR (http://crystalimpact.com/match/Default.htm). Match! has a trial version and the developers are very helpful with further development of their software. Don't be afraid to contact them for advice and reporting of errors.

```
%This script is meant to automate background subtraction using
%Match!
%This script was written for MATLAB on Mac however only the
%directory syntax and the syntax for executing the batch file below
%need to be edited.
%First, change directory to location of your Match! installation.

cd('/Applications/Match2');

%Start by importing a combiview formatted file where the first row
%is 2theta values, d, or Q, and the rows below are the spectra
%intensity data for each remainin X-ray diffraction spectra.

XRD = importdata('/Users/SeanFackler/Dropbox
(Takeuchi_share)/Research/FeCoX_Master/FeCoV/FeCo-
V_130719b/combiview/PP_FeCoV_130719b_combiview_140303a.txt');

s = size(XRD);
for ii=2:s(1)
xrd = [XRD(1,:)' XRD(ii,:)'];

%Each spectra is written as a text file to be imported into Match!.
%Edit the file path accordingly.

data_file_loc = '/Users/SeanFackler/Documents/autodata.txt';
dlmwrite(data_file_loc,xrd,'delimiter', '\t');

%Here, the batch file text is shown. Be sure to edit the various
%file paths below so they are exported to where you would like them.
%The exclamation point means that the command will NOT be executed
%in Match!. The up-to-date commands can be found in Tutorial.pdf in
%the root folder after installing Match!.

text = {'MATCH!_2_BATCH',...
'set_default_abscissa(d)',...
['import("' data_file_loc '")'],...
'!strip_K_alpha2',...
'subtract_background_automatic',...
'smooth_exp_raw_data',...
```

```
'export_profile_data("/Users/SeanFackler/Documents/auto_profile.dat"
)',...
'!export_pattern_graphics("/Users/SeanFackler/Documents/auto_pattern
.jpg",JPG,1024,768,false)',...
'!save_document("/Users/SeanFackler/Documents/testdoc.mtd")',...
'finish',...
'close'};
%'set_default_wavelength(1.541874)',...
%'find_peaks_normal(0.1,40.0,1)',...
%'search-match',...
%'!select_matching_automatic',...
%'export_matchlist("C:\Users\akusne\Dropbox\Combi_work\code\Match\au
to_matchlist.csv",CSV)',...
%'export_peaklist("C:\Users\akusne\Dropbox\Combi_work\code\Match\aut
o_peaklist.csv",CSV)',...
%'export_resultslist("C:\Users\akusne\Dropbox\Combi_work\code\Match\
auto_resultslist.csv",CSV)',...
batch_file_loc = '/Users/SeanFackler/Documents/auto_batch.mbf';
fid = fopen(batch_file_loc,'w');
for i=1:length(text)
    fprintf(fid,'%s\n',text{i});
end
fclose(fid);


%This section executes the batch file. For windows, delete "open -a"
%and add ".exe" to Match!, and edit the file path.
%Here, the analyzed data is also imported back into MATLAB for
%further plotting and analysis.
dos('open -a Match! /Users/SeanFackler/Documents/auto_batch.mbf');
    pause(3);
    dos('killall Match!');
    xrd_ =
importdata('/Users/SeanFackler/Documents/auto_profile.dat');
    l = length(xrd_);
    XRD_(ii-1,:) = xrd_(:,2)';

end
```

Some settings may need to be edited in Match!, in particular those under the

"Batch" tab. The desired automatic data analysis and closing sequence should be

chosen and don't forget to click the "save as default" box in the bottom left before

closing the options window.

Appendix B: Publications Related to This Dissertation

1. S. W. Fackler, M. J. Donahue, T. Gao, P. N. A. Nero, S.-W. Cheong, J. Cumings, and I. Takeuchi, "Local control of magnetic anisotropy in transcritical permalloy thin films using ferroelectric BaTiO3 domains," *Applied Physics Letters*, vol. 105, no. 21, p. 212905, Nov. 2014.

2. J. Unguris, S. R. Bowden, D. T. Pierce, M. Trassin, R. Ramesh, S.-W. Cheong, S. Fackler, and I. Takeuchi, "Simultaneous imaging of the ferromagnetic and ferroelectric structure in multiferroic heterostructures," *APL Materials*, vol. 2, no. 7, p. 076109, Jul. 2014.

3. T. R. Gao, Y. Q. Wu, S. Fackler, I. Kierzewski, Y. Zhang, A. Mehta, M. J. Kramer, and I. Takeuchi, "Combinatorial exploration of rare-earth-free permanent magnets: Magnetic and microstructural properties of Fe-Co-W thin films," *Applied Physics Letters*, vol. 102, no. 2, p. 022419, Jan. 2013.

4. K. Jin, R. Suchoski, S. Fackler, Y. Zhang, X. Pan, R. L. Greene, and I. Takeuchi, "Combinatorial search of superconductivity in Fe-B composition spreads," *APL Materials*, vol. 1, no. 4, p. 042101, Oct. 2013.

Bibliography

[1]   Office of the Under Secretary of Defense and for Acquisition, Technology and Logistics, "Strategic and Critical Materials 2013 Report on Stockpile Requirements." the Department of Defense, Jan-2013.

[2]   O. Le Bacq, O. Eriksson, B. Johansson, P. James, and A. Delin, "First-principles calculations of the magnetic anisotropy energy of Fe-V multilayers," *Phys. Rev. B*, vol. 65, no. 13, p. 134430, Mar. 2002.

[3]   H. Ebert, R. Zeller, B. Drittler, and P. H. Dederichs, "Fully relativistic calculation of the hyperfine fields of 5d‑impurity atoms in ferromagnetic Fe," *J. Appl. Phys.*, vol. 67, no. 9, pp. 4576–4578, May 1990.

[4]   A. Broddefalk, P. Nordblad, P. Blomquist, P. Isberg, R. Wäppling, O. Le Bacq, and O. Eriksson, "In-plane magnetic anisotropy of Fe/V (0 0 1) superlattices," *J. Magn. Magn. Mater.*, vol. 241, no. 2–3, pp. 260–270, Mar. 2002.

[5]   V. M. Zakharov, M. A. Libman, and E. I. Estrin, "On the role of atomic ordering in the formation of a high-coercivity state in iron-cobalt-vanadium alloys," *Phys. Met. Metallogr.*, vol. 113, no. 1, pp. 43–47, Jan. 2012.

[6]   M. Repetto and P. Uzunov, "Analysis of Hysteresis Motor Starting Torque Using Finite Element Method and Scalar Static Hysteresis Model," *IEEE Trans. Magn.*, vol. 49, no. 5, pp. 2405–2408, May 2013.

[7]   T. Sourmail, "Near equiatomic FeCo alloys: Constitution, mechanical and magnetic properties," *Prog. Mater. Sci.*, vol. 50, no. 7, pp. 816–880, Sep. 2005.

[8]   I. Takeuchi, O. O. Famodu, J. C. Read, M. A. Aronova, K.-S. Chang, C. Craciunescu, S. E. Lofland, M. Wuttig, F. C. Wellstood, L. Knauss, and A. Orozco, "Identification of novel compositions of ferromagnetic shape-memory alloys using composition spreads," *Nat. Mater.*, vol. 2, no. 3, pp. 180–184, Mar. 2003.

[9]   J. R. Hattrick-Simpers, D. Hunter, C. M. Craciunescu, K. S. Jang, M. Murakami, J. Cullen, M. Wuttig, I. Takeuchi, S. E. Lofland, L. Benderksy, N. Woo, R. B. V. Dover, T. Takahashi, and Y. Furuya, "Combinatorial investigation of magnetostriction in Fe–Ga and Fe–Ga–Al," *Appl. Phys. Lett.*, vol. 93, no. 10, p. 102507, Sep. 2008.

[10]   D. Hunter, W. Osborn, K. Wang, N. Kazantseva, J. Hattrick-Simpers, R. Suchoski, R. Takahashi, M. L. Young, A. Mehta, L. A. Bendersky, S. E. Lofland, M. Wuttig, and I. Takeuchi, "Giant magnetostriction in annealed Co1−xFex thin-films," *Nat. Commun.*, vol. 2, p. 518, Nov. 2011.

[11]   M. Pedram and S. Nazarian, "Thermal Modeling, Analysis, and Management in VLSI Circuits: Principles and Methods," *Proc. IEEE*, vol. 94, no. 8, pp. 1487–1501, Aug. 2006.

[12]   K. Roy, S. Bandyopadhyay, and J. Atulasimha, "Hybrid spintronics and straintronics: A magnetic technology for ultra low energy computing and signal processing," *Appl. Phys. Lett.*, vol. 99, no. 6, p. 063108, Aug. 2011.

[13]   J. Edgecumbe, L. G. Rosner, and D. E. Anderson, "Preparation and Properties of Thin‑Film Hard Superconductors," *J. Appl. Phys.*, vol. 35, no. 7, pp. 2198–2202, Jul. 1964.

[14] J. J. Hanak, "The 'multiple-sample concept' in materials research: Synthesis, compositional analysis and testing of entire multicomponent systems," *J. Mater. Sci.*, vol. 5, no. 11, pp. 964–971, Nov. 1970.

[15] A. Furka, F. Sebestyen, M. Asgedom, and G. Dibo, "General method for rapid synthesis of multicomponent peptide mixtures," *Int. J. Pept. Protein Res.*, vol. 37, no. 6, pp. 487–493, 1991.

[16] National Science and Technology Council, "Materials Genome Initiative for Global Competitiveness." the White House, 24-Jun-2011.

[17] R. J. Brodd, "Comments on the History of Lithium-Ion Batteries," in *The Electrochemical Society*, 2013.

[18] M. S. Whittingham, "Electrical Energy Storage and Intercalation Chemistry," *Science*, vol. 192, no. 4244, pp. 1126–1127, Jun. 1976.

[19] "New Commitments Support Administration's Materials Genome Initiative," *The White House*. [Online]. Available: http://www.whitehouse.gov/blog/2012/05/14/new-commitments-support-administration-s-materials-genome-initiative. [Accessed: 15-Apr-2015].

[20] M. Jansen, "A Concept for Synthesis Planning in Solid-State Chemistry," *Angew. Chem. Int. Ed.*, vol. 41, no. 20, pp. 3746–3766, Oct. 2002.

[21] L. Zhang, J. Wang, Y. Du, R. Hu, P. Nash, X.-G. Lu, and C. Jiang, "Thermodynamic properties of the Al–Fe–Ni system acquired via a hybrid approach combining calorimetry, first-principles and CALPHAD," *Acta Mater.*, vol. 57, no. 18, pp. 5324–5341, Oct. 2009.

[22] K. M. Rabe, "First-Principles Calculations of Complex Metal-Oxide Materials," *Annu. Rev. Condens. Matter Phys.*, vol. 1, no. 1, pp. 211–235, Aug. 2010.

[23] K. M. Nicholson and D. S. Sholl, "First-Principles Prediction of New Complex Transition Metal Hydrides for High Temperature Applications," *Inorg. Chem.*, vol. 53, no. 22, pp. 11849–11860, Nov. 2014.

[24] A. G. Kusne, T. Gao, A. Mehta, L. Ke, M. C. Nguyen, K.-M. Ho, V. Antropov, C.-Z. Wang, M. J. Kramer, C. Long, and I. Takeuchi, "On-the-fly machine-learning for high-throughput experiments: search for rare-earth-free permanent magnets," *Sci. Rep.*, vol. 4, Sep. 2014.

[25] Kathy Klotz-Guest, "Intermolecular and Elpida Launch R&D Collaboration For Next-Generation Memory Technology." Press Release Intermolecular Inc., 15-Jul-2008.

[26] R. Potyrailo, K. Rajan, K. Stoewe, I. Takeuchi, B. Chisholm, and H. Lam, "Combinatorial and High-Throughput Screening of Materials Libraries: Review of State of the Art," *ACS Comb. Sci.*, vol. 13, no. 6, pp. 579–633, Nov. 2011.

[27] J.-C. Zhao, M. R. Jackson, L. A. Peluso, and L. N. Brewer, "A Diffusion Multiple Approach for the Accelerated Design of Structural Materials," *MRS Bull.*, vol. 27, no. 04, pp. 324–329, Apr. 2002.

[28] J. F. Whitacre, W. C. West, and B. V. Ratnakumar, "A Combinatorial Study of Li y Mn x Ni2 − x O 4 Cathode Materials Using Microfabricated Solid-State Electrochemical Cells," *J. Electrochem. Soc.*, vol. 150, no. 12, pp. A1676–A1683, Dec. 2003.

[29] K. Jin, R. Suchoski, S. Fackler, Y. Zhang, X. Pan, R. L. Greene, and I. Takeuchi, "Combinatorial search of superconductivity in Fe-B composition spreads," *APL Mater.*, vol. 1, no. 4, p. 042101, Oct. 2013.

[30] A. Ludwig, J. Cao, J. Brugger, and I. Takeuchi, "MEMS tools for combinatorial materials processing and high-throughput characterization," *Meas. Sci. Technol.*, vol. 16, no. 1, p. 111, Jan. 2005.

[31] H. O. A J Zambano, "Dependence of exchange coupling interaction on micromagnetic constants in hard/soft magnetic bilayer systems," *Phys. Rev. B Condens. Matter*, vol. 75, 2007.

[32] G. Garcia, R. Doménech-Ferrer, F. Pi, J. Santiso, and J. Rodríguez-Viejo, "Combinatorial Synthesis and Hydrogenation of Mg/Al Libraries Prepared by Electron Beam Physical Vapor Deposition," *J. Comb. Chem.*, vol. 9, no. 2, pp. 230–236, Mar. 2007.

[33] H. Oguchi, J. Hattrick-Simpers, I. Takeuchi, E. J. Heilweil, and L. A. Bendersky, "An infrared imaging method for high-throughput combinatorial investigation of hydrogenation-dehydrogenation and new phase formation of thin films," *Rev. Sci. Instrum.*, vol. 80, no. 7, p. 073707, Jul. 2009.

[34] H. Koinuma and I. Takeuchi, "Combinatorial solid-state chemistry of inorganic materials," *Nat. Mater.*, vol. 3, no. 7, pp. 429–438, Jul. 2004.

[35] Superconductivity Research Group, "A schematic diagram of the principle of operation of the laser ablation system," *Pulsed Laser Deposition Facility*. [Online]. Available: http://www.cm.ph.bham.ac.uk/research/thinfilms/pulsedlaser.html.

[36] Hiroyuki Oguchi, "Combinatorial Investigation of Intermetallics Using Electron-beam Deposition," PhD, University of Maryland, College Park, MD, 2008.

[37] D. Dijkkamp, T. Venkatesan, X. D. Wu, S. A. Shaheen, N. Jisrawi, Y. H. Min-Lee, W. L. McLean, and M. Croft, "Preparation of Y‑Ba‑Cu oxide superconductor thin films using pulsed laser evaporation from high Tc bulk material," *Appl. Phys. Lett.*, vol. 51, no. 8, pp. 619–621, Aug. 1987.

[38] R. Ramesh, K. Luther, B. Wilkens, D. L. Hart, E. Wang, J. M. Tarascon, A. Inam, X. D. Wu, and T. Venkatesan, "Epitaxial growth of ferroelectric bismuth titanate thin films by pulsed laser deposition," *Appl. Phys. Lett.*, vol. 57, no. 15, pp. 1505–1507, Oct. 1990.

[39] S. Jin, M. McCormack, T. H. Tiefel, and R. Ramesh, "Colossal magnetoresistance in La‑Ca‑Mn‑O ferromagnetic thin films (invited)," *J. Appl. Phys.*, vol. 76, no. 10, pp. 6929–6933, Nov. 1994.

[40] R. Eason, *Pulsed Laser Deposition of Thin Films: Applications-Led Growth of Functional Materials*. John Wiley & Sons, 2007.

[41] D. Kan, C. J. Long, C. Steinmetz, S. E. Lofland, and I. Takeuchi, "Combinatorial search of structural transitions: Systematic investigation of morphotropic phase boundaries in chemically substituted BiFeO3," *J. Mater. Res.*, vol. 27, no. 21, pp. 2691–2704, 2012.

[42] R. Zarnetta, P. J. S. Buenconsejo, A. Savan, S. Thienhaus, and A. Ludwig, "High-throughput study of martensitic transformations in the complete Ti–Ni–Cu system," *Intermetallics*, vol. 26, pp. 98–109, Jul. 2012.

[43] M. L. Green, I. Takeuchi, and J. R. Hattrick-Simpers, "Applications of high throughput (combinatorial) methodologies to electronic, magnetic, optical, and energy-related materials," *J. Appl. Phys.*, vol. 113, no. 23, p. 231101, Jun. 2013.

[44] Susan Swapp, "Electron Probe Microanalysis," *Materials Characterization Laboratory*. [Online]. Available: http://mcl.gg.uwyo.edu/MicroProbe.htm.

[45] J. Als-Nielsen and D. McMorrow, *Elements of Modern X-ray Physics*. John Wiley & Sons, 2011.

[46] T. Funk, A. Deb, S. J. George, H. Wang, and S. P. Cramer, "X-ray magnetic circular dichroism—a high energy probe of magnetic properties," *Coord. Chem. Rev.*, vol. 249, no. 1–2, pp. 3–30, Jan. 2005.

[47] F. Tsui and P. A. Ryan, "Combinatorial molecular beam epitaxy synthesis and characterization of magnetic alloys," *Appl. Surf. Sci.*, vol. 189, no. 3–4, pp. 333–338, Apr. 2002.

[48] S. E. Russek, W. E. Bailey, G. Alers, and D. L. Abraham, "Magnetic combinatorial thin-film libraries," *IEEE Trans. Magn.*, vol. 37, no. 4, pp. 2156–2158, Jul. 2001.

[49] X. F. Li, J. Bao, J. Zhang, G. Chen, and C. Gao, "An imaging system for high-throughput magneto-optical Kerr effect characterization of combinatorial materials libraries," *Meas. Sci. Technol.*, vol. 18, no. 7, p. 2039, Jul. 2007.

[50] C. J. Long, D. Bunker, X. Li, V. L. Karen, and I. Takeuchi, "Rapid identification of structural phases in combinatorial thin-film libraries using x-ray diffraction and non-negative matrix factorization," *Rev. Sci. Instrum.*, vol. 80, no. 10, p. 103902, Oct. 2009.

[51] G. Barr, G. Cunningham, W. Dong, C. J. Gilmore, and T. Kojima, "High-throughput powder diffraction V: the use of Raman spectroscopy with and without X-ray powder diffraction data," *J. Appl. Crystallogr.*, vol. 42, no. 4, pp. 706–714, Aug. 2009.

[52] J. Scheidtmann, A. Frantzen, G. Frenzer, and W. F. Maier, "A combinatorial technique for the search of solid state gas sensor materials," *Meas. Sci. Technol.*, vol. 16, no. 1, p. 119, Jan. 2005.

[53] C. Long, "Near-field microwave microscopy and multivariate analysis of XRD data," 2011.

[54] D. D. Lee and H. S. Seung, "Learning the parts of objects by non-negative matrix factorization," *Nature*, vol. 401, no. 6755, pp. 788–791, Oct. 1999.

[55] F. Shahnaz, M. W. Berry, V. P. Pauca, and R. J. Plemmons, "Document clustering using nonnegative matrix factorization," *Inf. Process. Manag.*, vol. 42, no. 2, pp. 373–386, Mar. 2006.

[56] J. Piper, V. P. Pauca, R. J. Plemmons, and M. Giffin, "Object characterization from spectral data using nonnegative factorization and information theory," in *In Proc. Amos Technical Conf., Maui, HI*, 2004.

[57] A. Belsky, M. Hellenbrandt, V. L. Karen, and P. Luksch, "New developments in the Inorganic Crystal Structure Database (ICSD): accessibility in support of

materials research and design," *Acta Crystallogr. Sect. B,* vol. 58, no. 3–1, pp. 364–369, Jun. 2002.

[58] M. Yu, J. Hattrick-Simpers, I. Takeuchi, J. Li, Z. L. Wang, J. P. Liu, S. E. Lofland, S. Tyagi, J. W. Freeland, D. Giubertoni, M. Bersani, and M. Anderle, "Interphase exchange coupling in Fe∕Sm–Co bilayers with gradient Fe thickness," *J. Appl. Phys.,* vol. 98, no. 6, p. 063908, 2005.

[59] T. R. Gao, Y. Q. Wu, S. Fackler, I. Kierzewski, Y. Zhang, A. Mehta, M. J. Kramer, and I. Takeuchi, "Combinatorial exploration of rare-earth-free permanent magnets: Magnetic and microstructural properties of Fe-Co-W thin films," *Appl. Phys. Lett.,* vol. 102, no. 2, p. 022419, Jan. 2013.

[60] E. C. Stoner and E. P. Wohlfarth, "A Mechanism of Magnetic Hysteresis in Heterogeneous Alloys," *Philos. Trans. R. Soc. Lond. Ser. Math. Phys. Sci.,* vol. 240, no. 826, pp. 599–642, May 1948.

[61] E. Kondorsky, *J Phys Mosc.,* vol. II, p. 161, 1940.

[62] J. F. Herbst, R. W. Lee, and F. E. Pinkerton, "Rare Earth-Iron-Boron Materials: A New Era in Permanent Magnets," *Annu. Rev. Mater. Sci.,* vol. 16, no. 1, pp. 467–485, 1986.

[63] H. Yamamoto, Y. Matsuura, S. Fujimura, and M. Sagawa, "Magnetocrystalline anisotropy of R2Fe14B tetragonal compounds," *Appl. Phys. Lett.,* vol. 45, no. 10, pp. 1141–1143, Nov. 1984.

[64] D. R. Gauder, M. H. Froning, R. J. White, and A. E. Ray, "Elevated temperature study of Nd‑Fe‑B–based magnets with cobalt and dysprosium additions," *J. Appl. Phys.,* vol. 63, no. 8, pp. 3522–3524, Apr. 1988.

[65] X. Guo, X. Chen, Z. Altounian, and J. O. Ström-Olsen, "Temperature dependence of coercivity in MnBi," *J. Appl. Phys.,* vol. 73, pp. 6275–6277, May 1993.

[66] B. D. Cullity and C. D. Graham, *Introduction to Magnetic Materials,* 2 edition. Hoboken, N.J: Wiley-IEEE Press, 2008.

[67] J. Stöhr, "Exploring the microscopic origin of magnetic anisotropies with X-ray magnetic circular dichroism (XMCD) spectroscopy," *J. Magn. Magn. Mater.,* vol. 200, no. 1–3, pp. 470–497, Oct. 1999.

[68] Y. Otani, H. Miyajima, and S. Chikazumi, "Magnetocrystalline anisotropy in Nd‑Fe‑B magnet," *J. Appl. Phys.,* vol. 61, no. 8, pp. 3436–3438, Apr. 1987.

[69] P. Mohn and E. P. Wohlfarth, "The Curie temperature of the ferromagnetic transition metals and their compounds," *J. Phys. F Met. Phys.,* vol. 17, no. 12, p. 2421, Dec. 1987.

[70] D. J. Sellmyer, M. A. Engelhardt, S. S. Jaswal, and A. J. Arko, "Electronic Structure and Magnetism of ${\mathrm{Nd}}_{2}$${\mathrm{Fe}}_{14}$B and Related Compounds," *Phys. Rev. Lett.,* vol. 60, no. 20, pp. 2077–2080, May 1988.

[71] L. Zhou, M. K. Miller, H. Dillon, A. Palasyuk, S. Constantinides, R. W. McCallum, I. E. Anderson, and M. J. Kramer, "Role of the Applied Magnetic Field on the Microstructural Evolution in Alnico 8 Alloys," *Metall. Mater. Trans. E,* vol. 1, no. 1, pp. 27–35, Mar. 2014.

[72] D. V. Ratnam and W. R. Buessem, "Angular Variation of Coercive Force in Barium Ferrite," *J. Appl. Phys.,* vol. 43, no. 3, pp. 1291–1293, Mar. 1972.

[73] F. Schumacher, "On the modification of the Kondorsky function," *J. Appl. Phys.*, vol. 70, no. 6, pp. 3184–3187, Sep. 1991.

[74] S. Chikazumi, *Physics of Ferromagnetism 2e*. Oxford University Press, 2009.

[75] F. Y. Yang, C. L. Chien, E. F. Ferrari, X. W. Li, G. Xiao, and A. Gupta, "Uniaxial anisotropy and switching behavior in epitaxial CrO2 films," *Appl. Phys. Lett.*, vol. 77, no. 2, pp. 286–288, Jul. 2000.

[76] K. R. Coffey, T. Thomson, and J.-U. Thiele, "Angular dependence of the switching field of thin-film longitudinal and perpendicular magnetic recording media," *J. Appl. Phys.*, vol. 92, no. 8, pp. 4553–4559, Oct. 2002.

[77] A. Singh, V. Neu, S. Fähler, K. Nenkov, L. Schultz, and B. Holzapfel, "Relevance of pinning, nucleation, and interaction in nanograined epitaxial hard magnetic ${\text{SmCo}}_{5}$ films," *Phys. Rev. B*, vol. 79, no. 21, p. 214401, Jun. 2009.

[78] S. M. Dubiel and W. Zinn, "Changes in the electronic structure of iron induced by substitutional impurity W atoms," *Phys. Rev. B*, vol. 30, no. 7, pp. 3783–3789, Oct. 1984.

[79] A. Kashyap, P. Manchanda, P. K. Sahota, R. Skomski, J. E. Shield, and D. J. Sellmyer, "Anisotropy of W in Fe and Co," *IEEE Trans. Magn.*, vol. 47, no. 10, pp. 3336–3339, Oct. 2011.

[80] N. Kikuchi, O. Kitakami, S. Okamoto, Y. Shimada, A. Sakuma, Y. Otani, and K. Fukamichi, "Influence of 5d transition elements on the magnetocrystalline anisotropy of hcp-Co," *J. Phys. Condens. Matter*, vol. 11, no. 43, p. L485, Nov. 1999.

[81] S. M. Dubiel and W. Zinn, "Influence of V on the Fe site spin and charge densities in BCC-Iron," *J. Magn. Magn. Mater.*, vol. 37, no. 3, pp. 237–245, Jul. 1983.

[82] P. Léonard and N. Stéfanou, "Electronic structure of 3d impurities in ferromagnetic iron," *J. Phys.*, vol. 43, no. 10, pp. 1497–1502, 1982.

[83] H. C. Fiedler and A. M. Davis, "The formation of gamma phase in Vanadium Permendur," *Metall. Trans.*, vol. 1, no. 4, pp. 1036–1037, Apr. 1970.

[84] A. A. Couto and P. I. Ferreira, "Phase transformations and properties of Fe-Co alloys," *J. Mater. Eng.*, vol. 11, no. 1, pp. 31–36, Mar. 1989.

[85] E. A. Nesbitt, "Vicalloy—A Workable Alloy for Permanent Magnets," *Transactions*, pp. 415–425, 1946.

[86] "Materials for Permanent Magnets," in *Ferromagnetism*, IEEE, 2009, pp. 344–422.

[87] J. E. Bennett and M. R. Pinnel, "Equilibrium phases and transformations in Fe/Co/2--3%V alloys," 1974.

[88] K. Kawahara, "Structures and mechanical properties of an FeCo-2V alloy," *J. Mater. Sci.*, vol. 18, no. 11, pp. 3427–3436, Nov. 1983.

[89] J. A. Ashby, H. M. Flower, and R. D. Rawlings, "Gamma phase in an Fe-Co-2%V alloy," *Met. Sci.*, vol. 11, no. 3, pp. 91–96, Mar. 1977.

[90] M. Oron, S. Shtrikman, and D. Treves, "Study of Co-Fe-V Permanent Magnet alloys (vicalloys)," *J. Mater. Sci.*, vol. 4, no. 7, pp. 581–591, Jul. 1969.

[91] W. Baran, W. Breuer, H. Fahlenbrach, and K. Janssen, "Some Investigations on Iron-Cobalt Permanent Magnet Alloys of the Vicalloy II Type," *J. Appl. Phys.*, vol. 32, no. 3, pp. S199–S200, Mar. 1961.

[92] E. Josso, "Iron-cobalt-vanadium alloys: A critical study of the phase diagrams in relation to magnetic properties," *IEEE Trans. Magn.*, vol. 10, no. 2, pp. 161–165, Jun. 1974.

[93] I. Joffe, "Magnetic hardening and anomalous behaviour of Vicalloy," *J. Mater. Sci.*, vol. 9, no. 2, pp. 315–322, Feb. 1974.

[94] J. E. Bennett and M. R. Pinnel, "Aspects of phase equilibria in Fe/Co/2.5 to 3.0% V alloys," *J. Mater. Sci.*, vol. 9, no. 7, pp. 1083–1090, Jul. 1974.

[95] A. Watson and L. Cornish, "Cobalt – Iron – Vanadium," in *Ternary Alloy Systems*, G. Effenberg and S. Ilyenko, Eds. Springer Berlin Heidelberg, 2008, pp. 35–67.

[96] B. Heinrich and J. a. C. Bland, "Introduction," in *Ultrathin Magnetic Structures I*, J. A. C. Bland and B. Heinrich, Eds. Springer Berlin Heidelberg, 1994, pp. 1–19.

[97] *Phase Transformations in Metals and Alloys, Third Edition (Revised Reprint). .*

[98] Olugbenga O. Famodu, "COMBINATORIAL INVESTIGATION OF FERROMAGNETIC SHAPE MEMORY ALLOYS," PhD, University of Maryland, College Park, MD, 2005.

[99] I. Takeuchi, O. O. Famodu, J. C. Read, M. A. Aronova, K.-S. Chang, C. Craciunescu, S. E. Lofland, M. Wuttig, F. C. Wellstood, L. Knauss, and A. Orozco, "Identification of novel compositions of ferromagnetic shape-memory alloys using composition spreads," *Nat. Mater.*, vol. 2, no. 3, pp. 180–184, Mar. 2003.

[100] T. Harano, G. Shibata, K. Yoshimatsu, K. Ishigami, V. K. Verma, Y. Takahashi, T. Kadono, T. Yoshida, A. Fujimori, T. Koide, F.-H. Chang, H.-J. Lin, D.-J. Huang, C.-T. Chen, P.-H. Xiang, H. Yamada, and A. Sawa, "Phase diagram of Ca1−xCexMnO3 thin films studied by X-ray magnetic circular dichroism," *Solid State Commun.*, vol. 207, pp. 50–53, Apr. 2015.

[101] G. Shamsutdinov, "Application Of Scanning Hall Probe Microscopy For High Throughput Characterization Of Combinatorial Magnetic Materials," *Wayne State Univ. Diss.*, Jan. 2013.

[102] D. Goll, R. Loeffler, J. Herbst, R. Karimi, and G. Schneider, "High-throughput search for new permanent magnet materials," *J. Phys. Condens. Matter*, vol. 26, no. 6, p. 064208, Feb. 2014.

[103] G. Suran and P. Bernstein, "Aging phenomena at room temperature in amorphous GdFe thin films," *J. Magn. Magn. Mater.*, vol. 54–57, Part 1, pp. 229–230, Feb. 1986.

[104] Q. Zhu, L. Li, M. S. Masteller, and G. J. D. Corso, "An increase of structural order parameter in Fe–Co–V soft magnetic alloy after thermal aging," *Appl. Phys. Lett.*, vol. 69, no. 25, pp. 3917–3919, Dec. 1996.

[105] H. STUWE, "DESCRIPTION OF THE SIGMA PHASE AS A STRUCTURE WITH SPHERE PACKING," *Trans. Am. Inst. Min. Metall. Eng.*, vol. 215, no. 3, pp. 408–411, 1959.

[106] V. N. A. Singh, "Mechanism of coercivity in epitaxial SmCo5 thin films," *Phys. Rev. B - PHYS REV B*, vol. 77, no. 10, 2008.

[107] P. Haasen, "Magnetic Precipitation-Hardening," *Met. Sci.*, vol. 9, no. 1, pp. 41–44, Jan. 1975.

[108] J. P. Woods, A. Ushioda, A. Fukuno, S. Sun, L. Henderson, and R. C. OHandley, "Surface magnetization of Co70V10B20 and Fe77Cr6B17 amorphous alloys," *J. Appl. Phys.*, vol. 64, no. 10, pp. 5446–5448, Nov. 1988.

[109] J. J. Burton, "Surface segregation in alloys: Dilute solid solutions of vanadium in palladium," *Surf. Sci.*, vol. 69, no. 2, pp. 712–713, Dec. 1977.

[110] R. Hayakawa, Y. Hatano, K. Fujii, K. Fukumoto, H. Matsui, and K. Watanabe, "Surface segregation and oxidation of Ti in a V−Ti alloy," *J. Nucl. Mater.*, vol. 307–311, Part 1, pp. 580–584, Dec. 2002.

[111] J. Bernasconi, S. Strässler, and R. S. Perkins, "Simple models for the coercivity of hard magnetic materials," in *AIP Conference Proceedings*, 1975, vol. 24, pp. 761–762.

[112] D. I. Paul, "General theory of the coercive force due to domain wall pinning," *J. Appl. Phys.*, vol. 53, no. 3, pp. 1649–1654, Mar. 1982.

[113] M. E. McHenry and D. E. Laughlin, "Nano-scale materials development for future magnetic applications," *Acta Mater.*, vol. 48, no. 1, pp. 223–238, Jan. 2000.

[114] H. Kronmüller, K.-D. Durst, and M. Sagawa, "Analysis of the magnetic hardening mechanism in RE-FeB permanent magnets," *J. Magn. Magn. Mater.*, vol. 74, no. 3, pp. 291–302, Oct. 1988.

[115] R. H. Yu, S. Basu, Y. Zhang, A. Parvizi-Majidi, and J. Q. Xiao, "Pinning effect of the grain boundaries on magnetic domain wall in FeCo-based magnetic alloys," *J. Appl. Phys.*, vol. 85, no. 9, pp. 6655–6659, May 1999.

[116] R. H. Yu and J. Zhu, "Precipitation and high temperature magnetic properties of FeCo-based alloys," *J. Appl. Phys.*, vol. 97, no. 5, p. 053905, Mar. 2005.

[117] R. D. K. Misra, "Grain boundary segregation of phosphorus in iron-vanadium alloys," *Acta Mater.*, vol. 44, no. 11, pp. 4367–4373, Nov. 1996.

[118] Pierre M. P. Curie, "Sur la symétrie dans les phénomènes physiques, symétrie d'un champ électrique et d'un champ magnétique," *J Phys.*, vol. 3, pp. 393–415, 1984.

[119] E. Ascher, H. Rieder, H. Schmid, and H. Stössel, "Some Properties of Ferromagnetoelectric Nickel‐Iodine Boracite, Ni3B7O13I," *J. Appl. Phys.*, vol. 37, no. 3, pp. 1404–1405, Mar. 1966.

[120] N. A. Spaldin and M. Fiebig, "The Renaissance of Magnetoelectric Multiferroics," *Science*, vol. 309, no. 5733, pp. 391–392, Jul. 2005.

[121] G. Catalan and J. F. Scott, "Physics and Applications of Bismuth Ferrite," *Adv. Mater.*, vol. 21, no. 24, pp. 2463–2485, Jun. 2009.

[122] J. Silva, A. Reyes, H. Esparza, H. Camacho, and L. Fuentes, "BiFeO3: A Review on Synthesis, Doping and Crystal Structure," *Integr. Ferroelectr.*, vol. 126, no. 1, pp. 47–59, Jan. 2011.

[123] J. Wang, J. B. Neaton, H. Zheng, V. Nagarajan, S. B. Ogale, B. Liu, D. Viehland, V. Vaithyanathan, D. G. Schlom, U. V. Waghmare, N. A. Spaldin, K. M. Rabe, M. Wuttig, and R. Ramesh, "Epitaxial BiFeO3 Multiferroic Thin

Film Heterostructures," *Science*, vol. 299, no. 5613, pp. 1719–1722, Mar. 2003.

[124] S.-W. Cheong and M. Mostovoy, "Multiferroics: a magnetic twist for ferroelectricity," *Nat. Mater.*, vol. 6, no. 1, pp. 13–20, Jan. 2007.

[125] S. Fujino, M. Murakami, V. Anbusathaiah, S.-H. Lim, V. Nagarajan, C. J. Fennie, M. Wuttig, L. Salamanca-Riba, and I. Takeuchi, "Combinatorial discovery of a lead-free morphotropic phase boundary in a thin-film piezoelectric perovskite," *Appl. Phys. Lett.*, vol. 92, no. 20, p. 202904, May 2008.

[126] M. Fiebig, "Revival of the magnetoelectric effect," *J. Phys. Appl. Phys.*, vol. 38, no. 8, p. R123, Apr. 2005.

[127] C.-W. Nan, M. I. Bichurin, S. Dong, D. Viehland, and G. Srinivasan, "Multiferroic magnetoelectric composites: Historical perspective, status, and future directions," *J. Appl. Phys.*, vol. 103, no. 3, p. 031101, Feb. 2008.

[128] 段**纯刚** C.-G. D., "Interface/surface magnetoelectric effects: New routes to the electric field control of magnetism," *Front. Phys.*, vol. 7, no. 4, pp. 375–379, Aug. 2012.

[129] L. Shu, Z. Li, J. Ma, Y. Gao, L. Gu, Y. Shen, Y. Lin, and C. W. Nan, "Thickness-dependent voltage-modulated magnetism in multiferroic heterostructures," *Appl. Phys. Lett.*, vol. 100, no. 2, p. 022405, Jan. 2012.

[130] J.-M. Hu, Z. Li, J. Wang, and C. W. Nan, "Electric-field control of strain-mediated magnetoelectric random access memory," *J. Appl. Phys.*, vol. 107, no. 9, p. 093912, May 2010.

[131] C. Israel, N. D. Mathur, and J. F. Scott, "A one-cent room-temperature magnetoelectric sensor," *Nat. Mater.*, vol. 7, no. 2, pp. 93–94, Feb. 2008.

[132] J. Ma, J. Hu, Z. Li, and C.-W. Nan, "Recent Progress in Multiferroic Magnetoelectric Composites: from Bulk to Thin Films," *Adv. Mater.*, vol. 23, no. 9, pp. 1062–1087, Mar. 2011.

[133] Y. Zhang, J. Liu, X. H. Xiao, T. C. Peng, C. Z. Jiang, Y. H. Lin, and C. W. Nan, "Large reversible electric-voltage manipulation of magnetism in NiFe/BaTiO3 heterostructures at room temperature," *J. Phys. Appl. Phys.*, vol. 43, no. 8, p. 082002, Mar. 2010.

[134] T. Nan, Z. Zhou, M. Liu, X. Yang, Y. Gao, B. A. Assaf, H. Lin, S. Velu, X. Wang, H. Luo, J. Chen, S. Akhtar, E. Hu, R. Rajiv, K. Krishnan, S. Sreedhar, D. Heiman, B. M. Howe, G. J. Brown, and N. X. Sun, "Quantification of strain and charge co-mediated magnetoelectric coupling on ultra-thin Permalloy/PMN-PT interface," *Sci. Rep.*, vol. 4, Jan. 2014.

[135] S. Geprägs, A. Brandlmaier, M. Opel, R. Gross, and S. T. B. Goennenwein, "Electric field controlled manipulation of the magnetization in Ni/BaTiO3 hybrid structures," *Appl. Phys. Lett.*, vol. 96, no. 14, p. 142509, Apr. 2010.

[136] A. Brandlmaier, S. Geprägs, G. Woltersdorf, R. Gross, and S. T. B. Goennenwein, "Nonvolatile, reversible electric-field controlled switching of remanent magnetization in multifunctional ferromagnetic/ferroelectric hybrids," *J. Appl. Phys.*, vol. 110, no. 4, p. 043913, Aug. 2011.

[137] S. Sahoo, S. Polisetty, C.-G. Duan, S. S. Jaswal, E. Y. Tsymbal, and C. Binek, "Ferroelectric control of magnetism in BaTiO3/Fe heterostructures via interface strain coupling," *Phys. Rev. B*, vol. 76, p. 092108, Sep. 2007.

[138] T. H. E. Lahtinen and S. van Dijken, "Temperature control of local magnetic anisotropy in multiferroic CoFe/BaTiO3," *Appl. Phys. Lett.*, vol. 102, no. 11, p. 112406, Mar. 2013.

[139] T. H. E. Lahtinen, J. O. Tuomi, and S. van Dijken, "Electrical Writing of Magnetic Domain Patterns in Ferromagnetic/Ferroelectric Heterostructures," *IEEE Trans. Magn.*, vol. 47, no. 10, pp. 3768–3771, 2011.

[140] T. H. E. Lahtinen, K. J. A. Franke, and S. van Dijken, "Electric-field control of magnetic domain wall motion and local magnetization reversal," *Sci. Rep.*, vol. 2, Feb. 2012.

[141] T.-K. Chung, G. P. Carman, and K. P. Mohanchandra, "Reversible magnetic domain-wall motion under an electric field in a magnetoelectric thin film," *Appl. Phys. Lett.*, vol. 92, no. 11, p. 112509, Mar. 2008.

[142] Y.-H. Chu, L. W. Martin, M. B. Holcomb, M. Gajek, S.-J. Han, Q. He, N. Balke, C.-H. Yang, D. Lee, W. Hu, Q. Zhan, P.-L. Yang, A. Fraile-Rodríguez, A. Scholl, S. X. Wang, and R. Ramesh, "Electric-field control of local ferromagnetism using a magnetoelectric multiferroic," *Nat. Mater.*, vol. 7, no. 6, pp. 478–482, Jun. 2008.

[143] J. T. Heron, M. Trassin, K. Ashraf, M. Gajek, Q. He, S. Y. Yang, D. E. Nikonov, Y.-H. Chu, S. Salahuddin, and R. Ramesh, "Electric-Field-Induced Magnetization Reversal in a Ferromagnet-Multiferroic Heterostructure," *Phys. Rev. Lett.*, vol. 107, no. 21, p. 217202, Nov. 2011.

[144] T. Brintlinger, S.-H. Lim, K. H. Baloch, P. Alexander, Y. Qi, J. Barry, J. Melngailis, L. Salamanca-Riba, I. Takeuchi, and J. Cumings, "In Situ Observation of Reversible Nanomagnetic Switching Induced by Electric Fields," *Nano Lett.*, vol. 10, no. 4, pp. 1219–1223, Apr. 2010.

[145] C.-J. Hsu, J. L. Hockel, and G. P. Carman, "Magnetoelectric manipulation of domain wall configuration in thin film Ni/[Pb(Mn1/3Nb2/3)O3]0.68-[PbTiO3]0.32 (001) heterostructure," *Appl. Phys. Lett.*, vol. 100, no. 9, p. 092902, Feb. 2012.

[146] J. Unguris, S. R. Bowden, D. T. Pierce, M. Trassin, R. Ramesh, S.-W. Cheong, S. Fackler, and I. Takeuchi, "Simultaneous imaging of the ferromagnetic and ferroelectric structure in multiferroic heterostructures," *APL Mater.*, vol. 2, no. 7, p. 076109, Jul. 2014.

[147] J. van Suchtelen, *Philips Res Rep*, vol. 27, p. 28, 1972.

[148] S. Geprägs, M. Opel, S. T. B. Goennenwein, and R. Gross, "Giant magnetoelastic effects in BaTiO3-based extrinsic multiferroic hybrids," *Phys. Rev. B*, vol. 86, no. 13, p. 134432, Oct. 2012.

[149] S. Geprägs, D. Mannix, M. Opel, S. T. B. Goennenwein, and R. Gross, "Converse magnetoelectric effects in Fe${}_{3}$O${}_{4}$/BaTiO${}_{3}$ multiferroic hybrids," *Phys. Rev. B*, vol. 88, no. 5, p. 054412, Aug. 2013.

[150] T. N. Yang, J.-M. Hu, C. W. Nan, and L. Q. Chen, "On the elastically coupled magnetic and ferroelectric domains: A phase-field model," *Appl. Phys. Lett.*, vol. 104, no. 20, p. 202402, May 2014.

[151] C. B. Hill, W. R. Hendren, R. M. Bowman, P. K. McGeehin, M. A. Gubbins, and V. A. Venugopal, "Whole wafer magnetostriction metrology for magnetic films and multilayers," *Meas. Sci. Technol.*, vol. 24, no. 4, p. 045601, Apr. 2013.

[152] F. Felten, G. A. Schneider, J. M. Saldaña, and S. V. Kalinin, "Modeling and measurement of surface displacements in BaTiO3 bulk material in piezoresponse force microscopy," *J. Appl. Phys.*, vol. 96, no. 1, pp. 563–568, Jul. 2004.

[153] W. Karboul-Trojet, D. Faurie, E. Aït-Yahiatène, Y. Roussigné, F. Mazaleyrat, and S. M. Chérif, "In situ tailoring of magnetization configuration in NiFe film deposited onto flexible substrate," *J. Appl. Phys.*, vol. 111, no. 7, p. 07A926, Mar. 2012.

[154] J. Ben Youssef, N. Vukadinovic, D. Billet, and M. Labrune, "Thickness-dependent magnetic excitations in Permalloy films with nonuniform magnetization," *Phys. Rev. B*, vol. 69, no. 17, p. 174402, May 2004.

[155] Y. Murayama, "Micromagnetics on Stripe Domain Films. I. Critical Cases," *J. Phys. Soc. Jpn.*, vol. 21, p. 2253, Nov. 1966.

[156] B. B. Pant and K. Matsuyama, "Numerical Investigation of Stripe Structures in Ferromagnetic Thin Films with Perpenedicular Anisotropy," *Jpn. J. Appl. Phys.*, vol. 32, no. Part 1, No. 9A, pp. 3817–3822, 1993.

[157] N. Saito, H. Fujiwara, and Y. Sugita, "A New Type of Magnetic Domain Structure in Negative Magnetostriction Ni-Fe Films," *J. Phys. Soc. Jpn.*, vol. 19, no. 7, pp. 1116–1125, 1964.

[158] R. J. Spain, "STRIPE DOMAINS IN NICKEL/IRON FILMS," *Appl. Phys. Lett.*, vol. 6, no. 1, pp. 8–9, Jan. 1965.

[159] N. Amos, R. Fernandez, R. Ikkawi, B. Lee, A. Lavrenov, A. Krichevsky, D. Litvinov, and S. Khizroev, "Magnetic force microscopy study of magnetic stripe domains in sputter deposited Permalloy thin films," *J. Appl. Phys.*, vol. 103, no. 7, pp. 07E732–07E732–3, Apr. 2008.

[160] A. V. Svalov, I. R. Aseguinolaza, A. Garcia-Arribas, I. Orue, J. M. Barandiaran, J. Alonso, M. L. FernAndez-Gubieda, and G. V. Kurlyandskaya, "Structure and Magnetic Properties of Thin Permalloy Films Near the #x201C;Transcritical #x201D; State," *IEEE Trans. Magn.*, vol. 46, no. 2, pp. 333–336, 2010.

[161] A. Hubert and R. Schäfer, *Magnetic Domains: The Analysis of Magnetic Microstructures*, Corrected edition. Springer, 2008.

[162] L. M. Alvarez-Prado, G. T. Pérez, R. Morales, F. H. Salas, and J. M. Alameda, "Perpendicular anisotropy detected by transversely biased initial susceptibility via the magneto-optic Kerr effect in Fe_{x}Si_{1-x} thin films and Fe_{x}Si_{1-x}/Si multilayers: Theory and experiment," *Phys. Rev. B*, vol. 56, no. 6, pp. 3306–3316, Aug. 1997.

[163] D. Clarke, O. A. Tretiakov, and O. Tchernyshyov, "Stripes in thin ferromagnetic films with out-of-plane anisotropy," *Phys. Rev. B*, vol. 75, no. 17, p. 174433, May 2007.

[164] J.-H. Park, J.-H. Park, K.-B. Lee, T.-Y. Koo, H. S. Youn, Y.-D. Ko, J.-S. Chung, J. Y. Hwang, and S.-Y. Jeong, "Local strain-induced 90 degree domain

switching in a barium titanate single crystal," *Appl. Phys. Lett.*, vol. 91, no. 1, pp. 012906–012906–3, Jul. 2007.

[165] M. Takashige, S.-I. Hamazaki, N. Fukurai, and F. Shimizu, "Surface Morphology of Tetragonal PbTiO $_3$ and BaTiO $_3$ Observed by Atomic Force Microscopy," *J. Phys. Soc. Jpn.*, vol. 66, no. 6, pp. 1848–1849, Jun. 1997.

[166] N. T. Tsou, P. R. Potnis, and J. E. Huber, "Classification of laminate domain patterns in ferroelectrics," *Phys. Rev. B*, vol. 83, no. 18, p. 184120, May 2011.

[167] S. V. Kalinin, B. J. Rodriguez, S. Jesse, J. Shin, A. P. Baddorf, P. Gupta, H. Jain, D. B. Williams, and A. Gruverman, "Vector Piezoresponse Force Microscopy," *Microsc. Microanal.*, vol. 12, no. 03, pp. 206–220, 2006.

[168] J.-H. Park, J.-H. Park, K.-B. Lee, T.-Y. Koo, H. S. Youn, Y.-D. Ko, J.-S. Chung, J. Y. Hwang, and S.-Y. Jeong, "Local strain-induced 90 degree domain switching in a barium titanate single crystal," *Appl. Phys. Lett.*, vol. 91, no. 1, pp. 012906–012906–3, Jul. 2007.

[169] J. P. Remeika and W. M. Jackson, "A Method for Growing Barium Titanate Single Crystals," *J. Am. Chem. Soc.*, vol. 76, no. 3, pp. 940–941, Feb. 1954.

[170] R. Clarke, "Phase transition studies of pure and flux-grown barium titanate crystals," *J. Appl. Crystallogr.*, vol. 9, no. 4, pp. 335–338, Aug. 1976.

[171] Donahue, M.J. and Porter, D.G., "OOMMF User's Guide, Version 1.0," National Institute of Standards and Technology, Gaithersburg, MD, Interagency Report 6376, Sep. 1999.

[172] M. Takahashi, D. Watanabe, T. Kōno, and S. Ogawa, "Induced Magnetic Anisotropy of Evaporated Ni–Fe Films," *J. Phys. Soc. Jpn.*, vol. 15, no. 7, pp. 1351–1352, 1960.

[173] R. D. McMichael and M. J. Donahue, "Head to head domain wall structures in thin magnetic strips," *IEEE Trans. Magn.*, vol. 33, no. 5, pp. 4167–4169, Sep. 1997.

[174] M. M. Yang and J. A. Aboaf, "rf-diode sputtered Permalloy film," *J. Appl. Phys.*, vol. 66, no. 8, pp. 3734–3740, Oct. 1989.

[175] H. Deng, M. K. Minor, and J. A. Barnard, "Comparison of mechanical and tribological properties of permalloy and high moment FeTaN thin films for tape recording heads," *IEEE Trans. Magn.*, vol. 32, no. 5, pp. 3702–3704, Sep. 1996.

[176] D. Nečas and P. Klapetek, "Gwyddion: an open-source software for SPM data analysis," *Cent. Eur. J. Phys.*, vol. 10, no. 1, pp. 181–188, Feb. 2012.

[177] V. Anbusathaiah, D. Kan, F. C. Kartawidjaja, R. Mahjoub, M. A. Arredondo, S. Wicks, I. Takeuchi, J. Wang, and V. Nagarajan, "Labile Ferroelastic Nanodomains in Bilayered Ferroelectric Thin Films," *Adv. Mater.*, vol. 21, no. 34, pp. 3497–3502, Sep. 2009.

[178] S. Fusil, V. Garcia, A. Barthélémy, and M. Bibes, "Magnetoelectric Devices for Spintronics," *Annu. Rev. Mater. Res.*, vol. 44, no. 1, pp. 91–116, 2014.

[179] J. J. Wang, J. M. Hu, J. Ma, J. X. Zhang, L. Q. Chen, and C. W. Nan, "Full 180° Magnetization Reversal with Electric Fields," *Sci. Rep.*, vol. 4, Dec. 2014.

[180] M. Rivera, C. H. Rios-Reyes, and L. H. Mendoza-Huizar, "Magnetic transition phase diagram of cobalt clusters electrodeposited on HOPG: Experimental and

micromagnetic modelling study," *J. Magn. Magn. Mater.*, vol. 323, no. 7, pp. 997–1000, Apr. 2011.